

1           **Imaging spectroscopy: Earth and planetary remote sensing with the**  
2           **PSI Tetracorder and expert systems: from Rovers to EMIT and Beyond**  
3

4           Roger N. Clark<sup>1</sup>, Gregg A. Swayze<sup>2</sup>, K. Eric Livo<sup>2</sup>, Phil Brodrick<sup>3</sup>, Eldar Noe Dobrea<sup>1</sup>,  
5           Srinivasan Vijayarangan<sup>4</sup>, Robert O. Green<sup>3</sup>, David Wettergreen<sup>4</sup>, Alberto Candela<sup>3</sup>,  
6           Amanda Hendrix<sup>1</sup>, Carlos Pérez García-Pando<sup>5,6</sup>, Neil Pearson<sup>1</sup>, Melissa D. Lane<sup>8</sup>,  
7           Adolfo González-Romero<sup>5,7,9</sup>, Xavier Querol<sup>7</sup>, and the EMIT and TREX teams.  
8  
9

10          <sup>1</sup> Planetary Science Institute, Tucson, Arizona, USA  
11

12          <sup>2</sup> U. S. Geological Survey, Denver, Colorado, USA  
13

14          <sup>3</sup> Jet Propulsion Laboratory, California Institute of Technology, Pasadena, California, USA  
15

16          <sup>4</sup> Carnegie Mellon University, Pittsburgh, Pennsylvania, USA  
17

18          <sup>5</sup> Barcelona Supercomputing Center (BSC), Barcelona, Spain  
19

20          <sup>6</sup> Catalan Institution for Research and Advanced Studies, Barcelona, Spain  
21

22          <sup>7</sup> Spanish Research Council, Institute of Environmental Assessment and water Research  
23           (IDAEA-CSIC), Barcelona, Spain  
24

25          <sup>8</sup> Fibernetics LLC, Lititz, Pennsylvania, USA  
26

27          <sup>9</sup> Polytechnical University of Catalonia (UPC), environmental engineering doctoral programme,  
28           Barcelona, Spain  
29

31          Submitted to Planetary Science Journal November 10, 2023  
32

33          Send correspondence to: rclark@psi.edu  
34

35   **Abstract**

36

37   A system for rapid analysis of spectroscopy data with emphasis on planetary surfaces, both imaging  
38   and single spectrum data is described. The system, called Tetracorder, is commanded by an expert  
39   system developed by expert spectroscopists. The Tetracorder and the expert system applies multiple  
40   algorithms to analyze a spectrum in segments, leveraging the advantages of each spectral region's  
41   sensitivity to detecting different compounds, whether solid, liquid or gas. The algorithms compare  
42   measured spectra to the spectral properties of materials in spectral libraries. The libraries include pure  
43   minerals, mineral mixtures that include areal mixtures, intimate mixtures, coatings, and molecular  
44   mixtures and other compounds such as organics, vegetation, liquids and gases. Absorption bands of a  
45   particulate surface change shape with grain size, and shape changes are used in some cases to constrain  
46   grain size of each component in the surface. The different algorithm results are compared for each  
47   spectral region and specific material composition and average grain size (when possible) are identified.  
48   The system is operational analyzing real-time data on a new generation of rover for future planetary  
49   missions as well as identifying materials from a spectrometer on the International Space Station. Four  
50   abundance models, with increasing sophistication are developed that are computationally fast on  
51   imaging spectrometer data are presented, and use Tetracorder identifications to produce maps of  
52   mineral abundances. A fifth full radiative model that includes multi-layer surfaces is presented but is  
53   computationally intensive. The system is open source and available on Github.

54

55

56

57

58

59

60

61 **Introduction**

62  
63 Spectroscopy is a tool that has been used for decades to identify, understand, and quantify solid, liquid  
64 or gaseous compounds. Spectroscopy is used in many professions and disciplines ranging from police  
65 work to mining and environmental assessment to astronomy for remotely detecting compounds. In the  
66 laboratory, spectroscopic measurements are used to detect absorption features caused by specific  
67 chemical bonds. Models can be applied to determine the abundance and physical state of the detected  
68 absorbing species. Imaging spectroscopy is a tool that can be used to spectrally identify and spatially  
69 map compounds having specific chemical bonds (Clark, 1999, 2003 and references therein), whether  
70 solid (crystalline or amorphous), liquid or gas.

71 In this work we describe the software system, called Tetracorder, that is effective at material  
72 identification and mapping. Tetracorder employs a set of algorithms within an expert system decision-  
73 making framework to identify and map compounds, whether solid, liquid or gas. The expertise in the  
74 system has been developed over the last ~ 35 years by a team of expert spectroscopists utilizing their  
75 scientific knowledge of spectral identification and material behavior. Tetracorder has approximately  
76 100 person-years in development, testing, and verification. In modern terms of Artificial Intelligence,  
77 AI, this might be called Expert Intelligence, or EI. This paper describes the system and innovations  
78 developed since publication of the original Tetracorder paper (Clark et al., 2003).

79 Tetracorder has two modes of data analysis: single spectrum and imaging spectrometer. Single  
80 spectrum mode has two modes: 1) command line one spectrum at a time, and 2) follow a growing file  
81 of incoming spectra for real time analysis as spectra are received. Tetracorder has been deployed on  
82 the Carnegie Mellon University Zoë rover (Wagner et al., 2005; Wettergreen et al., 2005; Wettergreen  
83 et al., 2008; Vijayarangan et al., 2018; Clark et al., 2022) analyzing spectra real time as the rover  
84 explores autonomously, while making decisions based on Tetracorder identifications. Tetracorder is  
85 also being used by the NASA Earth Surface Mineral Dust Source Investigation (EMIT) science team at  
86 the Jet Propulsion Laboratory (JPL) on a Beowulf cluster. The EMIT instrument, an imaging  
87 spectrometer, is located on the International Space Station and is delivering thousands of scenes per  
88 month of the Earth's surface. Each EMIT scene covers about 75 x 75 km with 60 m/pixels and 285  
89 bands from 0.38 to 2.5  $\mu\text{m}$  (Green, 2023). Each scene has the atmospheric absorptions and scattering  
90 removed (Thompson et al., 2018; Brodrick et al., 2023), and the solar radiance corrected to derive  
91 apparent surface reflectance. The EMIT reflectance image cubes are analyzed by Tetracorder to deliver  
92 maps of minerals for use in climate change models to predict the radiative forcing impact of mineral  
93 dusts. Tetracorder is also being used by the European Research Council FRontiers in dust  
94 minerAloGical coMposition and its Effects upoN climaTe (FRAGMENT) project, which includes field  
95 measurements and sampling that can be used to verify EMIT and Tetracorder results. In this paper, we  
96 describe Tetracorder 5.27 as deployed on the Zoë rover and for EMIT/JPL in 2022/2023.

97 An imaging spectrometer data set may include millions of spectra, and Tetracorder can find hundreds  
98 of materials in a scene, including minerals, amorphous materials, inclusions, mixtures, and on Earth,  
99 vegetation spectral type, water content, chlorophyll red-edge position, photosynthetic and non-  
100 photosynthetic vegetation. Ice and snow grain size and melting snow is also identified and mapped.

101 Water is identified and the contaminant levels in water are determined. All these possibilities result in  
102 thousands of image files to review, so post Tetracorder analysis summarizes what was found in text  
103 files and in derived materials maps as browse products. A standard image stretch is performed so that  
104 these products may be included in a mosaic with multiple scenes.

105

106

107 **Tetracorder**

108

109 Tetracorder is a system for applying multiple algorithms to a single spectrum or a group of spectra  
110 (e.g., an imaging spectrometer data set) to identify and map mineralogy, chemistry, and particle grain  
111 size. Tetracorder is different from other systems because it applies multiple algorithms to identify  
112 materials expressed in the spectra, evaluating the results of those algorithms to make decisions,  
113 including identifications, and applying additional algorithms, as needed, to solve specific problems  
114 based on results of the previous analysis. The results of these decision processes could be continued  
115 with application of additional algorithms and decisions. In theory, there is no limit to the number of  
116 algorithm/decision cycles that can be handled by Tetracorder.

117

118 In traditional remote sensing analyses, an algorithm may be applied to return a score with the result  
119 referred to as a “classification.” The algorithm may be applied multiple times, but each classification  
120 image is usually not compared with others. Tetracorder applies multiple algorithms to characterize  
121 components of a spectrum, and then compares the results to make decisions to derive the best answers.  
122 Each spectral range has different sensitivity, thus multiple compounds may be identified from one  
123 spectrum.

124

125 Tetracorder also employs data from other sources, in addition to spectra, e.g., temperature and pressure,  
126 if available, to further constrain identifications. In that sense, Tetracorder is an “algorithm to apply  
127 algorithms” through commanding by an expert system. Tetracorder benefits from ~35 years of  
128 development by a team of expert spectroscopists at the U.S. Geological Survey, and more recently, at  
129 the Planetary Science Institute with additional collaborators at other institutions who contributed to the  
130 expert system.

131

132 Tetracorder uses knowledge bases of spectral libraries for comparison to unknown spectral features in  
133 measured spectra. The spectra, both spectral library entries and the measured spectra, are split into  
134 different wavelength-range intervals, called groups (Table 1) and each group is analyzed independently.  
135 Within a group, each measured spectrum has multiple algorithms applied to it when comparing spectral  
136 features to a potential match from the spectral library. The routine may be as follows for one measured  
137 spectrum and one spectral library entry for one spectral region, for example:

138

139 spectral feature fit, feature 1,  
140 spectral feature fit, feature 2,  
141 spectral feature fit, feature 3 etc.,  
142 “not” features (features that should not be present).

143

144 For each of the above features, there can be additional algorithms applied to constrain identifications:  
145     Shoulderness constraints,  
146     Slope constraints,

147 Threshold constraints,  
148 Reflectance times band depth constraints,  
149 Diagnostic feature constraints,  
150 Optional feature constraints,  
151 Must have feature constraints, and  
152 Weak feature constraints.  
153

154 Then after the above are completed, additional algorithms are applied:  
155 Weighted band depth calculation,  
156 Weighted correlation coefficient calculation (the “fit”),  
157 Weighted fit times band depth calculation.  
158 Correlation coefficient constraints,  
159 Temperature stability constraints,  
160 Pressure stability constraints, and  
161 Apply special cases as needed.  
162

163 The result of applying all these algorithms is a fit score. Once all spectral library entries in the expert  
164 system are tested against the measured spectrum within one group (a spectral range), where each  
165 library entry can have different parameters to all the above algorithms, the fits for all entries are  
166 compared and the best match chosen as the answer. Each spectral region (group) analysis can detect  
167 different components, including mixtures. If a chosen answer needs additional clarification, the special  
168 case test can be invoked, called cases. Cases can trigger additional cases with no limit (except for  
169 compile time memory declaration of array sizes).  
170

171 Tetracorder is one subsystem of the SPECtrum PRocessing system, SPECPR. SPECPR (Clark, 1980,  
172 1993) and is a comprehensive spectral analysis system. It includes free-format subroutines for user  
173 input, as well as input/output to binary-format SPECPR spectral data files. The U.S. Geological  
174 Survey spectral libraries (e.g., Library06: Clark et al., 2003; Library07: Kokaly et al., 2017) are stored  
175 in SPECPR format and Tetracorder only reads SPECPR format for reference spectra. Tetracorder uses  
176 SPECPR routines to parse the expert system and read reference spectra. SPECPR, Tetracorder source  
177 codes, the expert system and its needed spectral libraries are available at  
178 <https://github.com/PSI-edu/spectroscopy-tetracorder>

179

180 Because of the broad diversity of research by those who have contributed to Tetracorder development,  
181 the Tetracorder expert system has been designed to work on surfaces throughout our Solar System (e.g.  
182 Clark et al., 2003, 2015, 2016, illustrated in Figure 1), and the same expert system can be used with any  
183 spectral range and resolution (Tetracorder version 5.1+). Tetracorder 5+ mapping results are  
184 automatically analyzed and color-coded maps are automatically produced (e.g., Figures 1a, 1b).  
185 Tetracorder produces maps of hundreds of materials, including chemical substitutions in some  
186 minerals. Tetracorder results could be fed to other systems, e.g., real-time robotic systems to guide a  
187 robot to resources (In Situ Resource Utilization, ISRU). Indeed, a NASA project, Toolbox for Research  
188 and Exploration, TREX (Hendrix et al., 2023 and references therein update these), used Tetracorder for  
189 real-time field assessment by a rover (<https://trex.psi.edu/>).

191 Tetracorder solves the material mixture problem by using spectra of measured or computed mixtures,  
192 but only for overlapping absorption features that cannot be separated with continuum removal, thus  
193 greatly reducing the number of mixtures needed. For example, consider the narrow tremolite  
194 absorptions superimposed on the broad pyroxene bands in Figure 2. No reference mixture spectra are  
195 needed by Tetracorder, because a short continuum removal adequately isolates the different  
196 absorptions. Only if similar width absorptions overlap is a mixture analysis needed. For example, if the  
197 pyroxene in Figure 2 contained ice, which has a broad 2- $\mu\text{m}$  absorption, the 2- $\mu\text{m}$  ice band would  
198 overlap the 2- $\mu\text{m}$  pyroxene band and a set of mixture spectra would be needed by Tetracorder. The  
199 advantage of this strategy is that fewer mixtures are required, and computational time is reduced. Other  
200 solutions, e.g., linear equations of an areal mixture problem, involve a matrix inversion, where the  
201 compute time for a solution increases as the square of the number of endmembers. By including  
202 mixture spectra, areal, intimate, and molecular mixtures are well covered in Tetracorder, as are  
203 coatings, and the solution time grows linearly with the number of reference spectra.

204 The rapid response results were demonstrated with Tetracorder during the 2001 World Trade Center  
205 disaster and the 2010 Gulf of Mexico oil spill, where results were supplied to first responders within a  
206 few weeks, demonstrated that real-time results could soon be possible. Now with EMIT delivering data  
207 from the space station, and with rapid correction to surface reflectance using new atmospheric models  
208 (Thompson et al., 2018; Brodrick et al., 2023), material maps can be computed by Tetracorder within a  
209 few minutes per scene. Correction of EMIT data to surface reflectance currently takes about 1.5 hours  
210 on average on the EMIT team Beowulf cluster at JPL using 40 cores from 2 central processing units  
211 (cpu). Using the 5.27c1 expert system from github, a Tetracorder run takes about 0.22 hour using one  
212 cpu on the JPL computer (not including browse products which are not calculated on the EMIT team  
213 computer). EMIT reflectance cubes and Tetracorder products are delivered to the public via the USGS  
214 Land Surfaces Data Active Archive Center (LP-DAAC) typically within about one day of receipt of  
215 data from the Space Station. Users can run a full Tetracorder analysis on an EMIT reflectance scene on  
216 an I7-class cpu laptop (scenes with 1.5+ million spectra) in about 20 minutes, including browse  
217 products. Combining rapid production of calibrated surface reflectance (or apparent reflectance), with  
218 the atmospheric features removed, enables faster mapping of minerals and other components. As  
219 computers become faster, we are now able to generate near real-time results for identifying and  
220 mapping many compounds in imaging spectrometer data sets. On an I7 8<sup>th</sup> generation computer, over  
221 2000 spectra per second are analyzed with the Tetracorder 5.27c1 expert system, making real time  
222 analysis of spectra from a point spectrometer possible, and this is being done on the Carnegie Mellon  
223 Zoë rover and will be discussed further below.

224 Tetracorder has been used to analyze data from all over the Solar System, including mapping ice and  
225 other compounds on icy satellite surfaces in the Saturn (e.g., Clark et al., 2012 and references therein)  
226 and Jupiter (Carlson et al., 1996) systems, minerals on Mars (e.g., Hoefen et al., 2003; Miliken et al.,  
227 2008; Ehlmann et al., 2016 and references therein), and was critical in making the discovery of  
228 widespread water on the Moon possible (Clark, 2009; Pieters et al., 2009). Tetracorder has been used

229 for mapping minerals on Earth (e.g., Swayze et al., 2000, 2002, 2009, 2014; King et al., 1995; Livo et  
230 al., 2007). It was used in assessing the environmental damage from the World Trade Center disaster  
231 (Clark et al., 2001, 2006), the 2010 Deepwater Horizon oil spill (mapping organics) in the Gulf of  
232 Mexico (Clark et al., 2010b), and mapping ecosystems, e.g., mapping vegetation species, bacteria and  
233 grizzly bear habitat in Yellowstone (Kokaly et al., 2003, 2007). Derivative software using an early  
234 version of the Tetracorder algorithms and expert system coded in IDL has been used to map minerals in  
235 a entire country (Kokaly et al., 2013) based on a methodology of Tetracorder before groups and cases  
236 were added.

237 The results from all the above and many more studies (excluding oil spills) have been incorporated into  
238 a master expert system, now 5.27c1. That system is now being used to map materials on Mars with the  
239 CRISM instrument, the Moon with Moon Mineralogy Mapper, M<sup>3</sup>, and the Earth – a diversity of  
240 environments that required, all with no changes to the expert system. The Clark et al. (2010) oil spill  
241 expert system was a separate expert system, and an improved version is under development (Swayze et  
242 al. In preparation). The Cassini Visual and Infrared Mapping Spectrometer (VIMS), orbiting Saturn  
243 from 2004 to 2017 used a custom expert system designed for cold ice signatures, and this expert system  
244 will be brought up to date for the Europa Clipper mission to Jupiter and Jupiter’s moon Europa,  
245 scheduled for launch in 2024.

246

## 247 **History of Tetracorder**

248 The Tetracorder system (Clark et al., 2003), initially developed by a team at the U.S. Geological Survey  
249 over ~25 years (~1989 - 2014), is an expert system that can analyze multiple inputs to make  
250 identifications and decisions. The main development for Tetracorder is now centered at the Planetary  
251 Science Institute (2014 to date). The most recent version (5.x) of Tetracorder (Clark et al., 2015, 2016)  
252 employs inputs from other analyses, e.g., temperature and pressure, to further constrain identifications.  
253 The system was also modified such that the system automatically adapts to the available data, including  
254 spectral range and resolution, and available physical inputs. As a result, the same expert system can be  
255 used throughout the solar system in many different environments and with spectrometers that cover  
256 different spectral ranges.

257 Work on early versions of Tetracorder (1990s) concentrated on adding reference spectra and testing  
258 different strategies for which continua to use (e.g., Swayze et al., 2003). The main result of that work  
259 was a set of spectra and spectral feature definitions that worked between terrestrial atmospheric  
260 absorption bands. These workarounds were also valid for spectra from Mars and the Moon or other  
261 atmosphere-less bodies. Groups (different spectral wavelength regions) were introduced in 1993 with  
262 the mapping of the Summitville, Colorado mine region (King et al., 1995).

263 Fuzzy logic (Figure 7) was introduced in version 3.7 of the expert system on May 11, 2001. Rather  
264 than hard thresholds for parameters, like continuum thresholds, correlation coefficient thresholds and  
265 others, fuzzy logic enables a smoother transition from full acceptance and no acceptance.

266

Over the summer of 2001, organics were added to the spectral library and to the Tetracorder expert system to aid in discrimination between organics and Mg- and Fe-OH bearing phyllosilicates that have similar position and shape absorption features in the 2.2 to 2.4- $\mu\text{m}$  region. At the time, work was being done to map asbestos-bearing rocks and soils in support of environmental sites (Clark et al., 1998, 2003; Livo et al., 2002; Swayze et al.; 2004a, b). This work led to the ability for a rapid response to the World Trade Center disaster in September 2001 with version 4.0 of the expert system and included mapping asbestiform minerals in the debris (Clark et al., 2001, 2006, Swayze et al., 2006). To map such minerals in the World Trade Center debris, a new spectral “shoulderness” algorithm (Figure 8) was introduced on September 10, 2001, with expert system 4.0a5, just before the World Trade Center disaster on September 11. Testing the new algorithm and expert system was done the evening of September 10, but test results were not examined until September 12 (on September 11, offices were closed). The test results were excellent and used for the 9/11 environmental assessments (Clark et al., 2001, 2006), but the sholderness algorithm was not well described until the 2010 Deepwater Horizon Gulf of Mexico oil spill in Clark et al. (2010). Shoulderness describes the asymmetric nature of an absorption prior to continuum removal, and the sholderness value is largely independent of abundance and particle grain size (unless the absorption becomes saturated).

The main work on Tetracorder shifted to the Planetary Science Institute in 2014 with Tetracorder version 5. From 2014 to 2019 work mainly included adding more groups, increasing the spectral range further into the infrared, and including groups that cover spectral regions not well sampled through the Earth’s atmosphere but are spectrally detectable wavelength ranges in the lab and on airless (e.g., satellites, asteroids), or low-pressure atmospheric (e.g., Mars) bodies. The groups and cases in the 2023 expert system 5.27c1, currently on Github, are listed in Table 1.

**Table 1. Current and planned groups and cases, Tetracorder Expert System 5.27c1**

group 0: catch for other declared groups  
group 1: electronic absorptions UV to  $\sim$ 1- $\mu\text{m}$  region  
group 2: 2 to 2.5- $\mu\text{m}$  region narrow absorptions (vibrational absorptions)  
group 3: vegetation detection  
group 4: broad absorptions in the 1.5-  $\mu\text{m}$  region  
group 5: broad absorptions in the 2-  $\mu\text{m}$  region  
group 6: 2.5-  $\mu\text{m}$  region  
group 7: 2.7 to 3- $\mu\text{m}$  OH region  
group 8: 2.7 to 2.8- $\mu\text{m}$  OH region narrow bands  
group 9: UV (0.1 - 0.3  $\mu\text{m}$ ), Future  
group 10: 3.5-  $\mu\text{m}$  region curved continua  
group 11: 3.5- $\mu\text{m}$  region linear continua  
group 12: unused, Future  
group 13: 1.3 to 1.4- $\mu\text{m}$  OH narrow  
group 14: 1.4 to 1.5- $\mu\text{m}$  OH  
group 15: 1.5-  $\mu\text{m}$  OH  
group 16: 1.5 to 1.6- $\mu\text{m}$  OH, Future

309 group 17: 1.7- $\mu$ m region CH and water, Future  
310 group 18: 1.8- $\mu$ m region, Future  
311 group 19: 1.9 to 2- $\mu$ m water and ice  
312 group 20: the search for rare-earth oxides  
313 group 21: the search for rare-earth oxide Neodymium  
314 group 22: the search for rare-earth oxide Samarium  
315 group 23: 3.8-  $\mu$ m region includes OD stretches, Future  
316 group 24: 4- $\mu$ m region  
317 group 25: 4.1- $\mu$ m region, Future  
318 group 26: 4.25- $\mu$ m CO<sub>2</sub> trapped, ice  
319 group 27: 4.5- $\mu$ m region includes sulfates  
320 group 28: 5- $\mu$ m region includes silicate overtones, Future  
321 group 29: 6- $\mu$ m region, includes H-O-H bends, Future  
322 group 30: 7 to 8- $\mu$ m region, Future  
323 group 31: 8 to 10- $\mu$ m region, Future  
324 group 32: 10 to 12- $\mu$ m region, Future  
325 group 33: 12 to 14- $\mu$ m region, Future  
326 group 34: 14 to 16- $\mu$ m region, Future  
327 group 35: 16 to 19- $\mu$ m region, Future  
328 group 36: 19 to 22- $\mu$ m region, Future  
329 group 37: Experimental: search for methane plume 2.3- $\mu$ m signatures  
330 group 38: Experimental: search for CO<sub>2</sub> gas, 2- $\mu$ m signatures  
331  
332 case 1: Vegetation red edge shift  
333 case 2: Vegetation spectral type  
334 case 3: Vegetation 0.9- $\mu$ m-band depth (water in vegetation)  
335 case 4: Vegetation 1.2- $\mu$ m-band depth (water in vegetation)  
336 case 5: Vegetation 1.4- $\mu$ m-band depth (water in vegetation)  
337 case 6: Epidote-Chlorite-Calcite mixture series  
338 case 7: Carbonate 2.3 plus 2.5- $\mu$ m feature detection  
339

## 340 **Tetracorder Algorithms**

341  
342 How Tetracorder operates is dictated by instructions in the expert system, also called the Tetracorder  
343 command file. At its highest level, Tetracorder identifies materials by comparing a remotely sensed  
344 observed spectrum (the unknown) to a large library of spectra of well-characterized materials, but we  
345 do so using several innovations to maximize accuracy and performance. The Clark et al. (2003) study  
346 was based on Tetracorder 3.5. This paper will review the main points of the previous paper for context  
347 and the added innovations since then.  
348  
349 While we describe the methodology used now and in the history of Tetracorder, we stress that this is  
350 not the only way Tetracorder can be commanded; it is the way we have developed the system using our  
351 collective decades of experience. Tetracorder could be commanded differently. For example, given  
352 the Spectral Angle Mapper (SAM) algorithm, Tetracorder could be commanded to produce the same  
353 output as SAM in the commercial software ENVI.  
354

355 We developed the expert system to isolate and analyze spectral features, and to group these analyses for  
356 different spectral regions (Table 1). Specifically, we target diagnostic absorption features that are  
357 unique to particular materials in shape (variation in intensity with wavelength over a narrow interval)  
358 and position. Between diagnostic features are portions of the spectrum that contain little information  
359 specific to the material of interest, but being relatively more transparent, are susceptible to absorption  
360 by other components in the spectrum of the measured surface. The focus on diagnostic spectral  
361 features in analyses of natural scenes is critical because mixtures which obey nonlinear systematics  
362 (e.g., coatings, intimate mixtures, solid solutions) are common in the natural environment and frustrate  
363 simple matching of spectra (Clark et al., 2003 and references therein).

364

365 In Tetracorder, each comparison of an unknown to a reference spectrum is highly tailored to the  
366 chemistry of the reference material by focusing on diagnostic spectral features (Figures 3a and 3b).  
367 Tetracorder identifies materials by comparing them to a large spectral library and continuum-removing  
368 and comparing the diagnostic spectral features between the unknown and library known spectra.  
369 Material spectral signatures are most significant over their diagnostic wavelength ranges and a different  
370 wavelength range may allow detection of additional materials in a remotely sensed spectrum (Clark et  
371 al., 2003). For example, the red spectrum in Figures 3a and 3b shows absorptions at the shorter  
372 wavelengths due to hematite and at longer wavelengths due to kaolinite. Tetracorder mitigates false  
373 identifications caused by spectrally similar materials by quantitatively comparing the degree of  
374 similarity of an unknown to a set of spectrally similar reference spectra. Tetracorder mitigates  
375 coincidental false alarms permitted by our specific implementation of our shape-matching algorithm by  
376 including ancillary information, including constraints on spectral structure, and physical limits such as  
377 pressure and temperature stability (described below). Finally, Tetracorder is not forced to provide a  
378 solution; it allows “No Answer” as an answer. The “No Answer” level strategies were guided using  
379 information from Swayze et al. (2003) who studied the identification accuracy as functions of sampling  
380 interval, bandpass width, and signal-to-noise ratio of spectral features.

381

382 **Continuum Removal Algorithm.** In order to identify a spectral feature by its wavelength position  
383 and shape, it must be isolated from other effects, such as reflectance-level changes and slopes due to  
384 other absorbing (or emitting) materials. The first step in such isolation is continuum definition and  
385 removal (Clark and Roush, 1984). In the Clark et al. (2003) paper, Tetracorder 3.5 only applied linear  
386 continua. Tetracorder 5 was improved to use curved, as well as linear continua. Continuum removal  
387 examples are shown in Figures 3a, 3b, 4a, and 4b for several spectral features. A continuum is removed  
388 by division (Figure 5) in reflectance, transmittance, and emittance spectra because of exponential  
389 absorption and scattering processes (Clark and Roush, 1984). Conversely, a continuum should be  
390 removed by subtraction with absorbance or absorption coefficient spectra because multiple components  
391 are additive.

392

393 Straight-line continua can have a disadvantage when the feature depth is weak and superimposed on a  
394 larger curved background continuum. Such situations can induce false positives or false negatives  
395 (Figure 6). Tetracorder allows a 4-point continuum to be defined (Figures 6, panels C and E), for  
396 example the two-point continuum shown in Figures 3 – 5, plus an additional 2 wavelength intervals,  
397 one on each side. A cubic spline is fit through the four points and the spectrum is divided by the spline  
398 (Figure 6). The disadvantage of the 4-point continuum is that if one continuum interval falls in another  
399 absorption band, it can cause wild swings in the fitted spline and induce both false positives and false  
400 negatives. In a future version of Tetracorder, we plan on including an upper hull continuum, but this is  
401 computationally expensive compared to existing calculations. We have limited the use of curved

402 continua in Tetracorder 5.27 to spectral features and regions where interference from other absorptions  
403 is less likely.

404  
405 To isolate and identify absorption features, the continuum removal algorithm first removes a  
406 continuum from a library reference spectrum and from the observed spectrum using a wavelength  
407 interval on each side of the absorption feature that is to be mapped (Figures 3a, 3b, 4a, and 4b). This  
408 can be described mathematically by:

409

$$410 L_c(\lambda) = L(\lambda) / C_l(\lambda) \quad \text{and} \quad O_c(\lambda) = O(\lambda) / C_o(\lambda), \quad (\text{eqns 1a and 1b})$$

411

412 where  $L(\lambda)$  is the library spectrum as a function of wavelength,  $\lambda$ ,  $O$  is the observed spectrum,  $C_l$  is the  
413 continuum for the library spectrum,  $C_o$  is the continuum for the observed spectrum,  $L_c$  is the  
414 continuum-removed library spectrum, and  $O_c$  is the continuum-removed observed spectrum.

415  
416 **The Shape-Matching Algorithm** was described in detail by Clark et al., (2003).

417  
418 The apparent depth of an absorption feature,  $D$ , relative to the surrounding continuum in a  
419 reflectance or emittance spectrum (Clark and Roush, 1984) is:

420

$$421 D = 1 - R_b/R_c \quad (\text{eqn 2})$$

422

423 where  $R_b$  is the reflectance at the absorption-band center (the minimum in the continuum-removed  
424 feature), and  $R_c$  is the reflectance value of the continuum at the wavelength of the band center (Figure  
425 5). For an absorption feature, depth,  $D$ , is positive. Tetracorder's expert system can also define  
426 "emission" features, in which case  $D$  is negative. Emission is used loosely here, as any upward-convex  
427 feature after continuum removal is considered an "emission" feature. Whether a spectral feature is  
428 declared an absorption or emission is dependent on the continuum-removed library reference feature.  
429 Identification of a material can use a combination of absorption (positive depth value) and "emission"  
430 (negative depth value) features.

431  
432 The Tetracorder shape matching algorithm is carried out in a two-step process. First, the local spectral  
433 slope (the "continuum") is estimated and removed both from the reference and observed (unknown) by  
434 fitting the continuum over a diagnostic spectral region (or regions) of these spectra, then dividing these  
435 continuum lines out of the observed and reference spectra (equation 1a, 1b).

436  
437 Because of the near-universal weakness of remotely sensed features relative to those of pure materials,  
438 the intensity of the features must also be normalized prior to comparison. The Tetracorder feature-  
439 fitting algorithm normalizes the intensity of the reference to that of the unknown by changing the  
440 spectral contrast of the continuum-removed reference over the diagnostic range to best match the  
441 continuum-removed unknown spectrum over the same range (Figures 4a and 4b). The continuum-  
442 removed depth (which we call "spectral contrast") of an absorption feature in a reference library  
443 spectrum can be modified by a simple additive constant,  $k$ , so that a shape match between the unknown  
444 and reference feature can be calculated. We simultaneously perform a comparison between reference  
445 and unknown by determining the contrast that maximizes the correlation between reference and  
446 unknown. Equation 3 governs this process:

447  
448

449  $L_c' = (L_c + k) / (1.0 + k)$ , (eqn 3)

450

451

452 where  $L_c'$  is the modified, continuum-removed spectrum that best matches the observed spectrum. If  $k$   
 453 is less than zero, feature strength (i.e., spectral contrast) increases; if greater than zero, feature strength  
 454 decreases. Equation 3 can be rewritten in the form:

455  $L_c' = a + bL_c$ , (eqn 4)

456 where

457  $a = k / (1.0 + k)$ , and (eqn 5)

458

459  $b = 1.0 / (1.0 + k)$ .  
 460 Equation 4 linearizes the spectral feature strength problem, so a direct solution can be found without  
 461 iteration. In Equation 4 we want to find the  $a$  and  $b$  that gives a best fit to the observed spectrum  $O_c$ .  
 462 The solution is found using standard linear least squares:

463  $a = (\sum O_c - b \sum L_c) / n$ ,

464  $b = \frac{\sum O_c L_c - (\sum O_c \sum L_c) / n}{\sum L_c^2 - (\sum L_c)^2 / n}$ ,

465 and

466  $k = (1 - b) / b$ , also:  $k = a / (1 - a)$  (eqn 6).

467

468 where  $n$  is the number of spectral channels in the fit.

469

470 Finally, the correlation coefficient,  $F$ , to the fit is derived for that feature:

471  $b' = \frac{\sum O_c L_c - (\sum O_c \sum L_c) / n}{\sum O_c^2 - (\sum O_c)^2 / n}$ ,

472  $F = (b b')^{1/2}$ . (eqn 7)

473

474 The *fit*,  $F$ , is a measure of how well the spectral features match. Tetracorder uses the highest fit value to  
 475 decide which spectral feature is best matched by a given library reference feature, independent of the  
 476 feature depth, and thus, independent of the abundance of the material. Figures 4a and 4b illustrate  
 477 graphically and numerically the matches between a remotely sensed spectrum and several Tetracorder  
 478 reference library mineral spectra.

479

480

481

482

483 **D, M, O, W Spectral Feature Importance.** Feature importance (as judged by the expert  
 484 spectroscopists) must be assigned to each library spectral feature to be matched by Tetracorder. Not all  
 485 features are equally important in spectrally identifying a material.

496  
497 D = A Diagnostic feature that must be present. If there are multiple, defined diagnostic features, only  
498 one of those diagnostic features must be present. The fit, depth, and fit\*depth must be above  
499 thresholds.  
500  
501 M = A “Must have diagnostic feature,” unconditionally. If only one diagnostic feature is defined,  
502 there is no difference between D and M designation. But if there is more than one diagnostic feature  
503 defined, the M designation requires that feature to be present even if there are other diagnostic, D,  
504 features detected. The fit, depth, and fit\*depth must be above thresholds.  
505  
506 O = An Optionally present feature. If an optional feature is not detected in the unknown’s spectrum,  
507 the reference spectrum’s fit and depth are set to zero but the material might still be identified by the  
508 presence of other absorption features, though the weighted fit may lower the score enough to cause that  
509 material to be rejected. Use of optional features should used sparingly. Swayze et al. (2003) showed  
510 that in some cases, including optional features may negatively impact identification when those  
511 optional features are weak relative to the background noise in an unknown’s spectrum.  
512  
513 W = A weak feature must be present, but the feature’s calculated area is set to zero so it has no effect  
514 on the fit, unless there is no detection. Noise can mask a weak band’s presence reducing detection even  
515 when a strong diagnostic band is present, so it is used only when necessary.  
516  
517 There is a speed advantage to listing diagnostic features first because if diagnostic features (D or M)  
518 are not detected, there is no point in computing O and W features.  
519  
520 D vs M details. The D is a diagnostic feature. When there are multiple diagnostic features defined,  
521 only one is needed to be enabled for a detection. In the case of azurite which has two important  
522 features, both are needed, but the band between 0.45 and 1.3  $\mu\text{m}$  is more important than the feature  
523 near 2.3  $\mu\text{m}$ , so it is marked M and listed first in the expert system entry for that mineral.  
524  
525 If one diagnostic (D) feature is disabled because of poor calibration over its spectral region, a second, if  
526 present, (or third) diagnostic (D) feature will still allow detection. This approach is different than if all  
527 diagnostic features are enabled, because in this case if one feature is not present (i.e., feature strength is  
528 zero or fit too low) then the material will not be found. On other words, all enabled diagnostic features  
529 must be present to allow identification.  
530  
531 The must be present (M) feature importance solves the problem of a disabled diagnostic (D) feature,  
532 requiring all M-declared features to be enabled and present. If one M feature is disabled, the material  
533 identification is disabled. This strategy was required for group 1 azurite, for example. The EMIT  
534 spectral range, after deleting intervals where the corrections for terrestrial atmospheric water  
535 absorptions were unstable, several minerals had features defined as diagnostic but were disabled for  
536 EMIT resulting in false identifications. Changing those required diagnostic to the must have (M)  
537 category solved the identification problem. For example, consider a mixture of chlorite + muscovite,  
538 vs goethite + muscovite. While the muscovite 2.2 and 2.3- $\mu\text{m}$  features are diagnostic of muscovite,  
539 what the muscovite is mixed with is dependent on the absorptions in the 1- $\mu\text{m}$  region. Those 1- $\mu\text{m}$   
540 absorptions need to be marked must have (M) features because if there were no 1- $\mu\text{m}$  features present,  
541 the mixture could be erroneously identified.  
542

543  
544 **Weighted Results Algorithm.** Tetracorder uses the relative areas (including the depths and widths) of  
545 continuum-removed-reference spectral features to compute a weighted *fit* that is used in the decision  
546 process. The continuum removal and feature *fits* to multiple features in a spectrum are illustrated in  
547 Figures 3a, 3b, 4a, and 4b. Three parameters for each spectrum are computed (equation 8): weighted  
548 *fit*,  $F_w$ , weighted *depth*,  $D_w$ , and weighted *fit times depth* (*fit\*depth*),  $FD_w$ . They are computed by  
549 weighting the relative areas of the absorption features of the reference library spectrum:

550  
551  
552       $F_w = \sum c_i F_i$ ,  
553       $D_w = \sum c_i D_i$ ,                and  
554       $FD_w = \sum c_i F_i D_i$ ,                (eqn 8)

555  
556 where “i” is the feature number,  $c_i$  is the relative fractional area of library reference features between  
557 each feature and its continuum:

558  
559       $\sum c_i = 1.0$ .                (eqn 9)

560  
561  $F_i$ ,  $D_i$  are the *fits* (the correlation coefficients) and *depths* of the corresponding features. The feature  
562 *depths* and relative feature areas are calculated from the fitted library reference features. The relative  
563 feature area is found by integration of the continuum-removed feature (the area between the  
564 continuum-removed feature curve and 1.0) divided by the sum of the areas of all features analyzed for  
565 each reference material.

566  
567 **Not-Feature Algorithm**

568  
569 A “not” feature is a feature that should not be present to identify a particular material. For example,  
570 both muscovite and illite have a ~2.2- $\mu\text{m}$  absorption feature that is very close to the same position,  
571 width and shape as an absorption feature in a montmorillonite spectrum, but both muscovite and illite  
572 also have a 2.3- $\mu\text{m}$  feature while montmorillonite does not (Figure 3b). In the identification of  
573 montmorillonite, the 2.2- $\mu\text{m}$  absorption feature is diagnostic but there also must not be a 2.3- $\mu\text{m}$   
574 muscovite/illite feature. Therefore, in the expert system’s feature definitions for montmorillonite  
575 entries, a pointer to the muscovite/illite 2.3- $\mu\text{m}$  absorption feature is defined and the presence of that  
576 feature relative to the strength of the 2.2 feature depth is defined. If a 2.3- $\mu\text{m}$  muscovite/illite feature is  
577 found above that relative depth and above the fit threshold, montmorillonite cannot be identified in the  
578 spectrum.

579  
580 **Continuum Thresholds**

581  
582 Continuum thresholds are used where a pure material has a limited observed reflectance. For example,  
583 green vegetation with significant water content has low reflectance in the 2 to 2.5- $\mu\text{m}$  region, and  
584 relatively low reflectance in the blue/ultraviolet. If continuum thresholds are defined, and the observed  
585 continua fall outside those thresholds, that material identification is rejected.

586  
587 Continuum thresholds are also set for minimum reflectance values below which noise dominates.  
588 These values are best set for the performance of individual spectrometers. For that case, the continuum

589 thresholds are made variables in the expert system and those variables can be simply modified in one  
590 location to customize specific spectrometers.

591 Fore example:

593 ct n1 n2 where ct means the minimum and maximum center continuum thresholds,

594 lct n1 n2 where lct means the minimum and maximum left continuum thresholds,

595 rct n1 n2 where rct means the minimum and maximum right continuum thresholds,

596 and where n1 and n2 are reflectance levels.

## 597 598 **Spectral Constraint Algorithms and Fuzzy Logic**

### 599 600 **Fuzzy Logic Algorithm**

601 Fuzzy logic modifies the fit values so that it is not a simple on or off hard limit. The fuzzy logic  
602 algorithm is described in Figure 7. Fuzzy logic can include either 2 or 4 parameters (Figure 7). With  
603 two values, it is a lower limit, with 4 it is a lower and upper limit. Fuzzy logic is a way to degrade a fit  
604 value as the probability of a spectral parameter indicating the match to a specific material is less likely.  
605 There is no hard rule; these levels are set through experience of the experts programming the expert  
606 system after running tests with multiple spectra and imaging spectrometer data sets covering different  
607 geologic environments.

608

609

610

### 611 **Continuum Ratio Algorithms with Fuzzy Logic**

612 613 lct/rct> n1 n2 where n1 n2 are positive real numbers

614 rct/lct> n1 n2 where n1 n2 are positive real numbers

615

### 616 **Shoulderness Algorithms with Fuzzy Logic**

617

618 Shoulderness (Figure 8) describes the continuum level relative to the spectral feature band bottom.  
619 There are 4 potential conditions, two each for right shoulderness (rcbbLC), and two for left shoulderness  
620 (lcbbRC). The Tetracorder keywords are:

621 622 rcbbLC> n1 n2 where n1 n2 are the fuzzy logic values,

623 rcbbLC< n1 n2 where n1 n2 are the fuzzy logic values,

624 lcbbRC> n1 n2 where n1 n2 are the fuzzy logic values, and

625 lcbbRC< n1 n2 where n1 n2 are the fuzzy logic values.

626

### 627 **Reflectance times Band Depth with Fuzzy Logic**

628

629 A potential spectral match can be constrained by reflectance times band depth, r\*bd, with fuzzy logic.

630

631 r\*bd> n1 n2 where n1 n2 are the fuzzy logic values.

632

### 633 **Feature Ratio Constraints with Fuzzy Logic**

634

635 Spectral feature band depth ratios can be constrained, Tetracorder keyword = fratio.

636  
637      constraint: fratio: a / b = n1 n2 m1 m2 where a, b = spectral feature number  
638  
639

## 640      Fit Constraints Algorithms with Fuzzy Logic

641  
642      There are nine constraints on the output fit, depth and fit\*depth images, each with fuzzy logic:

643  
644      constraint: FIT>      n1 n2    fit threshold, apply to fit value,  
645      constraint: FITALL>    n1 n2    fit threshold, apply to fit, depth, fit\*depth values,  
646      constraint: DEPTH>    n1 n2    depth threshold, apply to depth value,  
647      constraint: DEPTHALL> n1 n2    depth threshold, apply to fit, depth, fit\*depth values,  
648      constraint: DEPTH-FIT> n1 n2    fit threshold, apply to depth value,  
649      constraint: FD>        n1 n2    fit\*depth threshold, apply to fit\*depth value,  
650      constraint: FDALL>    n1 n2    fit\*depth threshold, apply to fit, depth, fit\*depth values,  
651      constraint: FD-FIT>    n1 n2    fit threshold, apply to fit\*depth value, and  
652      constraint: FD-DEPTH> n1 n2    depth threshold, apply to fit\*depth value.  
653

654      If the parameter, e.g. band depth, fit, or fit\*depth value falls outside the allowed range the indicated  
655      parameters are set to zero. If it is within the n1 to n2 range, it is decreased by linear interpolation as  
656      indicated in Figure 7. For example, if the correlation coefficient, the fit, is 0.8 and FITALL> n1 and n2  
657      values are 0.7 and 0.9, this falls mid-way between 0.7 and 0.9, and the fuzzy logic multiplier would be  
658      0.5. Then the fit, depth, and fit\*depth values would each be multiplied by 0.5. These modified values  
659      would next be used in comparison with those from other materials to determine the best match.

## 660 661      Physical Constraints Algorithm with Fuzzy Logic

662  
663      The temperature and pressure range over which a material is stable, or metastable can be constrained.  
664      For example, liquid water is stable over the temperature range 0 to 100° C at Earth's atmospheric  
665      pressure. On Mars liquid water is not stable due to the low atmospheric pressure. Therefore, we  
666      constrain liquid water with the following fuzzy logic limits, (n1, n2, m1, m2 defined in Figure 7):  
667

668      Temperature: C n1 n2 m1 m2

669      Pressure: bar n1 n2 m1 m2

670  
671      For example:

672  
673      Temperature: C -10    -5    99 105

674      Pressure: bar 0.10 0.20 98 99.

675  
676      Setting broad limits beyond the actual stability field is done to reflect uncertainty in the estimated  
677      temperature. If we had precise temperature and pressure for every pixel in a scene, the values could be  
678      more restrictive. But even with precise temperature, there could be sub-pixel effects. For example, a  
679      patch of snow could be sub pixel, with the other materials in the pixel warmer and above the freezing  
680      point. Including some additional range helps to account for these problems. This model is simple but  
681      effective. Temperature can be specified in Centigrade or Kelvin.  
682

683 To be more precise, a phase diagram needs to be encoded. This simplistic method currently in place  
684 adequately (and correctly) rejects liquid water on Mars, the Moon, and other airless bodies. It does not  
685 do as well for discriminating between liquid water and ice in a terrestrial scene with mountains and  
686 valleys where temperatures can cover a large range and where there is no temperature information with  
687 the imaging spectrometer data.

688  
689 Not all imaging spectroscopy data has temperatures and pressures measured. The user determines at  
690 run time the plausible ranges of temperature and pressure for the data set. For example, the Moon may  
691 have temperatures in the 200 to 400 Kelvin range, and pressure essentially zero. A typical terrestrial  
692 scene with desert and mountains could be in the range -20 to 40 C. With such large ranges of plausible  
693 temperatures, liquid versus solid water could not be determined by temperature, but pressure  
694 constraints could restrict the solution, with the Moon rejecting liquid water. Some minerals shift  
695 absorption band positions with temperature, and the temperature constraints can be used to restrict  
696 solutions. For example, ice measured at 80 Kelvin is plausible to Saturn's rings and satellites, but not  
697 for terrestrial snowpacks. The temperature constraints help determine solutions that are plausible for  
698 the physical environment.

699  
700  
701 **Normalized Vegetation Red Edge Shift, NVRES**  
702

703 The wings of absorption bands change with a variety of conditions. For example, see Figure 2, top, and  
704 notice that the width of absorptions change with particle size, which reflects changing scattering and  
705 mean optical path length through the material. Now look at only the right half of the absorptions in  
706 Figure 2, top. The absorption's edge position from the absorption minimum to the continuum changes  
707 with particle size.

708  
709 The position of an absorption edge, e.g., the chlorophyll absorption near 0.7  $\mu\text{m}$  can also shift with  
710 chlorophyll content, vegetation type, and health (e.g., Clark, 1999, Clark et al., 2003 and references  
711 therein).

712  
713 In vegetation, the chlorophyll absorption edge is near 0.7  $\mu\text{m}$  (Figure 9a, 9b) and because there are  
714 other absorptions at shorter wavelengths, the short wavelength side of the absorption is not seen well.  
715 Therefore, the red-edge position is used. The Tetracorder NVRES algorithm normalizes the depth from  
716 0.75 to 0.68  $\mu\text{m}$  with the reference spectrum, ratios to the reference spectrum, and uses the shape-  
717 matching algorithm described above to determine the magnitude of the shift relative to the reference  
718 spectrum using the ratio, and reference ratios stored in the spectral library. In order not to be confused  
719 by mineral absorptions, the red-edge position is only determined after a chlorophyll absorption has  
720 been identified successfully, and then a special case is triggered to run the NVRES algorithm. In the  
721 current expert system, a lawn-grass spectrum is used that has the strongest chlorophyll absorption in the  
722 reference library and the longest wavelength for the red-edge position.

723  
724  
725 **Example Tetracorder Output and Expert System Entry**  
726

727 Example Tetracorder output is shown in Figures 10, 11a – 11g. A single mineral detection is shown in  
728 Figure 10. Figures 11a – 11d show mineral products, coded by color, and Figures 11e – 11g show

729 vegetation products. The vegetation products in Figures 11e – 11g are only calculated as special cases  
730 after chlorophyll has been detected. The red edge position is shown in Figure 11g.

731  
732 An example Tetracorder expert system entry is shown in Table 2. An entry starts with a group or case  
733 number. Table 1 shows an entry for Group 1. The second line turns on or off the entry. If you want to  
734 experiment with effectiveness of an entry, and turn it off, it is simple to change to “use= no” instead of  
735 deleting all the lines for that entry. The “udata” line tells what the analysis should cover, and in this  
736 case, the data should be in reflectance. Future uses for this variable could be emittance and data  
737 converted on the fly to what is needed, e.g., convert emittance data to reflectance if the library entry is  
738 in reflectance. But Tetracorder 5.27 currently has all udata in reflectance.

739  
740 The convolve line is a placeholder for the future to run spectral library convolutions during analysis.  
741 Early experiments showed we need the convolved libraries for post Tetracorder analysis and  
742 comparisons in scientific papers, so this convolution is currently not done. The placeholder remains in  
743 case a future spectrometer has varying wavelengths within a scene (e.g., large spectral smile) where  
744 such convolutions would become necessary.

745  
746 Preratio and preprocess lines are used in some cases, for example, in the vegetation red-edge position  
747 calculations. In such calculations, the unknown is divided by a reference spectrum in the preprocess  
748 step and the shape and magnitude of features in the ratio are analyzed.

749  
750 The algorithm keyword selects the algorithm to be applied, and tricorder-primary applies equations 1 –  
751 9. ID= needs to be a unique identifier. It can be the same as the output base file name.

752  
753 The “define library records” defines which library spectra to use. Tetracorder 5.27 can use up to three  
754 reference library spectra for different spectral features, and would be coded as spectrum a, b, or c. For  
755 example, one reference spectrum could be from a Visible-Near-IR spectrometer, (a), and another from  
756 an FTIR spectrometer in the further infrared (b). Then the “a” or “b” selects which reference spectrum  
757 to use for each feature. The spectral ID is the specpr format convolved library reference file and the  
758 record number where the spectrum is found. Spectral libraries use the fixed record length specpr  
759 format, but different length spectra can span across different numbers of records. The scripts that build  
760 the convolved library pad the records to keep all spectra up to a certain number of channels with the  
761 same record number. The SMALL keyword is for spectra up to 2171 channels. Next is an information  
762 title.

763  
764 The “define features” section contains the feature definitions and constraints on those features. The  
765 “define constraints” are constraints applied to the weighted fit, weighted depth and weighted fit times  
766 depth results. The “define output” section defines which files to output in imaging mode, the integer  
767 bits per channel (8 or 16), and how to scale the floating-point results to the integer image data. In  
768 single spectrum mode, the “define output” section is not used and the floating-point results are  
769 reported.

770  
771 Finally, the “define actions” block describes what analyses or other tasks to do next if this material  
772 passes all the tests and is identified as the best answer for this group. The sound1 action announces the  
773 answer in single spectrum mode. The idea for sound is when operating a spectrometer in the field,  
774 Tetracorder can announce the results so that the operator does not have to look at a computer screen  
775 that can be difficult to see in bright sun.

776  
 777 **Table 2. Example Tetracorder 5.27 Expert System Entry**  
 778  
 779 group 1  
 780 use= yes        \# yes or no,    if no, skip this entry.  
 781 udata: reflectance  
 782 convolve: no  
 783 preratio: none  
 784 preprocess: none  
 785 algorithm: tricorder-primary  
 786 ID=hematite.fine.gr.gds76  
 787  
 788 define library records  
 789    a SMALL: [sprlb06] 744 d        \# file ID, rec no. 1 to 2171 channels  
 790 endlibraryrecords  
 791 \#===== TITLE=Hematite.02+Quartz.98 GDS76 W1R1Ha  
 792 [DELETEPTS]  
 793 Fe3+ hematite fine grain + qtz GDS76                    \# output title  
 794  
 795 define features  
 796    f1a DLw 0.4400 0.4550 0.6117 0.6315 ct [CTHRESH4] rct/lct> 0.9 1.1  
 797    f2a OLw 0.7375 0.7645 1.0500 1.0700 ct [CTHRESH4] rct/lct> 0.4 0.6  
 798 endfeatures  
 799  
 800 define constraints  
 801    constraint: FD-FIT>[GLBLFDFIT] DEPTH-FIT>[GLBLDPFIT]  
 802    constraint: FITALL>[GLBLFITALL]  
 803 endconstraint  
 804  
 805 define output  
 806    output=fit depth fd  
 807    fe3+\_hematite.fine.gr.gds76                    \# Output base file name  
 808    8 DN 255 = 0.5000  
 809    compress= zip  
 810 endoutput  
 811  
 812 define actions  
 813    action: sound1  
 814    action: none  
 815 endaction  
 816

---

817 In the define features section, features to be analyzed begin with "f" followed by a feature number.  
 818 Next is D, O, W, or M for diagnostic, optional, weak, or must have, as defined above.  
 819 Next is L or C for linear or curved continua. The "w" means the following continuum  
 820        points are in wavelength (same units as the wavelength file).  
 821 After the continuum wavelengths are feature constraints.

822

823

824 **Post-Tetracorder analysis of imaging data and browse products**

825

826 Work on post-Tetracorder analyses has been improved significantly starting in 2015 and continues to  
 827 date. The problem with imaging spectroscopy is the potentially overwhelming number of identified  
 828 products. For each Tetracorder reference material, three image products are produced: a band depth  
 829 image, a correlation coefficient image (called the fit), and a fit\*depth image. Each of these products  
 830 are weighted by the area of the spectral features used for the identification. With hundreds of reference  
 831 spectra, the end-user can be overwhelmed by the many hundreds of output image products. Previous to  
 832 circa 2014, each of the output images needed to be brought into an image processing program and  
 833 stretched to see what was found. This step took days of intense effort. To alleviate this problem,  
 834 browse products that pre-stretch the fit\*depth images are automatically created. The stretch uses the  
 835 same equations across different scenes, so that results from multiple scenes could be mosaicked  
 836 together.

837

838 Tetracorder expert system 5.27c1 contains 639 reference spectra over 23 active groups and 7 cases  
 839 (Table 1). With 639 reference spectra, Tetracorder generates 639 times 3, or 1917 output image files  
 840 (\*.fit, \*.depth, and .fd for fit \* depth). Each of these files are linear 8-bits/pixel images (Tetracorder  
 841 also can output 16-bit files, but we have found 8-bit to be adequate). Except for deep absorption bands,  
 842 an output data number, DN, level of 255 corresponds to band depth or fit \* depth of 0.5. This gives a  
 843 band depth resolution of 0.00196. These are settings in the expert system setup command file and can  
 844 be changed if the need arises, as described above.

845

846 With so many image files to evaluate, several quick-look reference files are created. A file called  
 847 “results” lists how many pixels were identified for each material. A geospatial cluster analysis is done  
 848 and a file named “results.cluster.sorted” is generated that puts the top scores for each group listed first,  
 849 with both quantitative cluster values and a qualitative descriptor to indicate the most significant  
 850 matches that likely are real detections, not noise. Next, for each fit \* depth file, the linear data is tone  
 851 mapped with the variable gamma equation similar to the tone curve employed in consumer digital  
 852 cameras:

853

$$854 x' = x * 7.5 * 0.08^{\sqrt{x/400}} \quad (\text{eqn 10})$$

855

856 where  $x'$  is image brightness on a 0 to 255.0 scale, and  $x$  is a 32-bit floating point number for the  
 857 calculation, which is then converted to an 8-bit integer for the output image. As seen by eqn 10 and  
 858 Table 3, the tone mapped values boost faint signals at the expense of compressing the brightest signals.  
 859 The constants were determined empirically by running equations with different constants and finding  
 860 ones with good representation of mapped results through visual judgment for the browse products.  
 861 This equation is a little less aggressive than what is performed on consumer digital camera images in  
 862 terms of boosting the low end and compressing the high end.

863

864

865 **Table 3 Tone map values from Equation 10**

x	x'
1	7
10	50
50	154
100	212
150	240
200	251
255	255

866

867 The tone-mapped fit \* depth image is written as a gif-format image, thus producing another 639 image  
 868 files with the 5.27c1 expert system. This approach still generates a lot of files to evaluate, and locating  
 869 mapped pixels on a black background often does not show context, thus another set of browse images  
 870 is produced: the mapped pixels for each identification converts the gif image to red and overlays it on a  
 871 gray-scale background (another 639 images). Sometimes it is hard to see the red pixels on the gray  
 872 background, so another set is made by putting the red on gray image alongside the gray scale gif image,  
 873 converting the set to RGB and outputting a jpeg format image (Figure 10), another set of 639 images.  
 874

875 Many reference materials are not found in a given image cube, so many images of these reference  
 876 materials are zero (non-detect) resulting in completely black images. Having many images with no  
 877 detections also takes time to review, so another set of images that only include some detections, like  
 878 shown in Figure 10, are copied into another set of directories, results.dual.group.\*.notzero. These  
 879 directories contain only images of detected reference materials.

880

881 The final set of browse products are summary products, where multiple materials are colored  
 882 differently and put on images beside a visible color RGB image. These images are located in  
 883 directories labeled: color.results, color.results+labels, and color.results+labels-jpegs. These images are  
 884 png format except for the jpeg-specific images that are smaller and therefore easier to email. Examples  
 885 are shown in Figures 11a-g and Figures 12a – 12d, 13a – 13d, and 14. The colored materials maps are  
 886 also suitable as figures in scientific reports.

887

888

889

890   **Real-Time Single Spectrum Mode**

891  
892   Tetracorder has two modes. The first, discussed above, analyzes an imaging spectrometer data cube,  
893   called “Cube Mode.” The second mode analyzes individual spectra, called “Single Spectrum Mode”  
894   (referred to here as SSM). SSM can have 5 output modes shown in Table 4.

895  
896   **Table 4. Tetracorder Single Spectrum Output Options**

Option	Action
0	(default) one-line answers only
1	abbreviated answers only
2	weighted fit + answer
3	for full diagnostic output: (individual fits, weighted fits and answer)
4	one-line answers to screen, and full diagnostic output to results file

897  
898   Options 0 and 1 provide quick results for the final answer with option 1 showing more information  
899   about the reference spectrum best match over option 0.

900  
901   Option 2 shows the weighted fit values for each reference material plus the option 0 ouput.

902  
903   Option 3 provides the full diagnostic output, with fit, and depth values for each spectral feature for each  
904   reference spectrum, then the weighted result of all reference spectra and rejection decisions. Use this  
905   output (or number 4) to understand how Tetracorder makes decisions.

906  
907   Option 4 is option 3 written to the file called “results,” and the option 0 results are written to the  
908   terminal window. Use this output (or number 3) for understanding how Tetracorder makes decisions.

909  
910   In addition to the above options, single spectrum mode can operate on a spectrum one at a time, or  
911   watch a growing file as new spectra are added. With the growing file option, option 4 is the preferred  
912   mode because the use of other options writes so much information to the terminal that it goes by too  
913   fast to read with about 1900 lines of diagnostic output. Option 4 provides the basic answers (about 16  
914   to 40 lines depending on the spectrometer spectral range), and the full diagnostic output written to the  
915   results file. Example output is shown in the SSERVI TREX section below.

916

917 **EMIT**

918  
919 The NASA Earth Surface Mineral Dust Source Investigation (EMIT), located on the International  
920 Space Station (ISS) is an imaging spectrometer covering the 0.38 to 2.5- $\mu\text{m}$  region in 285 bands with  
921 spectral resolution of 0.008 to 0.009  $\mu\text{m}$  Full Width at Half Maximum (FWHM). There are 1280 pixels  
922 cross track, approximately 60 x 60 meters per pixel, giving a width of about 77 km. The exact width  
923 and pixel footprint is dependent on the exact height of the ISS. Each scene has the atmospheric  
924 absorptions and scattering removed (Thompson et al., 2018; Brodrick et al., 2023), and the solar  
925 radiance corrected to derive apparent surface reflectance. The surface reflectance image cubes are  
926 analyzed by Tetracorder to deliver maps of minerals for use in climate change models to predict the  
927 radiative forcing impact of mineral dusts. But Tetracorder computes more than the small subset of 10  
928 minerals studied by the EMIT science team, including hundreds of minerals, vegetation (spectral type,  
929 water content, red-edge position of the chlorophyll absorption at  $\sim 0.7 \mu\text{m}$ , and non-photosynthetic  
930 vegetation), water, snow and melting snow, man-made materials, and some environmental materials.  
931 Example standard products are shown in Figures 12 – 14.

932 Example EMIT mineral maps are shown in Figures 12a, 12b, 12c, and 12d. Each color on these maps  
933 may represent multiple Tetracorder identifications that could be further split if the science need arises.  
934 For example, examine the green coded illite/muscovite in Figure 12c. The muscovite absorption near  
935 2.2  $\mu\text{m}$  shifts with aluminum substitution in the octahedral layer of the muscovite structure. This  
936 changing composition is shown in Figure 12d where low to high octahedral layer aluminum content is  
937 coded in different colors.

938 Vegetation, water, contaminants in water and snow and melting snow are assembled into a colored  
939 materials map, an example of which is shown in Figure 13a. The colors in this browse product are  
940 combinations from multiple Tetracorder entries and could be split further if needed.

941 Vegetation spectral type for the same scene as in Figure 13a is shown in Figure 13b. Only empirically  
942 determined spectral type rather than specific vegetation species is possible to map in the general case  
943 because the chlorophyll changes as a function of growing season, plus soil and water characteristics,  
944 adding complexity to species identification. The vegetation red-edge position is shown in Figure 13c  
945 and the water content in the vegetation is shown in Figure 13d.

946 Vegetation, water, ice and snow and melting snow for a different EMIT scene are shown in Figure 14.  
947 Here we see that at high elevations the snow is solid, but at lower elevations, it is melting. Repeat  
948 imaging with time could show the evolution of the snowpack with changing seasons.

949

950 **SSERVI TREX**

951  
952 Tetracorder has been installed on the Carnegie Mellon University Zoë rover (Clark et al., 2022) as part  
953 of the NASA Solar System Exploration Research Virtual Institute (SSERVI, <https://sservi.nasa.gov/>),  
954 Toolbox for Research and Exploration (TREX), a multi-institutional collaboration led out of the  
955 Planetary Science Institute (Hendrix et al., 2023 and references therein). Zoë is a solar-powered rover

956 capable of performing autonomous science operations (Wagner, et al., 2005, Wettergreen et al., 2005;  
957 Wettergreen et al., 2008; Vijayarangan et al., 2018). It carries an Analytical Spectral Devices ASD  
958 FieldSpec spectrometer, mounted on a pan-tilt unit, and can observe spectra at any point around the  
959 rover. The rover (Figures 15), and its data flow (Figure 16) includes and an ASD-spectrometer  
960 covering 0.35 – 2.5  $\mu\text{m}$  to provide real-time data as the rover drives autonomously. The rover also  
961 runs a second instance of Tetracorder to analyze FTIR data in the 2.5 to 5- $\mu\text{m}$  range.  
962

963 Zoë uses the Robot Operating System (ROS) from the Stanford Artificial Intelligence Laboratory,  
964 <https://www.ros.org>. ROS uses a message-passing system for communication between the different  
965 components in the system that enables each component to operate independently without having to  
966 know who or how many consumers are using the data produced by the components.  
967

968 Tetracorder analyzes the spectra real time with single spectrum mode and is described in Clark et al.  
969 (2023). Tetracorder output of a single spectrum analysis is in tabular form, and example analysis is  
970 presented in Figure 17 in graphic form to illustrate the features that Tetracorder analyzed. Another  
971 program monitors the Tetracorder tabular output and uses the identified minerals to assess the geologic  
972 origin of the area, updates a geologic-origin map and uses the information to plan a new route  
973 autonomously to explore the area (Candela et al., 2017, 2020; Noe Dobrea et al., 2022, 2023a, 2023b).  
974

975 Field tests were conducted in fall 2021 and fall 2022 on the Colorado Plateau (Clark et al., 2022, Noe  
976 Dobrea et al., 2022, 2023a, Clark et al., 2023). In 2022, additional spectrometers were employed as  
977 contact instruments, including an ASD spectrometer with a contact probe, and a contact FTIR  
978 instrument covering 2.5 to 15  $\mu\text{m}$ . The rover collected data from these instruments and sent them,  
979 along with imaging data to a remote server via satellite communication. This strategy simulated a rover  
980 on a remote body (e.g., the Moon, Mars, asteroid), or a remote location on Earth that may be hazardous  
981 for humans (e.g., an environmental disaster or volcano emitting toxic gases). The remote server ran  
982 three instances of Tetracorder for the three spectrometers giving a near real-time readout of what  
983 materials the spectra indicated were present. By near real-time we mean limited by communication  
984 delays, and the three second wait loop for checking for new spectra to arrive. The science team, at  
985 remote locations, could monitor the incoming images, spectra, and Tetracorder results real time (within  
986 data rate limitations; images sometimes took a while to download).  
987

988 Example Tetracorder output from two spectrometers deployed in the field are compared to XRD  
989 analyses of the same rock in Table 5, and the spectra are shown in Figure 17. The Tetracorder expert  
990 system in use included identifications from 0.35 to about 4.5  $\mu\text{m}$ . The results in Figure 17 and Table 5  
991 illustrate that different methods and wavelength ranges are sensitive to differing minerals and  
992 abundances. The XRD analysis found quartz, feldspar, and calcite. Nano-phase hematite is X-ray  
993 amorphous and undetectable by XRD. Reflectance spectroscopy is more sensitive to phyllosilicates  
994 than XRD, thus the illite/muscovite that was easily detected from the 2.2-2.3- $\mu\text{m}$  absorptions in the  
995 reflectance spectra was too low in abundance for XRD detection. But XRD has good sensitivity to  
996 quartz and feldspar, both of which are relatively transparent in the 0.4 to 4- $\mu\text{m}$  region. The weakness  
997 of the calcite absorptions near 3.5 and 4  $\mu\text{m}$  indicate low abundance of carbonate, that is too low to  
998 show absorptions in the 2.3- $\mu\text{m}$  region, especially with the strong phyllosilicate bands that are present.  
999 This example illustrates the power of extended spectral range beyond the 2.5  $\mu\text{m}$  limit, common in  
1000 terrestrial remote sensing studies.  
1001

1002 Tetracorder reported absorptions due to hydroxyl in the 1.4- $\mu\text{m}$  region and water in the 1.9- $\mu\text{m}$  region.  
1003 These absorptions may be diagnostic of mineralogy, but the Tetracorder 5.27 expert system needs  
1004 additional reference spectra added before unique mineralogy can be identified. Until those additions  
1005 are made, these 1.9- $\mu\text{m}$  absorptions are only identified by their band positions.  
1006

1007 Historically, the 2- $\mu\text{m}$  water absorption has received little attention as a feature to identify mineralogy  
1008 because the Earth's atmospheric water causes too much interference. However, the 1.4 and 1.9- $\mu\text{m}$   
1009 absorptions could be useful for studying airless bodies or planets with thin, dry atmospheres (e.g.,  
1010 Mars). Even terrestrial studies could be enhanced if this spectral range were acquired by *in situ*  
1011 instruments with a local light source, thus minimizing atmospheric path lengths. Different mineral  
1012 groups have varied hydrogen bonding, that shifts the position and width of the water absorptions  
1013 (Figure 18). In addition to the changing wavelength position and width of the absorptions plotted in  
1014 Figure 18, the band shapes, including asymmetry and shoulders from overlapping water absorptions  
1015 further distinguish the absorptions from different minerals, improving specific mineral identification.  
1016 Tetracorder reports the position of detected absorptions in the 1.9- $\mu\text{m}$  region (e.g., Table 5), and  
1017 indicates the mineral that is best matched, although the output is not always a unique identification  
1018 (e.g., Figure 19). With more reference spectra coded into the expert system, identification accuracy  
1019 might be improved, but this possibility needs additional study.  
1020

1021 **Table 5. Tetracorder and XRD results for sample T8 Spot 1.**

1022 XRD: Xrd\_2022\_1019\_022200\_s\_t08\_spot-ka\_tfb

1025 Quartz 90 %  
 1026 2:1 clay mineral -  
 1027 Kaolinite -  
 1028 Felspar 5  
 1029 Calcite 5  
 1030 Hematite -  
 1031 100 %

1032 Tetracorder single spectrum mode, ASD contact instrument:  
 1034 Spectrum: sps0051 312 ASD2\_20221019\_1500\_REFL\_T8\_Spot1

Grp/Cse	Material	Fit	Depth	F*D
grp 1	1um region 67 MATCHES: fe3+_hematite.nano.BR34b2b	0.7267	0.0757	0.0699
grp 2	2-2.5um 149 MATCHES: micagrp_illite.gds4	0.9681	0.0608	0.0599
grp 3	veg detect none			
grp 4	1.5um broad 322 MATCHES: fe2+_wollastonite_hs348.3b	0.7471	0.0397	0.0297
grp 5	2um broad none			
grp13	1.3-1.4 nrw 421 MATCHES: oh_1.406_silica-opal	0.9519	0.0648	0.0617
grp14	1.4-1.5 nrw 445 MATCHES: ohb_1.416_mica-roscelite	0.9922	0.0556	0.0552
grp15	1.5um OH 472 MATCHES: ohc_1.451_hydroxide-gibbsite	0.8091	0.0428	0.0346
grp19	1.9-2um H2O 489 MATCHES: water_1.910_halloysite	0.9944	0.2068	0.2056
grp20	rare-earth none			
grp21	Neodymium none			
grp22	Samarium none			

1048 Tetracorder single spectrum mode, FTIR instrument:

1050 Spectrum: sps0053 252 FTIR\_20221019\_134900\_T8\_Spot1\_10\_19\_2022

Grp/Cse	Material	Fit	Depth	F*D
grp 6	2.5um region 343 MATCHES: adularia_2.5um	0.7907	0.0266	0.0210
grp 7	2.5-3um 354 MATCHES: grossular_3.17um	0.7308	0.0929	0.0679
grp 8	3.2um region 358 MATCHES: oh2.76um_ref_illite_gds4	0.7769	1.0390	0.8072
grp10	3.5um curveC 367 MATCHES: carbonate_trace-b_3.4um.curv	0.9542	0.1703	0.1625
grp11	3.5um linear 386 MATCHES: carbonate_trace-b_3.4um_linc	0.9486	0.1593	0.1511
grp24	4-um region 530 MATCHES: carbonate_calcite_4um_linc	0.9786	0.2872	0.2810
grp26	4.25um CO2 539 MATCHES: trapped-co2-4.26um_ref-cordierite	0.5899	0.0141	0.0092
grp27	4.5um region none			

1061 Notes:

- 1062 Group 4 fe2+\_wollastonite is a shape match for a broad feature, not a specific mineral ID.  
 It is likely that the Fe<sup>2+</sup> feature is from the illite / muscovite.
- 1063 Group 13, 14, 15, 19 are feature position matches, not specific mineral IDs.
- 1064 Group 6 adularia\_2.5um is a shape match, not a specific mineral ID.
- 1065 Group 8 oh2.76um is a feature position match, not a specific mineral ID.
- 1066 The features are marked on spectra in Figure Z1.
- 1068 The Fit is the correlation coefficient to the least-squares fit to the reference spectral feature(s)
- 1069 Depth is the fitted depth, and F\*D is the weighted fits times depths of all the features used in the identification.

1071   **Abundances**

1072  
1073 Deriving abundances from remotely obtained reflectance spectra has been a difficult problem, due to  
1074 heterogenous particle sizes and non-linear spectral mixing, requiring inversion of radiative transfer  
1075 models using an iterative solution. The optical constants of all components in the surface are needed  
1076 for the general case. Particle sizes and the size distribution also needs to be known to iteratively solve  
1077 the radiative transfer models to derive abundances. Because of the non-linear iterative nature of the  
1078 radiative transfer model inversions, it is not feasible to apply this full solution to imaging spectroscopy  
1079 data that often includes millions of spectra. Therefore, various studies have used simpler solutions, for  
1080 example using linear mixture models that assume pure materials in spatially separate areas (i.e., the  
1081 “checkerboard” model). But there are other models, and here we describe four models that are  
1082 operational in the Tetracorder system and can be applied to imaging spectroscopy data. These models  
1083 were developed as part of the EMIT and FRAGMENT projects and are currently limited to the EMIT  
1084 10 minerals: hematite, goethite, calcite, chlorite, dolomite, gypsum, kaolinite, illite/muscovite,  
1085 montmorillonite, and vermiculite. Other minerals can be added.  
1086

1087   **Model 1:** Relative linear band depth as a proxy for abundance, popularly called “spectral abundance.”

1088   The measured band depth is compared to the band depth in the reference library and the library  
1089 sample’s known abundance. This model is a reasonable approximation if the albedo and  
1090 particle sizes of the remote surface are similar to the reference spectrum. Figure 20 shows  
1091 observed band depth for hematite at varying abundances and albedos.

1092 Note: Models 2-4 use solutions for Mean Optical Path Length, MOPL, derived by Clark and Roush  
1093 (1984). Absorption strength is a direct measure of the MOPL but requires accurate optical constants.  
1094

1095   **Model 2:** Absolute Abundance in a non-scattering 2-way slab model (Figure 21a). This model  
1096 requires optical constants for calculating the diagnostic absorption band centers and the  
1097 continuum wavelengths. Results are in mass per unit area in the optical surface, e.g., grams  
1098 per sq meter. The major remaining unknown is how deep is the actual optical layer and how it  
1099 varies from mineral to mineral.  
1100

1101   **Model 3:** Mass in the optical layer assuming isotropic random walk by photons (Figure 21b). Hapke  
1102 (1981) argued that after the first scatter, photon direction within a particulate surface is  
1103 randomized so an isotropic scattering assumption is a good approximation. Results are in mass  
1104 per unit area in the optical surface, e.g., grams / sq meter. The major remaining unknown is the  
1105 optical layer thickness and how it varies from mineral to mineral. This model requires optical  
1106 constants for calculating the diagnostic absorption band centers and continuum wavelengths.  
1107  
1108

1109   **Model 4:** Relative Abundance in the optical layer assuming isotropic random walk by photons with  
1110 estimates of particle sizes of quartz and feldspar, which are typically dominant in arid regions of  
1111 the Earth. This model solves the problem of depth of the optical layer in Model 3. Results are  
1112 fractional mass abundance on a 0 to 1 scale. This model requires optical constants for  
1113 calculating the diagnostic absorption band centers and each continuum, and the average particle  
1114 size of quartz and feldspar.  
1115

1116   **Model 5:** Full radiative transfer model with layers. This model is too computationally intensive for  
1117 inversion of a full radiative transfer scene but can be used on individual spectra.

1118  
1119  
1120 **Model 1 Relative Linear Band depth as a Proxy for Abundance.** The model scales band depth to  
1121 band depth of reference mineral and assumes linear scaling of this scaled band depth = relative  
1122 fractional abundance,  $F_A$ :

1123  
1124  $F_A = R_{AB} * BD_O / BD_R,$  (eqn 11)  
1125

1126 where:

1127  $R_{AB}$  = Reference material abundance in the reference spectrum,  
1128  $BD_O$  = Band depth in the observed spectrum (the unknown), and  
1129  $BD_R$  = Band depth in the reference spectrum.

1130 The band depth,  $BD_O$ , can be from a Tetracorder analysis.

1131  
1132 **Model 2 Slab Layer Mass.** The Mean Optical Path Length, MOPL, derives directly from Beers Law,  
1133 after Clark and Roush (1984, their equation 11):

1134  
1135  
1136  $R = e^{(-k*x)},$  (eqn 12)  
1137

1138 where

1139  $k$  = absorption coefficient (usually expressed in inverse centimeters).

1140  $x$  = path length through the material

1141 = Mean Optical Path Length in a scattering medium, MOPL.

1142  
1143  $-ln(R) = kx,$  and (eqn 13)

1144 Extending equation 13 using Clark and Roush (1984, their equation 30), multiple components would  
1145 have:

1146  
1147  
1148  $-ln(R) = k_1x_1 + k_2x_2 + K_3x_3 + \dots$  (eqn 14)

1149  
1150 Unfortunately,  $R$  is influenced by more than just a single material we are interested in. But we can  
1151 work around this problem by using continuum-removed band depths of diagnostic spectral features.

1152 Clark and Roush (1984, their equation 32) showed the band depth, BD, relative to the continuum is

1153  
1154  
1155  $BD = (R_c - R_b)/R_c = 1 - R_b/R_c,$  (eqn 15)

1156 where

1157  $R_c$  = reflectance of the continuum =  $\exp(-k_c * x_c),$

1158  $R_b$  = reflectance at the band center =  $\exp(-k_b * x_b),$

1159  $k_c$  = absorption coefficient of the continuum,

1160  $x_c$  = mean optical path length of the continuum,

1161  $k_b$  = absorption coefficient at the band center, and

1162  $x_b$  = mean optical path length at the band center.

1163  
1164

1165 Therefore,  
 1166  
 1167  $x = \ln(1-BD) / (-\Delta k)$ , (eqn 16)  
 1168 where  $\Delta k = k_b - k_c$  = delta absorption coefficient (Figure 22).  
 1170  
 1171 Depth probed for model 2, independent of other components, Figure 21a, is then  
 1172  
 1173  $T_{\text{slab}} = x/2$ . (eqn 17)  
 1174  
 1175 For 3 optical depths:  
 1176  
 1177 Model 2 Mass =  $3 * T_{\text{slab}} * (100^2) * \text{density}$ , (eqn 18)  
 1178 where density is in gm/cc and mass = grams per sq meter in optical layer.  
 1179  
 1180 Model 1 is used by the EMIT team for initial abundance delivery.  
 1181  
 1182 **Model 3 Random Walk Mass** is similar to model 2 but includes scattering in a random walk (Figure  
 1183 21b). Again, the MOPL is a direct calculation from equation 16. If we can constrain the grain size,  
 1184 e.g., derived from the shape of absorption bands (Clark, 1999, Clark et al., 2003 and references  
 1185 therein), we can compute the number of grains encountered in the random walk process using Clark  
 1186 and Roush (1984, their equations 16 and 19):  
 1187  
 1188  $m = \ln(R) / \ln(1/(1+2kD))$ , (eqn 19)  
 1189 where  $m$  = number of scatters,  $k$  = absorption coefficient, and  $D$  = distance between scatters.  
 1190 In model 3,  $D$  = grain diameter. The light penetration depth is then  
 1191  
 1192  $T = (\pi/4) * D * (m/2)^{1/2}$ , (eqn 20)  
 1193 and for three optical depths with density in gm/cc and the result in grams per sq meter in the optical  
 1194 layer is:  
 1195  
 1196 Model 3 Mass =  $3 * T * (100^2) * \text{density}$ . (eqn 21)  
 1197  
 1198  
 1199 **Model 4 Relative Abundances.** This model is designed to derive the fractional abundances of the  
 1200 EMIT 10 minerals. EMIT's goal is to derive mineralogy in the arid regions of the Earth to feed into  
 1201 climate change models for dust radiative properties. Terrestrial arid dust-generating regions commonly  
 1202 have a high component of quartz plus feldspar of larger grain sizes. There are usually no spectral  
 1203 features from quartz or feldspar in the visible-near-infrared spectral range making it difficult to identify  
 1204 and quantify their abundance directly from EMIT data. Instead, we use an estimate of the quartz plus  
 1205 feldspar particle (hereafter grain) size, and assuming that quartz plus feldspar, which are relatively  
 1206 transparent in the visible to 2.5- $\mu\text{m}$  spectral range, is a significant mass fraction of the soil/rock surface.  
 1207 We can use quartz plus feldspar grain diameter as a proxy for distance between scatterings from other  
 1208 mineral grains. For model 4, equation 20 becomes:

1212  
 1213  $T = (\pi/4) * D_q / n * (m/2)^{1/2}$ , (eqn 22)  
 1214  
 1215 where  $D_q$  is the quartz plus feldspar grain diameter and  $n$  = average number of mineral grains (e.g.,  
 1216 hematite) per quartz/feldspar grain. The value of “ $n$ ” needs to be derived with a model checked against  
 1217 observations or derived empirically for a given region. The  $D$  in equation 19 remains the grain  
 1218 diameter of the mineral whose mass is to be determined.  
 1219  
 1220 Using equation 22 in a model 3 mass calculation, the mass of quartz plus feldspar is derived using the  
 1221 value of  $m$  from equation 19 and  $D_q$ .  
 1222  
 1223 The relative abundance for component  $i$  of  $j$  total components is:  
 1224  
 1225  $M_{R,i} = M_i / (\sum_i^j (M_i))$ , (eqn 23a)  
 1226  
 1227 where Relative Mass is  $M_{R,i}$  of  $i^{th}$  component absolute mass  $M_i$ .  
 1228 The Tetracorder reference material parameters for computing the band depths for a given set of  
 1229 reference spectra are stored in ascii files that get parsed by the abundance programs. An example set  
 1230 for hematite includes 13 reference spectra covering four grain size ranges and is shown in Appendix 1,  
 1231 Table A1. The full tables are available on github in each tetracorder.cmds directory.  
 1232  
 1233 **Layered Regoliths and Contaminants.** A major physical characteristic observed on planetary  
 1234 surfaces, including in the Saturn system, Mars and the Moon, yet so far ignored by the remote sensing  
 1235 community is the changing grain size with depth in the regolith. The reason for ignoring this factor is  
 1236 mainly the lack of development of radiative transfer algorithms to handle layered media. Layered  
 1237 regoliths are directly imaged on the Earth, and also in rover tracks on the Moon (Figure 23) and Mars.  
 1238 For example, rover tracks on the Moon and Mars show darker regolith below a lighter surface. The  
 1239 lunar and Martian surfaces commonly are coated by finer grains (dust). This condition is also observed  
 1240 in the Saturn system as expressed by variations in band depths of the different intrinsic strength ice  
 1241 absorptions. An example model with grains increasing with depth is shown in Figure 24 with  
 1242 measured band depths in Table 6.  
 1243  
 1244 **Model 5: Layered Media and Abundances with Full Radiative Transfer Model.** Planetary surfaces  
 1245 can have different compositions and/or grain size at the surface, compared to deeper down (e.g., Figure  
 1246 23). Radiative transfer models need to include these changes with depth. Clark and Roush (1984)  
 1247 gave equations for penetration depths into a surface, and these equations have been added to the Clark  
 1248 *et al.* (2012) radiative transfer model that is based on Hapke (1980, 2012) with extensions for sub-  
 1249 micron particles and diffraction Clark *et al.* (2012).  
 1250  
 1251 This full radiative transfer model has been used in multiple studies, for example, Clark *et al.* (2012,  
 1252 2019) where it was used to model the ice in the Saturn system including complex darkening by  
 1253 contaminants. The mean penetration depth into a regolith is mainly a function of absorption  
 1254 coefficient, not wavelength (Clark and Roush, 1984). Using equations 18 to 24 from Clark and Roush,  
 1255 it was a simple extension to derive transmission, absorption, and reflections between multiple layers.  
 1256 An example 2-layer radiative transfer model is shown in Figure 24.  
 1257

1258 The radiative transfer code is based on the Hapke model (1980, 2012):  
 1259  
 1260  $r(w, \lambda, \mu_o, \mu, g) = (w/4\pi)[\mu_o/(\mu_o + \mu)]\{[1 + B(g)]P(g) + H(\mu_o)H(\mu) - 1\}$  (eqn 24)  
 1261  
 1262 where  $r$  is the reflectance (radiance factor) at wavelength  $\lambda$ ,  $\mu_o$  is the cosine of the angle of incident  
 1263 light,  $\mu$  is the cosine of the angle of emitted light,  $g$  is the phase angle,  $w$  is the average single scattering  
 1264 albedo,  $B(g)$  is a backscatter function,  $P(g)$  is the average single particle phase function, and  $H$  is the  
 1265 Chandrasekhar (1960)  $H$ -function for isotropic scatterers. When  $r > 0.9$ , Hapke's approximation of the  
 1266  $H$ -function shows considerable error and equation 24 deviates from measurements (Hapke, 1981, Clark  
 1267 1999). Because of this deviation, a table interpolation subroutine using "exact" values from  
 1268 Chandrasekhar (1960) is used. The table interpolation is computationally faster than the Hapke  
 1269 approximation and more accurate.  
 1270  
 1271 We extended the single scattering albedo calculation from Hapke (1980, 2012) to include diffraction  
 1272 effects when particles much smaller than the wavelengths are present (Clark et al., 2012). We use the  
 1273 scattering efficiency from Hapke (1993, p. 94), and adapt his equation (5.25):  
 1274  
 1275  $Q_s = Q_d + Q_s'$  (eqn 25)  
 1276  
 1277 where  $Q_d$  is the scattering due to diffraction, and  $Q_s'$  is the scattering from the particles not including  
 1278 diffraction ( $Q_s'$  computed using the standard Hapke model). For small particles, we implement  
 1279 equations (5.13) and (5.14) from Hapke (1993) for  $Q_A$  (absorption) and  $Q_s$  (scattering). The resulting  
 1280 single-layer model reproduces the spectral shapes of dark surfaces seen in the Visible and Infrared  
 1281 Mapping Spectrometer (VIMS) data for the Saturn system. The model computes both Rayleigh  
 1282 scattering and Rayleigh absorption (Clark et al., 2012).  
 1283  
 1284 The layered spectra and model shown in Figures 24 and 25 illustrates the basics for interpreting real  
 1285 planetary regoliths. Previously published results of relatively pure icy surfaces in the Saturn system  
 1286 never matched the intensity and shape of the 3 to 5- $\mu\text{m}$  region and the depths of the 1.04, 1.25, 1.5 and  
 1287 2- $\mu\text{m}$  ice bands at the same time (e.g., Ciarniello et al., 2017). When the longer wavelengths were  
 1288 matched, the shorter wavelength absorptions, especially the 1.04 and 1.25- $\mu\text{m}$  ice bands were too weak.  
 1289 However, the multiple layer regolith model (Figure 24, solid red line) solves the absorption-band-depth  
 1290 problem because where the absorption coefficients are smaller, light penetrates deeper. Where larger  
 1291 grains are encountered, there are deeper absorptions in the spectrum. Table 6 shows the quantitative  
 1292 band depths where in the 2-layer model the 1.04/1.5- $\mu\text{m}$  band depth ratio has been increased by over a  
 1293 factor of two over non layered models. As contaminant levels increase, e.g., as observed on Saturn's  
 1294 moon Phoebe, penetration depths (and layered-regolith effects) decrease, and non-layered radiative  
 1295 transfer models are adequate.  
 1296  
 1297 The multi-layer radiative transfer model has been coded and is operational since 2019. This improved  
 1298 model will lead to better accuracy in deriving material abundance as a function of depth, especially for  
 1299 ices that are more transparent. Given the above considerations, multi-stream calculation is performed  
 1300 between multiple layers, as illustrated in Figure 25. Through testing with ice optical constants, it has  
 1301 been determined that calculation to 4<sup>th</sup> order scattering between layers is sufficient, even for  
 1302 transparent-ice materials. At very low absorption coefficients (e.g., pure ice at 0.5  $\mu\text{m}$ ) with no  
 1303 contaminants in the surface, calculation to 6<sup>th</sup> order is needed.  
 1304

**Table 6. Multi-Layer Model**

	Band Depth				Depth Ratio
Model, g.d. = grain diameter	1.04 $\mu\text{m}$	1.25 $\mu\text{m}$	1.5 $\mu\text{m}$	2.0 $\mu\text{m}$	1.04 / 1.5 $\mu\text{m}$
H <sub>2</sub> O ice 2 layer g.d.= top: 28, 11 microns, bottom: 3.5, 2.1 mm	0.2014	0.3266	0.5713	0.4450	0.3526
<b>H<sub>2</sub>O ice 2-layer fine on coarse lab data</b>	<b>0.2178</b>	<b>0.3484</b>	<b>0.5462</b>	<b>0.4031</b>	<b>0.3988</b>
H <sub>2</sub> O ice 1 layer g.d.= 4 microns	0.0717	0.0190	0.3132	0.4142	0.2289
H <sub>2</sub> O ice 1 layer g.d.= 1.73 mm	0.1989	0.3815	0.9903	0.9821	0.2008

1305 Measured band depths for the spectra in Figure 24. Note the band depth ratio of the 1.04 / 2.0  $\mu\text{m}$   
1306 band. Only a multi-layer surface can create observed band depth ratios that are high while not  
1307 saturating the 1.5 and 2- $\mu\text{m}$  band depths. This effect is observed on icy surfaces in the Saturn and  
1308 Jupiter systems and is indicative of increasing grain size with depth.

1309

1310

## 1311 Abundance Examples

1312

1313 EMIT data over Morocco were analyzed with the first four abundance models. This area has been  
1314 studied by the FRAGMENT project (González-Romero et al., 2023). An EMIT subscene was extracted  
1315 from EMIT scene emit20230206t101334\_o03707\_s000\_l2a\_rfl\_b0106\_v01 and mapped with  
1316 Tetracorder (Figures 26 and 27). The EMIT 10 minerals include 17 categories to cover mineralogy  
1317 and grain size ranges. There is one category each for calcite, chlorite, dolomite, illite+muscovite,  
1318 kaolinite, montmorillonite and vermiculite (7 categories, each one grain size). There are 4 categories  
1319 for goethite (nano, fine, medium and coarse grained), 2 for gypsum (fine and coarse grained), and 4 for  
1320 hematite (nano, fine, medium, and coarse grained). For the results in Figures 28-31, n=5 and the  
1321 quartz-feldspar grain diameter was set to 100 microns.

1322

1323 Results for determining hematite abundance in the Morocco scene for the 4 models are shown in Figure  
1324 28. Models 1 and 4 show similar patterns but different magnitude abundances. In this case, model 1  
1325 shows higher abundances of hematite than model 4. Models 1 and 4 can't be compared with the mass  
1326 results from models 2 and 3 because the former are in % abundance while the later are in gm/m<sup>2</sup>.  
1327 Models 2 and 3 show the same pattern, but different abundances, with model 2 returning higher values.  
1328 The average abundances by mass for the Morocco scene are shown in Table 7. Because model 4 is  
1329 based on the masses in model 3 with additional information to derive quartz + feldspar abundance, if  
1330 model 4 agrees with field data, then model 3 should be in similar agreement. However, there are no lab  
1331 studies that we know of to date that derive what the optical layer is for a scene like the one used, nor  
1332 absolute abundances of the individual components present, so it is difficult to verify model 4 results in  
1333 more detail.

1334

1335 Models 1 to 4 show the same basic patterns because they originate from the same band depth images.  
1336 Models 1 and 4 are compared for the other EMIT 10 minerals in Figures 29a and 29b. The quartz  
1337 derivation from model 4 is shown in Figure 30.

1338

1339

1340

**Table 7:**  
**Abundance Models 2 and 3 Results for Morocco Study Area**  
**Abundance in the Optical Layer for 3 Optical Depths,**  
**Tetracorder 5.27d1**

Mineral	Model 2 gm / sq meter	Model 3 gm / sq meter
calcite	220.0	122.0
chlorite	25.62	46.80
dolomite	116.1	287.0
goethite-nano	1.92	1.01
goethite-fine	0.64	2.60
goethite-med	0.62	3.63
goethite-large	0.68	5.97
gypsum-fine	22.31	27.03
gypsum-coarse	13.33	145.3
hematite-nano	4.89	1.90
hematite-fine	0.56	2.88
hematite-med	0.56	4.04
hematite-large	0.78	7.60
illite+muscovite	34.76	23.16
kaolinite	16.38	15.38
montmorillonite	24.79	17.98
Vermiculite	0.0	0.0

1341

1342

1343 The FRAGMENT study of the Morocco field site has characterized the mineralogy and grain size  
 1344 information (González-Romero et al., 2023). The abundances for model 4 are compared to the average  
 1345 field data in Table 8. Examination of the 10 EMIT minerals shown in Figures 28, 29a, 29b show large  
 1346 variations in local mineral abundances. While the average abundances in Table 8 are mostly consistent.

1347

1348 The iron oxide Field Sample results in Table 8 are from X-Ray Diffraction, XRD. XRD is not very  
 1349 sensitive with sub-micron iron oxide grains, which are the dominant grain sizes in the Morocco scene  
 1350 according to spectroscopy. The Table 8 XRD derived iron oxide abundances from field samples are  
 1351 lower than the Model 4 derived abundances. Therefore, we compared wet chemistry from González-  
 1352 Romero et al., (2023) derived iron oxide abundances to Model 4 derived abundances and plot the  
 1353 results in Figure 31 with good agreement.

1354

1355 A more in-depth comparison with field-derived abundances is needed and will be conducted when the  
 1356 Morocco data become available for individual sites located in the EMIT scene.

1357

1358

**Table 8: Model 4 Abundances Compared to Field Data**

Mineral	Model 4 Fractional Abundance			González-Romero et al. (2023) Field Sample	
	max	mean	standard deviation	mean	std dev
calcite	0.554	0.100	0.176	0.138	0.082
dolomite	0.000	0.000	-	0.025	0.016
chlorite	0.664	0.0002	0.009	0.008	0.006
gypsum-fine	0.000	0.000	0.000	0.001	0.003
gypsum-coarse	0.654	0.000	0.002		
goethite-nano	0.000	0.000	0.000		
<b>goethite-fine</b>	<b>0.228</b>	<b>0.008</b>	<b>0.012</b>	<b>0.004</b>	<b>0.003</b>
goethite-med	0.372	0.000	0.002		
goethite-large	0.000	0.000	0.000		
<b>hematite-nano</b>	<b>0.020</b>	<b>0.015</b>	<b>0.004</b>		
hematite-fine	0.016	0.000	0.000	<b>0.004</b>	<b>0.004</b>
hematite-med	0.000	0.000	0.000		
hematite-large	0.000	0.000	0.000		
illite+muscovite	0.286	0.091	0.056	0.067	0.045
kaolinite	0.143	0.0004	0.007	0.047	0.043
montmorillonite	0.107	0.013	0.023	0.001	0.002
quartz+feldspar	0.980	0.772	0.147	0.69	0.15
vermiculite	0.0000	0.0000	0.0000	-	-

1360 The Model 4 results are for the area in the white box in Figure 26 using Tetracorder 5.27d1. The Model  
 1361 4 standard deviations represent the scene variability, not the error in the abundance of a pixel. Field  
 1362 results are averages for X-Ray Diffraction analyses from the entire field study area as reported in  
 1363 González-Romero et al. (2023), their Table 2 for crust, paved sediment and dune samples, and includes  
 1364 areas not imaged by EMIT in the Figures 26 and 27 boxed area. The field and EMIT results are in  
 1365 approximate agreement, usually within the standard deviations of the measurements and models, except  
 1366 the field goethite and hematite values are lower, as expected from XRD results of fine particles.  
 1367 The maximum values found by model 4 are from a few small locations and indicate a local spot may  
 1368 have large variability from the mean.

1369

1370

1371

1372

1373

1374 **Known issues**

1375

1376 A known issues file is maintained with each tetracorder.cmds github directory containing the expert  
1377 system. The file is called “AAAAA.KNOWN-ISSUES.txt” and should be reviewed before interpreting  
1378 any results from the Tetracorder system.

1379

1380 The Tetracorder expert system has been developed for researcher’s projects and field study sites. As  
1381 the diversity of sites has grown over the decades, new geologic environments have shown weaknesses  
1382 in the spectral libraries and/or the expert system. Thus, any results from the Tetracorder expert system  
1383 still need to be checked for accuracy. The calibration to reflectance of the input spectra also needs to  
1384 be checked. Calibration errors can impact identification accuracy. With EMIT now collecting imaging  
1385 spectroscopy data over the Earth, the diversity of environments that may be studied with Tetracorder or  
1386 other systems has never been greater. Thus, diligence is needed to confirm results and deficiencies, and  
1387 if known additions or fixes to the expert system and spectral libraries are identified, they should be  
1388 reported to the authors. Deficiencies can then be added to the known issues file, and noted when  
1389 improvements have been implemented.

1390

1391 While analyzing the EMIT data for this manuscript, we encountered two anomalies that illustrate why  
1392 checking results are important. Initial testing of the Morocco scene was made with Tetracorder expert  
1393 system 5.27c1, and a large amount of gypsum and jarosite was “mapped” that did not agree with the  
1394 analyses of the field samples. The expert system’s 0.35 to 2.5- $\mu\text{m}$  spectral range was developed mainly  
1395 with AVIRIS data and the system used a combination of radiative transfer models plus known spectral  
1396 reflectance areas to correct errors in the radiative transfer model (Clark et al., 2003c). That calibration  
1397 method was known not to work on a global scale, so the EMIT data had some additional channels  
1398 deleted around the 1.4- and 1.9- $\mu\text{m}$  atmospheric water bands for the Tetracorder analysis. The resulting  
1399 loss of diagnostic mineral absorptions in the EMIT data near the atmospheric water bands resulted in  
1400 gypsum being misidentified as present. A mitigation strategy was implemented in 5.27d1 and tested  
1401 on multiple AVIRIS and EMIT scenes.

1402

1403 The areas of misidentification of jarosite in the Morocco EMIT data was found to be a nano-hematite  
1404 plus fine-grained goethite mixture. Tetracorder 5.27c1 and earlier expert systems had no nano-hematite  
1405 + goethite reference spectra, leading to the misidentification. A mixture spectrum was added to expert  
1406 system 5.27d1. While this new reference spectrum reduced the misidentification, as we see in Figure  
1407 26, jarosite still shows over significant area, some of which may be other grain sizes of hematite-  
1408 goethite mixtures. More goethite-hematite mixtures of specific grain sizes and proportions are needed  
1409 to solve this problem.

1410

1411

1412 **Discussion and conclusions**

1413

1414 Tetracorder is an open-source operational system with proven results for a wide variety of applications,  
1415 including geologic mapping on the Earth and other planets and moons, mapping of ecosystems on the  
1416 Earth and conducting environmental assessments. The breath of environments where Tetracorder has  
1417 been applied on the Earth and throughout the Solar System has contributed greatly to the development  
1418 of the expert system and helped to make it widely applicable to diverse environments. However, it is

1419 still an evolving system with improvements to be made as Tetracorder is applied to new areas with  
1420 different geology and ecosystem environments than previously studied.

1421  
1422 While experience and testing in multiple environments has helped develop the Tetracorder system and  
1423 proven it is robust in those environments, we have not tested all possible environments. A new  
1424 environment may show deficiencies in either needed reference spectra, or the strategy to identify a  
1425 specific chemistry, for example, due to different instrument characteristics (spectral range, spectral  
1426 resolution, signal-to-noise ratio). Thus, there remains a need to check results for consistency and  
1427 accuracy. Users are requested to report known deficiencies to the authors so that the deficiency may be  
1428 repaired or mitigated.

1429  
1430 The abundance models all need refinement. While the equations used for the abundance models are  
1431 well established, one of the main issues is accuracy of the input optical constants. Available optical  
1432 constants need to be reviewed and where differences are found in the literature, new measurements  
1433 need to be made. As grain size gets small, into the tens of nanometers and smaller, the surface-to-  
1434 volume ratio of each particle is increasing, and chemical bonds at and near the surface have different  
1435 bonding, e.g., electric fields are different. Thus, optical constants are expected to change with particle  
1436 size in the sub-micron range. Optical constants are needed as a function of grain size for micron and  
1437 sub-micron particles.

1438  
1439 Model 4 has a free parameter, the value of n, which is the number of other mineral grains per large  
1440 quartz+feldspar grain. The value of n needs to be studied empirically, by a model, or ideally, both.

## 1441 1442 **Acknowledgments**

1443  
1444  
1445 EMIT work was supported by the National Aeronautics and Space Administration Earth Venture  
1446 Instrument program, under the Earth Science Division of the Science Mission Directorate. A portion of  
1447 this research was performed at the Jet Propulsion Laboratory, California Institute of Technology, under  
1448 a contract with the National Aeronautics and Space Administration. We acknowledge the support and  
1449 assistance of NASA's International Space Station Program.

1450  
1451 Portions of this work was supported by the National Aeronautics and Space Administration through the  
1452 Solar System Exploration Research Virtual Institute 2016 (SSERVI16) Cooperative Agreement  
1453 (NNH16ZDA001N) (TREX). A portion of this work was supported by the European Research Council  
1454 (ERC) Consolidator Grant FRAGMENT (grant agreement No. 773051). Carlos Pérez García-Pando  
1455 also acknowledges support from the AXA Chair on Sand and Dust Storms at the Barcelona  
1456 Supercomputing Center funded by the AXA Research Fund.

## 1460 Appendix A

1461

## 1462 Table A1. Hematite Reference spectra and abundance parameters.

1463

1464 Nano Hematite (grain size= 50 nanometers):

1465 #  
 1466 # file  
 1467 group.1um/fe3+\_hematite.nano.BR34b2.depth.gz

DN	BD	Band	
scale factor	depth	title	
0.5	0.01	0.2727	Nanohematite BR93-34B2

convolved  
reference spectrum  
splib06 3468

1468 Fine grained Hematite (grain size =1 micron):

1469 #  
 1470 # file  
 1471 group.1um/fe3+\_hematite.fine.gr.fe2602.depth.gz  
 1472 group.1um/fe3+\_hematite.fine.gr.ws161.depth.gz  
 1473 group.1um/fe3+\_hematite.fine.gr.gds76.depth.gz  
 1474 group.1um/fe2+fe3+mix\_with\_hematite\_br5b.depth.gz  
 1475 group.1um/fe2+fe3+\_hematite\_weathering.depth.gz  
 1476 group.1um/fe3+\_hematite.thincoat.depth.gz

DN	BD	Band	
scale factor	depth	title	
0.5	1.0	0.3957	Hematite FE2602
0.5	0.79	0.4596	Hematite WS161
0.5	0.020	0.2876	Hematite.02+Quartz.98 GDS76 W
0.5	0.17	0.1597	Magnetite_skarn BR93-5B
0.5	0.01	0.1239	Basalt_weathered BR93-43
0.5	0.05	0.5045	Hematite_Thin_Film GDS27

convolved  
reference spectrum  
splib06 2100  
splib06 2208  
splib06 5790  
splib06 5934  
splib06 5460  
splib06 6198

1477 Medium grained Hematite (grain size =2 microns):

1478 #  
 1479 # file  
 1480 group.1um/fe3+\_hematite.med.gr.gds27.depth.gz  
 1481 group.1um/fe3+\_hematite.med.gr.br25b.depth.gz

DN	BD	Band	
scale factor	depth	title	
0.5	1.00	0.5700	Hematite GDS27
0.5	0.050	0.4408	Hematite_Coatd_Qtz BR93-25B

convolved  
reference spectrum  
splib06 2106  
splib06 6174

1482 Large grained Hematite (grain size =5 microns):

1483 #  
 1484 # file  
 1485 group.1um/fe3+\_hematite.lg.gr.br25a.depth.gz  
 1486 group.1um/fe3+\_hematite.lg.gr.br25c.depth.gz  
 1487 group.1um/fe3+\_hematite.lg.gr.br34c.depth.gz  
 1488 group.1um/fe3+\_maghemite.depth.gz

DN	BD	Band	
scale factor	depth	title	
0.5	0.01	0.4556	Hematite_Coatd_Qtz BR93-25A
0.5	0.69	0.5660	Hematite_Coatd_Qtz BR93-25C
0.5	0.63	0.5146	Hematite_Coatd_Qtz BR93-34C
0.5	0.85	0.7649	Maghemite GDS81 Syn (M-3)

convolved  
reference spectrum  
splib06 6186  
splib06 6192  
splib06 6180  
splib06 2928

1492

1493

## 1494 Table A2. Delta-Absorption Coefficients and Parameters for Models 2-4

	Mineral	Del K absorption coefficient cm-1	Density grams / cc	Reflectance Wavelength (μm)	Grain Diameter (μm)
1500	calcite	10.51	2.71	2.18	9
1501	chlorite	76.96	2.8	2.14	11
1502	dolomite	10.51	2.84	2.17	90
1503					
1504	goethite-fine	5120	3.8	0.76	1
1505	goethite-med	5120	3.8	0.76	2
1506	goethite-large	5120	3.8	0.76	5
1507					
1508	gypsum	50	2.36	2.09	75
1509					
1510	hematite-nano	1304	5.3	0.75	0.05
1511	hematite-fine	6400	5.3	0.75	1
1512	hematite-med	6400	5.3	0.75	2
1513	hematite-large	6400	5.3	0.75	5
1514					
1515	illite+muscovite	91.2	2.78	2.14	2
1516	kaolinite	181.0	2.6	2.11	2
1517					
1518	montmorillonite	100	2.35	2.12	2
1519	vermiculite	100	2.5	2.15	10
1520					

1521 Values are subject to refinement as new information is obtained.

1522  
1523  
1524  
1525





1683	gypsum-coarse	0.0000	0.0000	0.0000	0.0000	0.
1684	gypsum-fine	0.0000	0.0000	0.0000	0.0000	0.020 Halite = 0.16
1685	hematite-fine	0.0000	0.0000	0.0000	0.0000	0.
1686	hematite-large	0.0000	0.0000	0.0000	0.0000	0.
1687	hematite-med	0.0000	0.0000	0.0000	0.0000	0.
1688	hematite-nano	0.0151	0.0165	0.0158	0.0007	0.000 Total Fe = 0.028
1689	illite+muscovite	0.1134	0.1351	0.1244	0.0094	0.054
1690	kaolinite	0.0000	0.0000	0.0000	0.0000	0.033
1691	montmorillonite	0.0000	0.0000	0.0000	0.0000	0.000
1692	quartz-feldspar	0.8254	0.8701	0.8461	0.0216	0.636 q+f = 0.55 + 0.047 + 0.039
1693	(halite+quartz+feldspar	0.8254	0.8701	0.8461	0.0216	0.796 h+q+f = 0.16 + .55 + 0.047 + 0.039)
1694	vermiculite	0.0000	0.0000	0.0000	0.0000	0.

1695 Comment: The high illite/muscovite absorptions masks calcite/dolomite detection.

1696 Comment: Salt grains are transparent like quartz or feldspar so will have s similar  
1697 scattering contribution as quartz or feldspar. This combination  
1698 is included for comparison.

1701

1702

1703 Site # 110: pixels 326 194 328 196

1705	Mineral	min	max	mean	std_dev	FRAGMENT field mineralogy
1706	calcite	0.0000	0.4132	0.0912	0.1810	0.056
1707	chlorite	0.0000	0.0000	0.0000	0.0000	0.005
1708	dolomite	0.0000	0.0000	0.0000	0.0000	0.018
1709	goethite-fine	0.0000	0.0250	0.0169	0.0106	0.001
1710	goethite-large	0.0000	0.0000	0.0000	0.0000	0.
1711	goethite-med	0.0000	0.0000	0.0000	0.0000	0.
1712	goethite-nano	0.0000	0.0000	0.0000	0.0000	0.
1713	gypsum-coarse	0.0000	0.0000	0.0000	0.0000	0.
1714	gypsum-fine	0.0000	0.0000	0.0000	0.0000	0.008 Halite: 0.46
1715	hematite-fine	0.0000	0.0000	0.0000	0.0000	0.
1716	hematite-large	0.0000	0.0000	0.0000	0.0000	0.
1717	hematite-med	0.0000	0.0000	0.0000	0.0000	0.
1718	hematite-nano	0.0086	0.0166	0.0141	0.0032	0.002
1719	illite+muscovite	0.0000	0.1319	0.0964	0.0552	0.017
1720	kaolinite	0.0000	0.0000	0.0000	0.0000	0.011
1721	montmorillonite	0.0000	0.0548	0.0121	0.0240	0.002
1722	quartz-feldspar	0.5096	0.8726	0.7693	0.1466	0.417 q+f = 0.293 + 0.066 + 0.058
1723	(halite+quartz+feldspar	0.5096	0.8726	0.7693	0.1466	0.877 h+q+f = 0.46 + 0.293 + 0.066 + 0.058)
1724	vermiculite	0.0000	0.0000	0.0000	0.0000	0.
1725						

1726 Comment: Here is a case where the calcite absorption was strong enough to be  
1727 detected in the presence of illite/muscovite.

1728 Comment: Salt grains are transparent like quartz or feldspar so will have s similar  
1729 scattering contribution as quartz or feldspar. This combination  
1730 is included for comparison.

1731

1732

1733

1734

1735

- 1736 **References**
- 1737
- 1738 Brodrick, P.G. et al., 2023, Surface Reflectance and Atmospheric Modeling with Optimal Estimation at  
1739 the Global Scale, In Prep.
- 1740
- 1741 Candela, A., Thompson, D., Noe Dobrea, E., and Wettergreen, D. 2017, Planetary robotic exploration  
1742 driven by science hypotheses for geologic mapping. *IEEE/RSJ International Conference on Intelligent*  
1743 *Robots and Systems (IROS)*, Vancouver, BC, Canada, 3811-3818, doi: 10.1109/IROS.2017.8206231.
- 1744
- 1745 Candela, A., Kodgule, S., Edelson, K., Vijayarangan, S., Thompson, D. R., Noe Dobrea, E., and  
1746 Wettergreen, D. 2020, Planetary Rover Exploration Combining Remote and In Situ Measurements for  
1747 Active Spectroscopic Mapping. *IEEE International Conference on Robotics and Automation (ICRA)*,  
1748 Paris, France, 5986-5993, doi: 10.1109/ICRA40945.2020.9196973.
- 1749
- 1750 Carlson, R, Smythe, W., Baines, K., Barbinas, E., Burns, R., Calcutt, S., Calvin, W., Clark, R.,  
1751 Danielson, G., Davies, A., Drossart, P., Encrenaz, T., Fanale, F., Granahan, J., Hansen, G., Herrera, P.,  
1752 Hibbitts, C., Hui, J., Irwin, P., Johnson, T., Kamp, L., Kieffer, H., Leader, F., Lopes-Gautier, R.,  
1753 Matson, D., McCord, T., Mehlman, R., Ocampo, A., Orton, G., Roos-Serote, M., Segura, M., Shirley,  
1754 J., Soderblom, L., Stevenson, A., Taylor, F., Weir, A. & Weissman P. 1996, Near-Infrared Spectroscopy  
1755 and Spectral Mapping of Jupiter and the Galilean Satellites: First Results from Galileo's Initial Orbit.  
1756 *Sci*, **274**, 385-388.
- 1757 Clark, R. N., 1980, A large scale interactive one dimensional array processing system: *Publications of*  
1758 *the Astronomical Society of the Pacific*, **92**, p. 221-224.
- 1759
- 1760 Clark, R.N., 1993, SPECtrum Processing Routines User's Manual Version 3 (program SPECPR), U.S.  
1761 *Geological Survey, Open File Report 93-595*, 210 pages.
- 1762
- 1763 Clark, R. N., Vance, S., Livo, K.E. and Green, R. 1998, Mineral Mapping with Imaging Spectroscopy:  
1764 the Ray Mine, AZ. *Summaries of the 7th Annual JPL Airborne Earth Science Workshop*, R.O. Green,  
1765 Ed., JPL Publication 97-21. pp 67-76, Jan 12-14.
- 1766
- 1767 Clark, R.N.. 1999, Chapter 1: Spectroscopy of Rocks and Minerals and Principles of Spectroscopy,  
1768 *Manual of Remote Sensing*, (A.N. Rencz, ed.) John Wiley and Sons, New York, 3-58.
- 1769
- 1770 Clark, R. N., Green, R. O., Swayze, G. A., Meeker, G., Sutley, S., Hoefen, T. M., Livo, K. E., Plumlee,  
1771 G., Pavri, B., Sarture, C., Wilson, S., Hageman, P., Lamothe, P., Vance, J. S., Boardman J., Brownfield,  
1772 I., Gent, C., Morath, L. C., Taggart, J., Theodorakos, P. M. & Adams, M. 2001, Environmental Studies  
1773 of the World Trade Center area after the September 11, 2001 attack. U. S. Geological Survey, Open File  
1774 Report OFR-01-0429, 260 pp. <http://pubs.usgs.gov/of/2001/ofr-01-0429/>
- 1775
- 1776 Clark, R. N., Swayze, G. A., Livo, K. E., Kokaly, R. F., Sutley, S. J., Dalton, J. B., McDougal, R. R., &  
1777 Gent, C. A. 2003a, Imaging spectroscopy: Earth and planetary remote sensing with the USGS  
1778 Tetracorder and expert systems, *JGR*, **108**(E12), 5131, doi:10.1029/2002JE001847, p. 5-1.
- 1779

- 1780 Clark, R.N., Hoefen, T.M., Swayze, G.A., Livo, K.E., Meeker, G.P., Sutley, S.J., Wilson, S.,  
1781 Brownfield, I.K., and Vance, J.S. 2003b, Reflectance Spectroscopy as a Rapid Assessment Tool for the  
1782 Detection of Amphiboles from the Libby, Montana Region, *U.S. Geological Survey Open-File Report*  
1783 03-128. <http://pubs.usgs.gov/of/2003/ofr-03-128/ofr-03-128.html>
- 1784
- 1785 Clark, R., Swayze, G. , Livo, E., Kokaly, R., King, T.V.V., Dalton, B., Vance, S., Rockwell, B., Hoefen,  
1786 T., McDougal, R., 2003c, Surface reflectance calibration of terrestrial imaging spectroscopy data: A  
1787 tutorial using AVIRIS: Proceedings of the 11<sup>th</sup> JPL Airborne Earth Science Workshop, R.O. Green  
1788 (ed.), JPL Publication 03-4, p. 43-63.  
1789 [https://popo.jpl.nasa.gov/pub/docs/workshops/02\\_docs/2002\\_Clark\\_web.pdf](https://popo.jpl.nasa.gov/pub/docs/workshops/02_docs/2002_Clark_web.pdf)
- 1790
- 1791 Clark, R. N., Swayze, G. A., Hoefen, T. M., Green, R. O., Livo, K. E., Meeker, G., Sutley, S., Plumlee,  
1792 G., Pavri, B., Sarture, C., Boardman, J., Brownfield, I. & Morath, L. C. 2006, Chapter 4:  
1793 Environmental mapping of the World Trade Center area with imaging spectroscopy after the September  
1794 11, 2001 attack: in *Urban Aerosols and Their Impacts: Lessons Learned from the World Trade Center*  
1795 *Tragedy*, Jeff Gaffney and N. A. Marley (eds), American Chemical Society, Symposium Series 919,  
1796 Oxford University Press, p. 66-83, plates 4.1-4.6.
- 1797
- 1798 Clark, R. N., Swayze, G. A., Wise, R., Livo, E., Hoefen, T., Kokaly, R., Sutley, S. J. 2007, USGS  
1799 digital spectral library splib06a: U.S. Geological Survey, Data Series 231. Data at  
1800 <https://github.com/PSI-edu/spectroscopy-tetracorder/tree/main/sl1/usgs>
- 1801
- 1802 Clark, R. N. 2009, Detection of Adsorbed Water and Hydroxyl on the Moon, *Science*, **326**, 562-564,  
1803 DOI: 10.1126/science.1178105.
- 1804
- 1805 Clark, R. N., Curchin, J. M., Barnes, J. W., Jaumann, R., Soderblom, L., Cruikshank, D. P., Brown, R.  
1806 H., Rodriguez, S., Lunine, J., Stephan, K., Hoefen, T. M., Le Mouelic, S., Sotin, C., Baines, K. H.,  
1807 Buratti, B. & Nicholson, P. 2010a, Detection and Mapping of Hydrocarbon Deposits on Titan, *JGR*,  
1808 **115**, E10005, doi:10.1029/2009JE003369.
- 1809
- 1810 Clark, R. N., Swayze, G. A., Leifer, I., Livo, K. E., Lundein, S., Eastwood, M., Green, R. O., Kokaly,  
1811 R., Hoefen, T., Sarture, C., McCubbin, I., Roberts, D., Steele, D., Ryan, T., Dominguez, R., Pearson,  
1812 N., and the Airborne Visible/Infrared Imaging Spectrometer (AVIRIS) Team, 2010b, A method for  
1813 qualitative mapping of thick oil spills using imaging spectroscopy: U.S. Geological Survey Open-File  
1814 Report 2010-1101. <http://pubs.usgs.gov/of/2010/1101/>
- 1815
- 1816 Clark, R. N., Cruikshank, D. P., Jaumann, R., Brown, R. H., Stephan, K., Dalle Ore, C. M., Livo, K. E.,  
1817 Pearson, N., Curchin, J. M., Hoefen, T. M., Buratti, B. J., Filacchione, G., Baines, K. H. & Nicholson,  
1818 P. D. 2012, The Composition of Iapetus: Mapping Results from Cassini VIMS, *Icar*, **218**, 831-860.
- 1819
- 1820 Clark, R. N., Swayze, G. A., Murchie, S. L., Seelos, F. P., Seelos, K., & Viviano-Beck, C. E. (2015)  
1821 Mineral and other materials mapping of CRISM data with Tetracorder 5. 46th LPSC Abstract #2410.  
1822

- 1823 Clark, R. N., Swayze, G. A., Murchie, S. L., Seelos, F. P., Viviano-Beck, C. E., & Bishop, J. (2016)  
1824 Mapping water and water-bearing minerals on Mars with CRISM. 47th LPSC Abstract #2900.
- 1825
- 1826 Clark, R. N., M. E. Banks, A. Hendrix, M. D. Lane, T. H. Prettyman, F. Vilas, S. Wright, D. Vaniman,  
1827 C. Thieberger, C. Ahrens, S. Buxner, 2022, Science Team Experience with an Autonomous Rover in the  
1828 Field and Automated Science Analyses, 53rd Lunar and Planetary Science Conference, Abstract 2323.
- 1829
- 1830 Clark, R. N., Prettyman, T. H., Banks, M. E., Hendrix, A. R., Noe Dobrea, E., Lane, M. D., Vilas, F.,  
1831 Wright, S. P., Vaniman, D., Thieberger, C., Ahrens, C., Buxner, S., Pearson, N. C., Holsclaw, G.,  
1832 Borrelli, M., Kramer, G. P., Wettermgreen, D., Vijayarangan, S., Candela, A., Breitfeld, A., Hansen, M.,  
1833 Kumari, N., Martin, A. C., Patterson, R., Meier, M., Knightly, P., Steckel, A. V. and Osterloo, M. 2023,  
1834 Science Team Experience with an Autonomous Rover and Automated Science Analyses During the  
1835 TREX 2021 and 2022 Field Campaigns, *PSJ*, this issue.
- 1836
- 1837 Ehlmann, B.L., Swayze, G.A., Milliken, R.E., Mustard, J.F., Clark, R.N., Murchie, S.L., Breit, G.N.,  
1838 Wray, J.J., Gondet, B., Poulet, F., Crater, J., Calvin, W.M., Benzel, W.M., and Seelos, K.D. 2016,  
1839 Discovery of alunite in Cross Crater, Terra Sirenum, Mars: Evidence for acidic, sulfurous waters,  
1840 *American Mineralogist*, **101**, 1527-1542. doi:10.2138/am-2016-5574.
- 1841
- 1842 Green, R. (2022). EMIT L2A Estimated Surface Reflectance and Uncertainty and Masks 60 m V001  
1843 [Data set]. NASA EOSDIS Land Processes Distributed Active Archive Center. Accessed 2023-07-16  
1844 from <https://doi.org/10.5067/EMIT/EMITL2ARFL.001>
- 1845
- 1846 González-Romero, A., González-Florez, C., Panta, A., Yus-Díez, J., Reche, C., Córdoba, P., Alastuey  
1847 A., Kandler, K., Klose, M., Baldo, C., Clark, R.N., Ehlmann, B., Greenberger, R., Keebler, A., Shi, Z.,  
1848 Querol, X., and Pérez García-Pando, C. 2023, Variability in sediment particle size, mineralogy, and Fe  
1849 mode of occurrence across dust-source inland drainage basins: The case of the Lower Drâa Valley,  
1850 Morocco, *Atmospheric Chemistry and Physics*, in press.
- 1851
- 1852 Hapke, B., 1981. Bidirectional reflectance spectroscopy 1. Theory. *JGR*. **86**, 3039–3054.
- 1853
- 1854 Hapke, B., 1993. Theory of Reflectance and Emittance Spectroscopy. Cambridge University Press,  
1855 New York.
- 1856
- 1857 Hendrix et al., 2023, The Toolbox for Research and Exploration, *PSJ*, this issue in review.
- 1858
- 1859 Hoefen T.M., Clark R.N., Bandfield J.L., Smith M.D., Pearl J.C., & Christensen P.R. (2003) Discovery  
1860 of olivine in the Nili Fossae region of Mars. *Science*, **302**, 627–630.
- 1861
- 1862 King, T.V.V., Clark, R.N., Ager, C. and Swayze, G.A. 1995, Remote mineral mapping using AVIRIS  
1863 data at Summitville, Colorado and the adjacent San Juan Mountains. *Proceedings: Summitville Forum*  
1864 '95, H.H. Posey, J.A. Pendleton, and D. Van Zyl Eds., Colorado Geological Survey Special Publication  
1865 38, p. 59-63.
- 1866
- 1867 Kokaly R. F., Despain D. G., Clark R. N., & Livo K. E. (2003) Mapping vegetation in Yellowstone  
1868 National Park using spectral feature analysis of AVIRIS data. *RSEnv*, **84**, 437–456.
- 1869

- 1870 Kokaly R., Despain D. G., Clark R., & Livo K. E. (2007) Spectral analysis of absorption features for  
1871 mapping vegetation cover and microbial communities in Yellowstone National Park using AVIRIS data.  
1872 In: Integrated geoscience studies in the Greater Yellowstone area: Volcanic, tectonic, and hydrothermal  
1873 processes in the Yellowstone geoecosystem. USGS Professional Paper 1717 (L.A. Morgan, ed.). U.S.  
1874 Geological Survey, Denver.
- 1875
- 1876 Kokaly R. F., King T. V., & Hoefen T. M. (2013) Surface mineral maps of Afghanistan derived from  
1877 HyMap imaging spectrometer data, version 2. US Department of the Interior, US Geological Survey,  
1878 Denver.
- 1879
- 1880 Kokaly, R. F., Clark, R. N., Swayze, G. A., Livo, K. E., Hoefen, T. M., Pearson, N. C., Wise, R. A.,  
1881 Benzel, W. M., Lowers, H. A., Driscoll, R. L. & Klein, A. J. 2017, USGS Spectral Library Version 7  
1882 Data: U.S. Geological Survey data release, <https://dx.doi.org/10.5066/F7RR1WDJ>
- 1883
- 1884 Kramer, G. Y., Besse, S., Dhingra, D., Nettles, J., Klima, R., Garrick-Bethell, I., Clark, R. N., Combe,  
1885 J. P., Head, J. W. III, Taylor, L. A., Pieters, C. M., Boardman, J. & McCord, T. B. 2011, The Spectral  
1886 Peculiarities of Lunar Swirls as Seen by the Moon Mineralogy Mapper, *JGR*, **116**, E00G18,  
1887 doi:[10.1029/2010JE003729](https://doi.org/10.1029/2010JE003729).
- 1888 Livo, K.E. and Clark, R.N. 2002, Mapped minerals at Questa, New Mexico, using Airborne Visible-  
1889 Infrared Imaging Spectrometer (AVIRIS) data - preliminary report for: First quarterly report of the U.S.  
1890 Geological Survey investigation of baseline and pre-mining ground-water quality in the Red River  
1891 Valley Basin, New Mexico, November 13, 2001, *U.S. Geological Survey Open-File Report 02-26*, 11p.,  
1892 3 maps. <http://pubs.usgs.gov/of/2002/ofr-02-0026>
- 1893
- 1894 Livo, K. E., Kruse, F. A., Clark, R. N., Kokaly, R. F., & Shanks, W. C. III, 2007, Hydrothermally  
1895 Altered Rock and Hot- Spring Deposits at Yellowstone National Park—Characterized Using Airborne  
1896 Visible- and Infrared-Spectroscopy Data, Chapter O in: Integrated Geoscience Studies in the Greater  
1897 Yellowstone Area—Volcanic, Tectonic, and Hydrothermal Processes in the Yellowstone Geoecosystem  
1898 USGS Professional Paper 1717, 463-489. <http://pubs.usgs.gov/pp/1717/downloads/pdf/p1717O.pdf>
- 1899
- 1900 Milliken, R. E., Swayze, G. A., Arvidson, R. E., Bishop, J. L., Clark, R. N., Ehlmann, B. L., Green, R.  
1901 O., Grotzinger, J. P., Morris, R. V., Murchie, S., Mustard, J. F., Weitz, C., & the CRISM Science Team,  
1902 2008, Opaline silica in young deposits on Mars, *Geo*, **36**, 847-850.
- 1903
- 1904 Noe Dobrea, E. Z., Ahrens, C., Banks, M.E., Breitfeld, A., Candela, A., Clark, R. N., Hansen, M.,  
1905 Hendrix, A., Holsclaw, G., Kramer, G., Lane, M. D., Prettyman, T. H., Thieberger, C., Vijayarangan, S.,  
1906 Vilas, F., Wettergreen, D., Wright, S. P. and the TREX Team, Autonomous Rover Science in the Field:  
1907 First Resutls. *53rd LPSC*, Abstract 1674.
- 1908 Noe Dobrea, E. Z., Ahrens, C., Banks, M. E., Bell, E., Breitfeld, A., Bristow, T., Candela, A., Clark, R.  
1909 N., Hansen, M., Hendrix, A., Holsclaw, G., Knightly, P., Kramer, G., Kumari, N., Lane, M. D., Martin,  
1910 A. C., Meier, M. L., Patterson, R. V., Pearson, N. C., Prettyman, T. H., Steckel, A. V., Vijayarangan, S.,

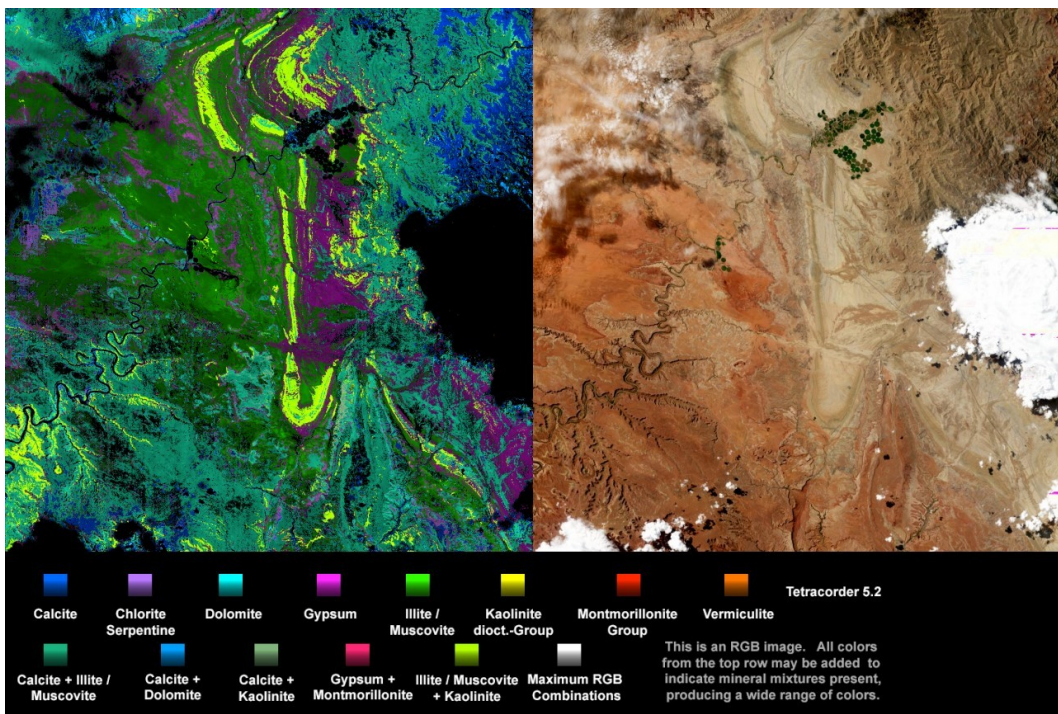
- 1911 Vilas, F., Wettergreen, D., Wright, S. P., and the TREX Team 2023a, Autonomous Rover Science in the  
1912 Field: Yellow Cat, *54th LPSC*, Abstract 2366.
- 1913 Noe Dobrea et al., (2023b) trex hypothesis paper. *PSJ*, this issue. REF  
1914
- 1915 Pieters, C. M., Goswami, J. N., Clark, R. N., Annadurai, M., Boardman, J., Buratti, B., Combe, J. P.,  
1916 Dyar, M. D., Green, R., Head, J. W., Hibbitts, C., Hicks, M., Isaacson, P., Klima, R., Kramer, G.,  
1917 Kumar, S., Livo, E., Lundein, S., Malaret, E., McCord, T., Mustard, J., Nettles, J., Petro, N., Runyon,  
1918 C., Staid, M., Sunshine, J., Taylor, L. A., Tompkins, S. & Varanasi, P. 2009a, Character and distribution  
1919 of OH/H<sub>2</sub>O on the surface of the Moon seen by M3 on Chandrayaan-1, *Sci*, **326**, 568–572,  
1920 doi:10.1126/science.1178658.  
1921
- 1922 Swayze, G.A., Smith, K. S., Clark, R. N., Sutley, S. J., Pearson, R. N., Rust, G. S., Vance, J. S.,  
1923 Hageman, P.L., Briggs, P.H., Meier, A.L., Singleton, M.J. & Roth, S. 2000, Using imaging  
1924 spectroscopy to map acidic mine waste, *EnST*, **34**. 47-54.  
1925
- 1926 Swayze, G. A., Clark, R. N., Sutley, S. J., Rockwell, B. W., Gent, C. A. & Farm, B. P., 2002, Mineral  
1927 mapping Mauna Kea and Mauna Loa shield volcanoes on Hawaii Mauna Kea using AVIRIS data and  
1928 the USGS Tetracorder Spectral Identification System: Lessons applicable to the search for relict  
1929 Martian hydrothermal systems:, Proceedings of the 11th JPL Airborne Earth Science Workshop, R.O.  
1930 Green (ed.), Jet Propulsion Laboratory Publication 03-4, p. 373-387.  
1931
- 1932 Swayze, G.A., Clark, R.N., Goetz, F.H., Chrien, T.G., and Gorelick, N.S., 2003, Effects of spectrometer  
1933 band pass, sampling, and signal-to-noise ratio on spectral identification using the Tetracorder  
1934 algorithm: *Journal of Geophysical Research (Planets)*, vol. 108(E9), 5105, doi:  
1935 10.1029/2002JE001975, 30 p.  
1936
- 1937 Swayze, G.A., Higgins, C.T., Clinkenbeard, J.P., Kokaly, R.F., Clark, R.N., Meeker, G.P. and Sutley,  
1938 S.J., 2004, Preliminary report on using imaging spectroscopy to map ultramafic rocks, serpentinites,  
1939 and tremolite-actinolite-bearing rocks in California: U.S. Geological Survey Open-File Report 2004-  
1940 1304, 20 p. <http://pubs.usgs.gov/of/2004/1304>  
1941
- 1942 Swayze, G.A., Higgins, C.T., Clinkenbeard, J.P., Kokaly, R.F., Clark, R.N., Meeker, G.P., Sutley, S.,  
1943 2004, Preliminary report on using imaging spectroscopy to map ultramafic rocks, serpentinites, and  
1944 tremolite-actinolite-bearing rocks in California: California Geological Survey Geologic Hazards  
1945 Investigation 2004-01, 20 p.  
1946 [http://www.consrv.ca.gov/cgs/geologic\\_hazards/hazardous\\_minerals/aviris.htm](http://www.consrv.ca.gov/cgs/geologic_hazards/hazardous_minerals/aviris.htm)  
1947
- 1948 Swayze, G.A., Clark, R.N., Sutley, S.J., Hoefen, T.M., Plumlee, G.S., Meeker, G.P., Brownfield, I.K.,  
1949 Livo, K.E. and Morath, L.C. 2006, Chapter 3: Spectroscopic and x-ray diffraction analyses of asbestos  
1950 in the World Trade Center dust: in *Urban Aerosols and Their Impacts: Lessons Learned from the World*  
1951 *Trade Center Tragedy*, Jeff Gaffney and N. A. Marley (eds), *American Chemical Society*, Symposium  
1952 Series 919, Oxford University Press, p. 40-65.  
1953
- 1954 Swayze, G. A., Kokaly, R. F., Higgins, C. T., Clinkenbeard, J. P., Clark, R. N., Lowers, H. A. & Sutley,  
1955 S.J., 2009, Mapping potentially asbestos-bearing rocks using imaging spectroscopy: *Geo*, **37**, 763-766.

- 1956
- 1957 Swayze, G. A., Clark, R. N., Goetz, A. F. H., Livo, K. E., Breit, G. N., Sutley, S. J., Kruse, F. A., Snee,  
1958 L. W., Lowers, H. A., Post, J. L., Stoffregen, R. E. & Ashley, R. P., 2014, Mapping advanced argillic  
1959 alteration at Cuprite, Nevada using imaging spectroscopy: *EcGeo*, **109**, 1179-1221  
1960 DOI:10.2113/econgeo.109.5.1179
- 1961
- 1962 Thompson, D. R., Natraj, V., Green, R. O., Helmlinger, M. C., Gao, B. C., Eastwood, M. L. 2018,  
1963 Optimal estimation for imaging spectrometer atmospheric correction, *Remote Sensing of Environment*,  
1964 **216**, 355-373.
- 1965 Wagner, M., Heys, S., Wettergreen, D., Teza, J., Apostolopoulos, D., Kantor, G., and Whittaker, W.  
1966 2005. Design and Control of a Passively Steered, Dual Axle Vehicle. Proceedings of *I-SAIRAS:*  
1967 *International Symposium on Artificial Intelligence, Robotics and Automation in Space*. Munich,  
1968 Germany. European Space Agency ESA-SP-603. September 2005.
- 1969
- 1970 Wettergreen, D., Cabrol, N., Baskaran, V., Calderón, F., Heys, S., Jonak, D., Luders, R. A., Pane, D.,  
1971 Smith, T., Teza, J., Tompkins, P., Villa, D., Williams, C., and Wagner, M. 2005, Second experiments in  
1972 the robotic investigation of life in the Atacama Desert of Chile. In *Proc. 8th International Symposium*  
1973 *on Artificial Intelligence, Robotics and Automation in Space*, vol. 4, p. 4.
- 1974
- 1975 Wettergreen, D., Wagner, M., Jonak, D., Baskaran, V., Deans, M., Heys, S., Pane. D., et al., 2008,  
1976 Long-Distance Autonomous Survey and Mapping in the Robotic Investigation of Life in the Atacama  
1977 Desert, Proceedings of *I-SAIRAS: International Symposium on Artificial Intelligence, Robotics and*  
1978 *Automation in Space*. Hollywood, USA. February 2008.
- 1979
- 1980 Vijayarangan, S., Kohanbash, D., Foil, G., Zacny, K., Cabrol, N., and Wettergreen, D. 2018, Field  
1981 experiments in robotic subsurface science with long duration autonomy. In *Field and Service Robotics: Results of the 11th International Conference*, 515-529. Springer International Publishing.  
1982
- 1983

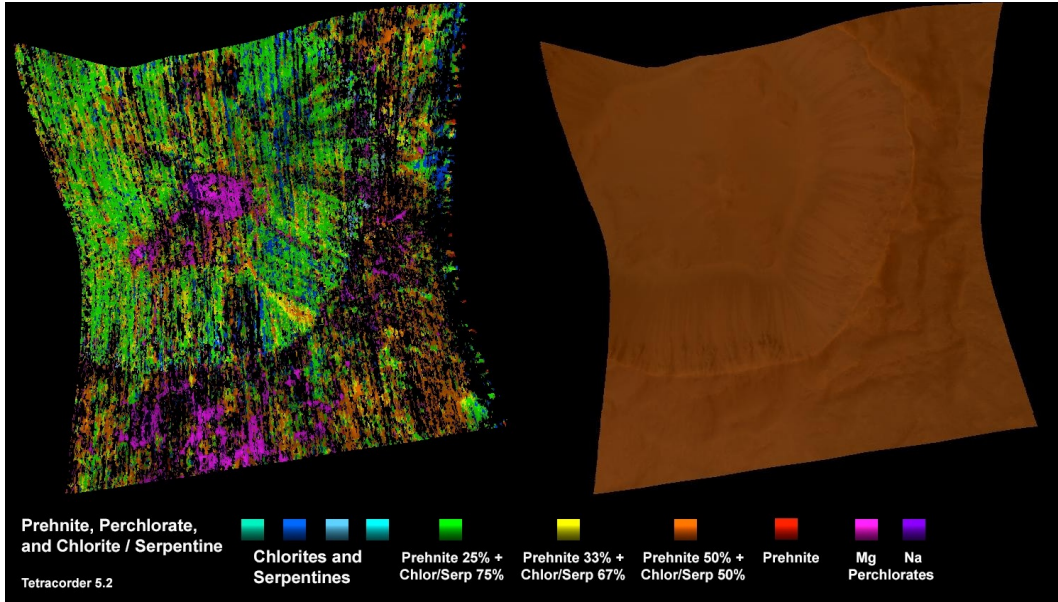
1984 **Figures**

1985

1986 a)

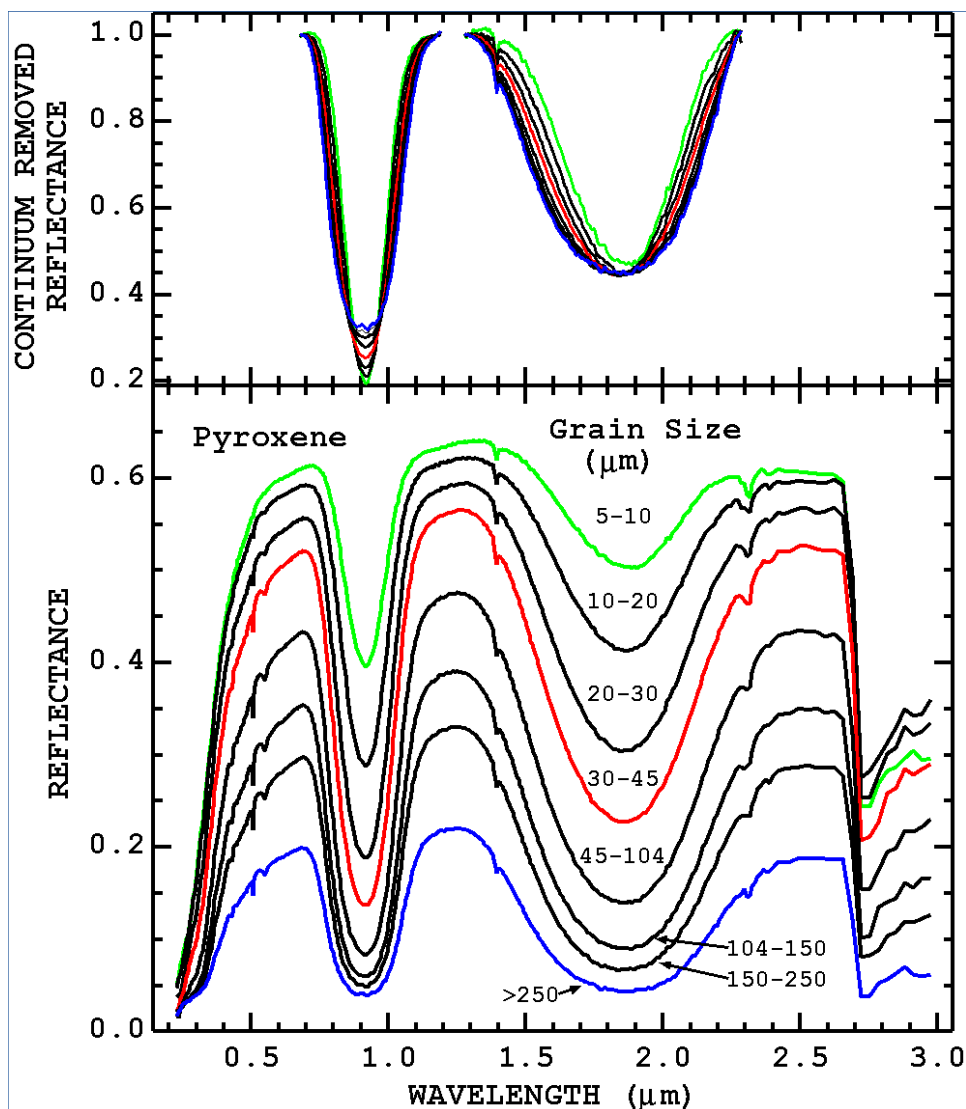


1987 b)

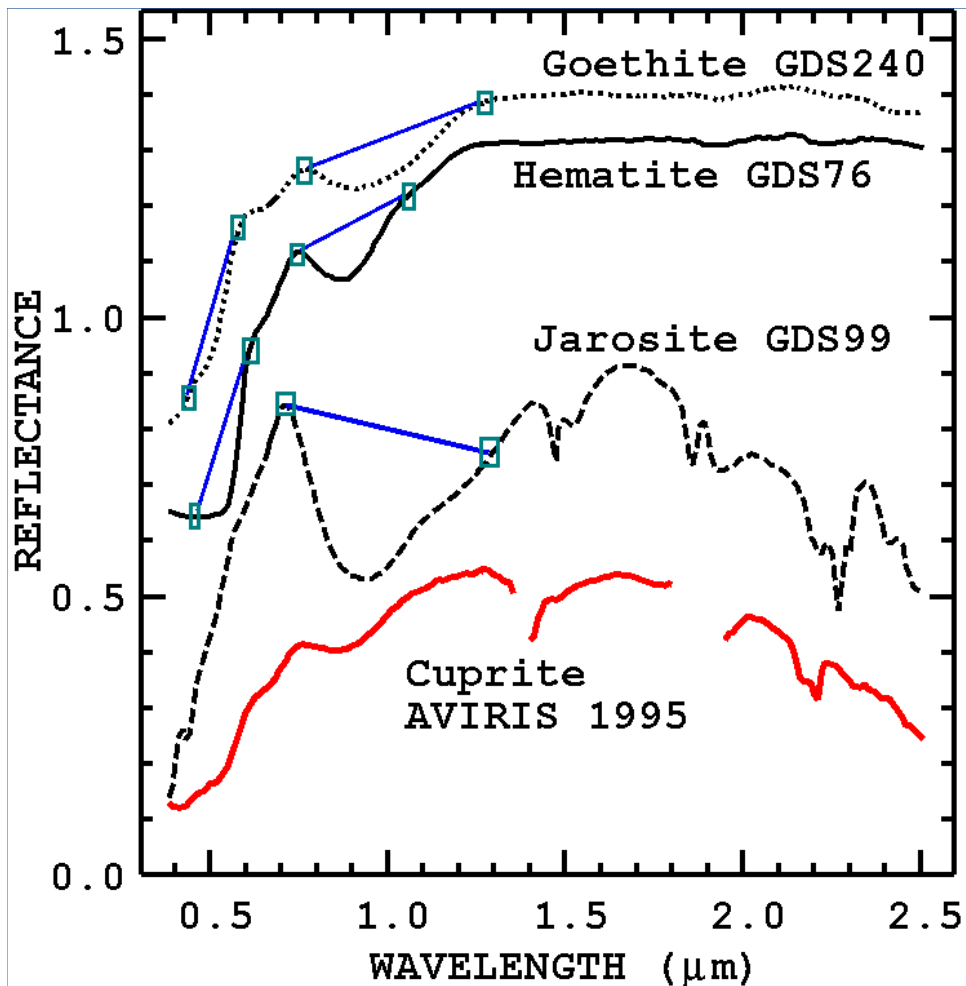


1989 **Figure 1. Tetracorder mineral map expert system standard products.**

(a) EMIT image cube of Utah, USA. Arches National Park is in the lower right corner. Results here show minerals detected using absorption features in the near-infrared region. (b) Mars Reconnaissance Orbiter, Compact Reconnaissance Imaging Spectrometer for Mars (CRISM) scene FRT000148C1\_07\_IF164J\_MTR3 for a crater at 7.7°S, 84.5°E. The Tetracorder expert system was the same for this wavelength region as the Tetracorder EMIT results in (a).

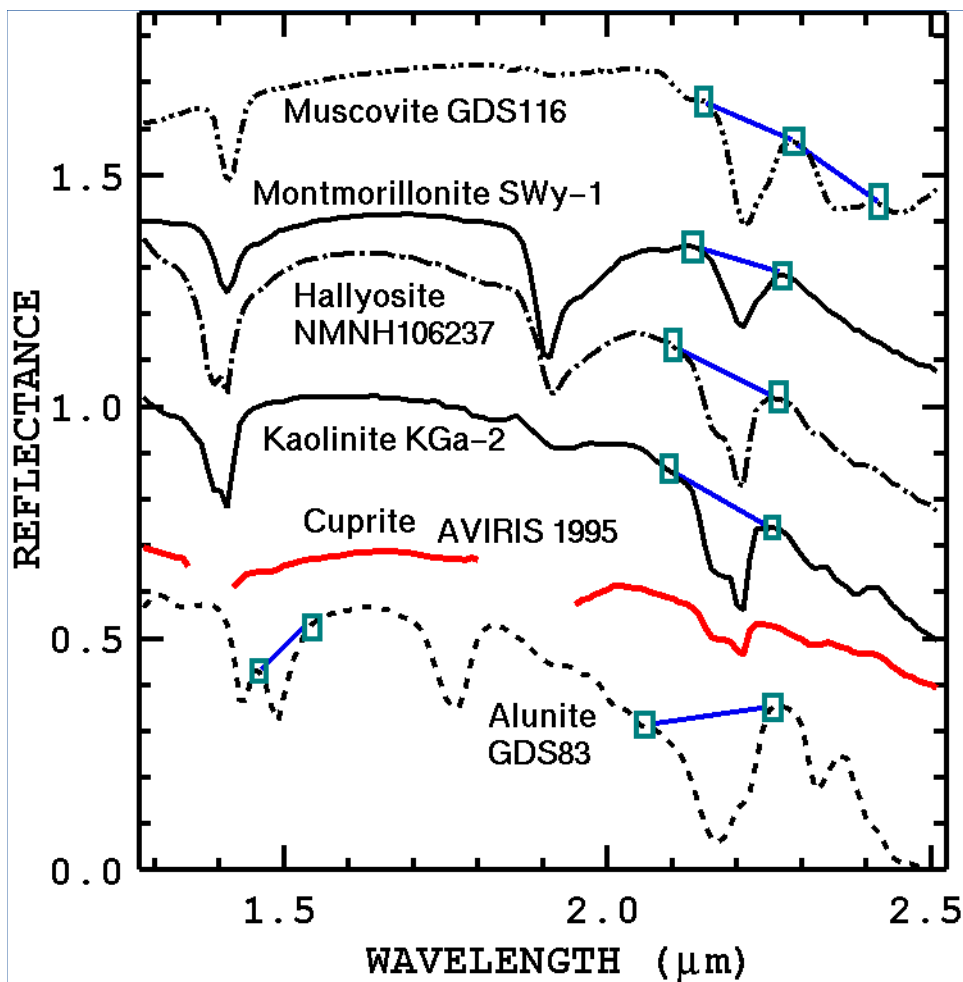


1997 Figure 2. Effects of mixtures and grain size on band shape. Pyroxene reflectance spectra as a function  
 1998 of grain size. As the grain size becomes larger, more light is absorbed, the reflectance decreases, and  
 1999 the absorption feature bottoms flatten. Note the trace tremolite contamination causing the narrow  
 2000 absorption features near 1.4 and 2.3  $\mu\text{m}$ . The broader pyroxene absorptions are the continuum  
 2001 background to the narrow tremolite features. This example shows how the components in a mixture can  
 2002 be readily identified even though no unmixing analysis is done. The component features are  
 2003 “spectrally separated” in wavelength position and width, as well as shape. Continuum-removed feature  
 2004 fits (top) show the similarity in shape of features at different grain sizes. The small change in shape  
 2005 can be used to determine grain size from the spectra, independent of abundance. Data from Clark et al.,  
 2006 2003a, USGS spectral library 06.  
 2007  
 2008

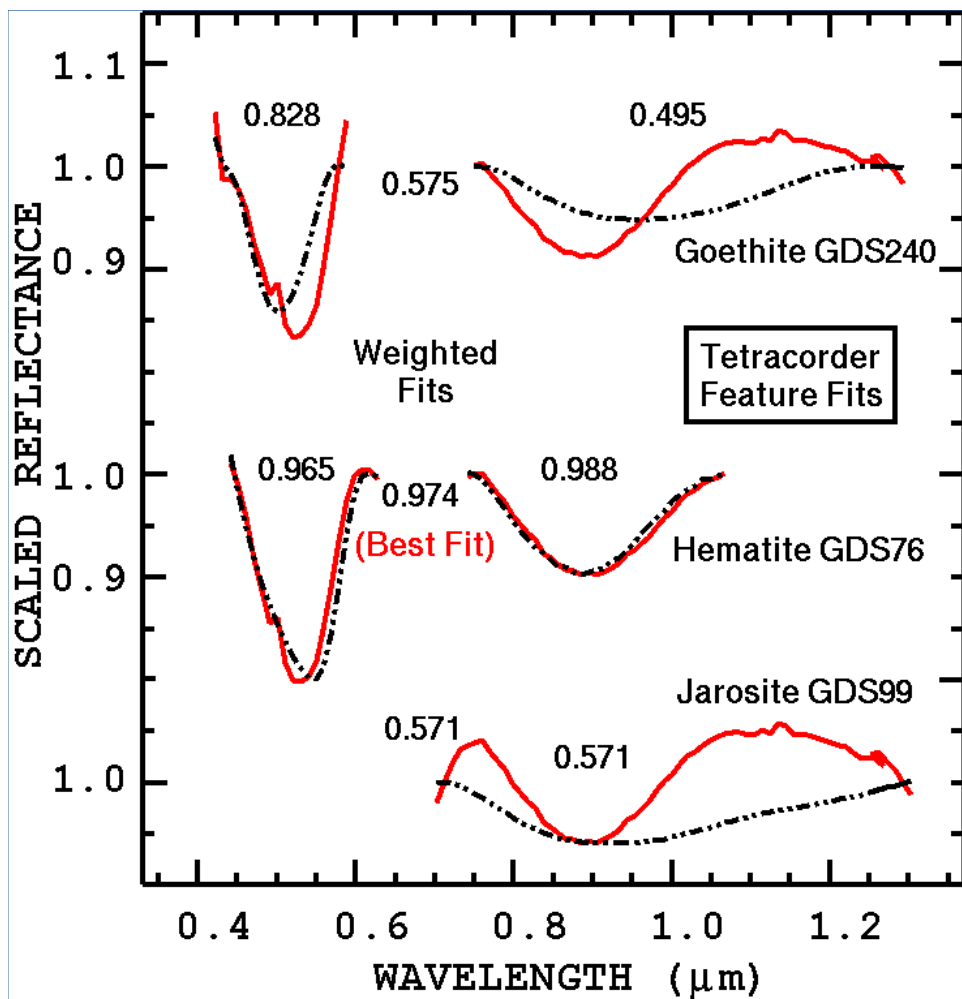


2010

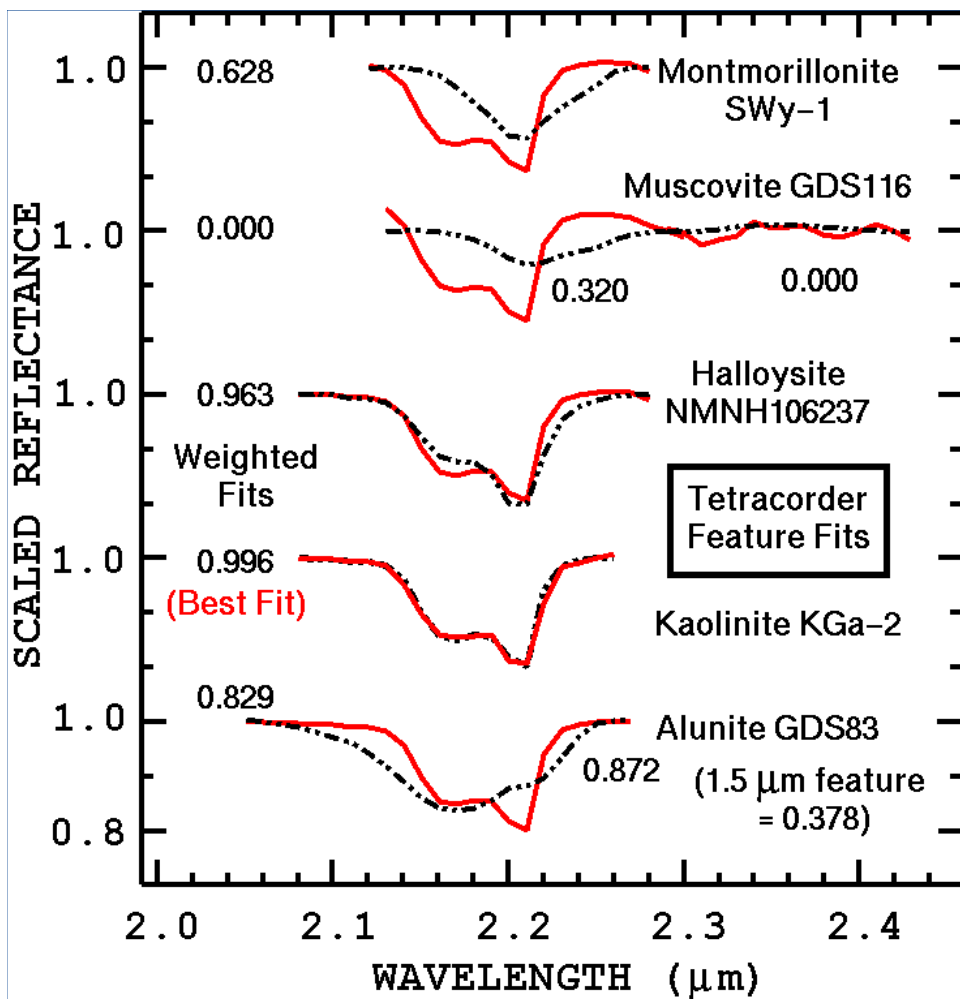
2011 Figure 3a. Continuum removal process employed by the Tetracorder spectral feature shape matching  
 2012 algorithm. Three reference spectra are shown: goethite, jarosite and hematite. Each spectral feature  
 2013 has its own continuum end-points (illustrated by the boxes). The continuum is removed from both the  
 2014 observed and reference spectra. For example, the hematite 0.9- $\mu\text{m}$  feature continuum is removed from  
 2015 the Cuprite unknown spectrum, then the goethite continuum is removed, and so on. This allows a  
 2016 specific comparison between each spectral library feature and the unknown. The spectra are offset for  
 2017 clarity. From Clark et al., 2003, a public domain image.



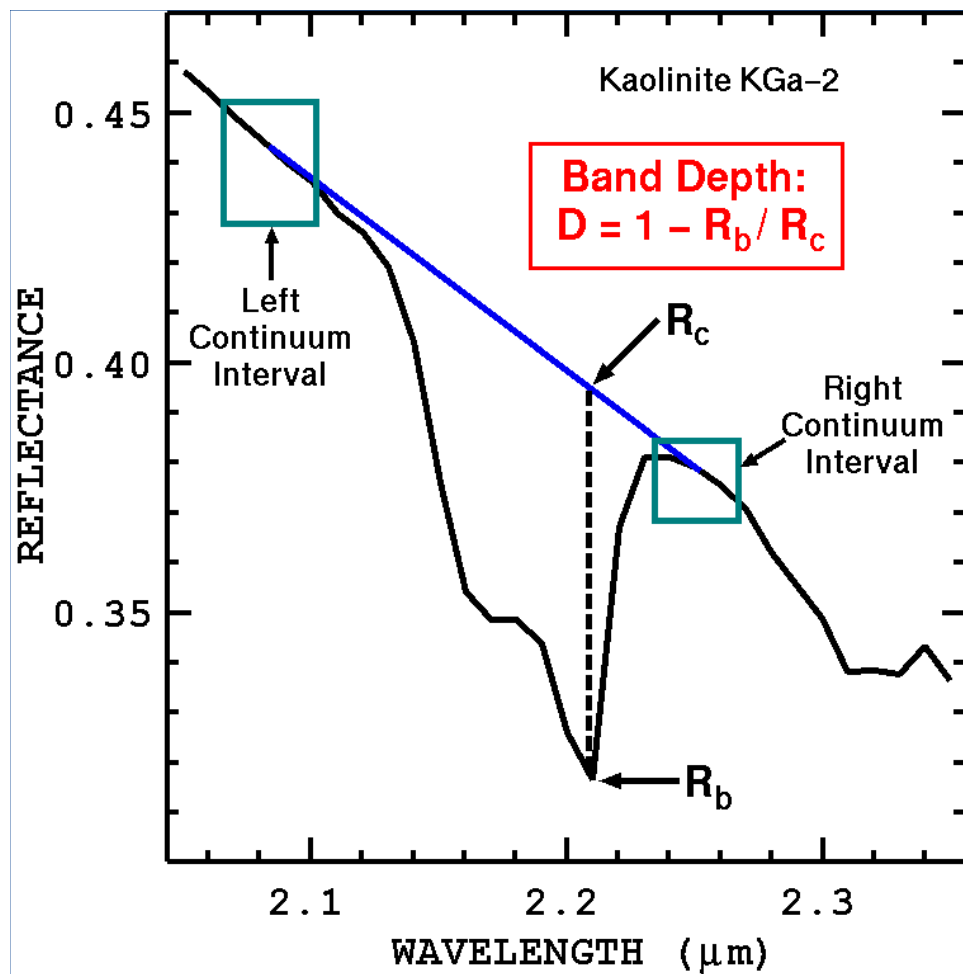
2018      Figure 3b. Spectral features as on Figure 3a except for comparison with vibrational absorptions near  
 2019      2.2  $\mu\text{m}$ . Note that alunite also has a diagnostic absorption near 1.5  $\mu\text{m}$ . The spectra are offset for  
 2020      clarity. From Clark et al., 2003, a public domain image.



2022 Figure 4a. The continuum removed spectra from Figure 3a are fit to each other using a modified least  
 2023 squares calculation. The library reference feature strength is increased or decreased to best match the  
 2024 observed feature. Tetracorder compares the least-squares fits to many features from many library  
 2025 reference spectra to determine which one matches best. The solid red line in each case is the unknown  
 2026 and the dash double dotted black line is the library reference feature. For each feature, the least squares  
 2027 correlation coefficients (the *fits*) are given, and along a vertical central column, the weighted fits are  
 2028 shown. The best match to the Cuprite spectrum is hematite. Hematite has two features used in the  
 2029 identification: the 0.9  $\mu\text{m}$  feature gives a fit of 0.988, and the 0.5  $\mu\text{m}$  feature gives a fit of 0.965. The  
 2030 area-weighted fit is 0.974. From Clark et al., 2003, a public domain image.



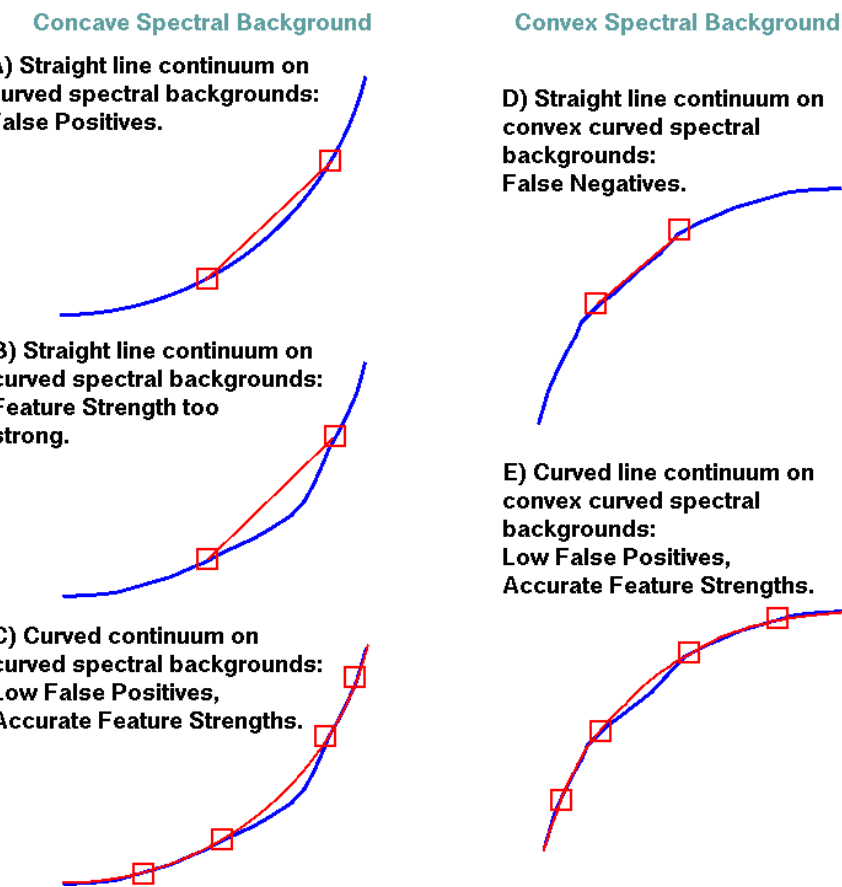
2032 Figure 4b. The continuum removed spectra from Figure 3b are fit together using a modified least  
 2033 squares calculation. Kaolinite is the best match to the Cuprite spectrum. The muscovite spectrum has  
 2034 two features, one near 2.2 and the other near 2.3  $\mu\text{m}$ . No 2.3- $\mu\text{m}$  muscovite feature could be detected  
 2035 in the Cuprite spectrum, so the weighted fit is zero (left hand column). Note the very similar fits  
 2036 between kaolinite (0.996) and halloysite (0.963), yet the halloysite profile clearly does not match as  
 2037 well as the kaolinite profile. This illustrates that small differences in fit numbers are significant.  
 2038 Alunite has two diagnostic spectral features, but the 1.5- $\mu\text{m}$  feature is not shown. From Clark et al.,  
 2039 2003, a public domain image.



2041     Figure 5. Characteristics of an absorption feature. A continuum interval is chosen on each side of the  
 2042     feature to reduce noise. The continuum intervals in this example are about 30nm wide. A straight-line  
 2043     continuum is fit between the end points. The reflectance at the band center ( $R_b$ ) and the corresponding  
 2044     continuum reflectance at the band center ( $R_c$ ) are found to compute the band depth,  $D$ . The continuum  
 2045     is removed by division from both the library reference spectrum and from the unknown's spectrum.  
 2046     From Clark et al., 2003, a public domain image.

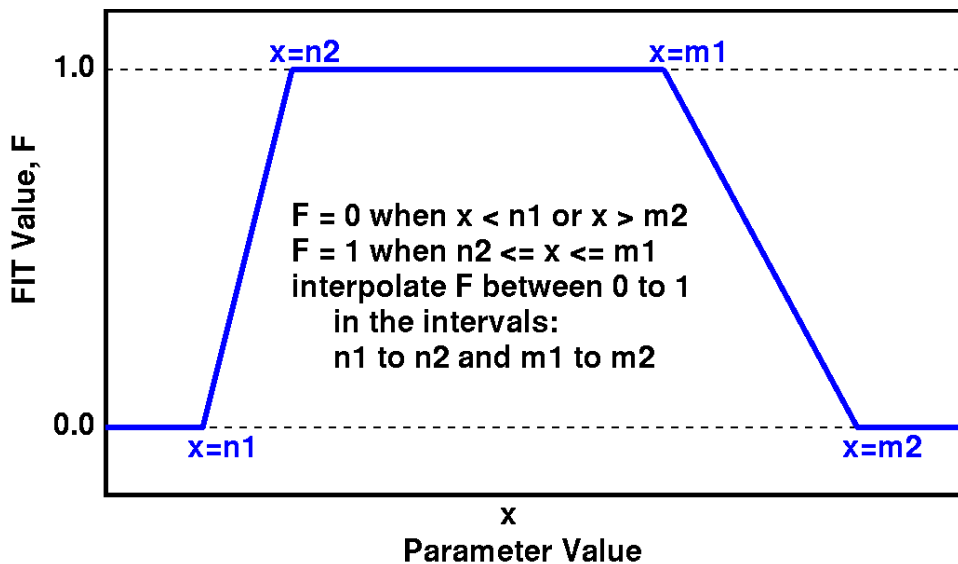
2047  
 2048

2049  
2050



2052 Figure 6. Curved versus straight line continua. For weak spectral features on a curved continuum  
2053 background, straight line continua can lead to false positives (A), errors in band depth (B) and false  
2054 negatives (D). Curved continua (C, E) solve these problems but requires additional continuum  
2055 intervals (4 endpoints instead of 2). The disadvantage of more continuum endpoints is that if one falls  
2056 in another absorption band, it can distort off the cubic spline, creating false positives and false  
2057 negatives. Tetracorder allows for both linear and curved continua to be used.  
2058  
2059

2060

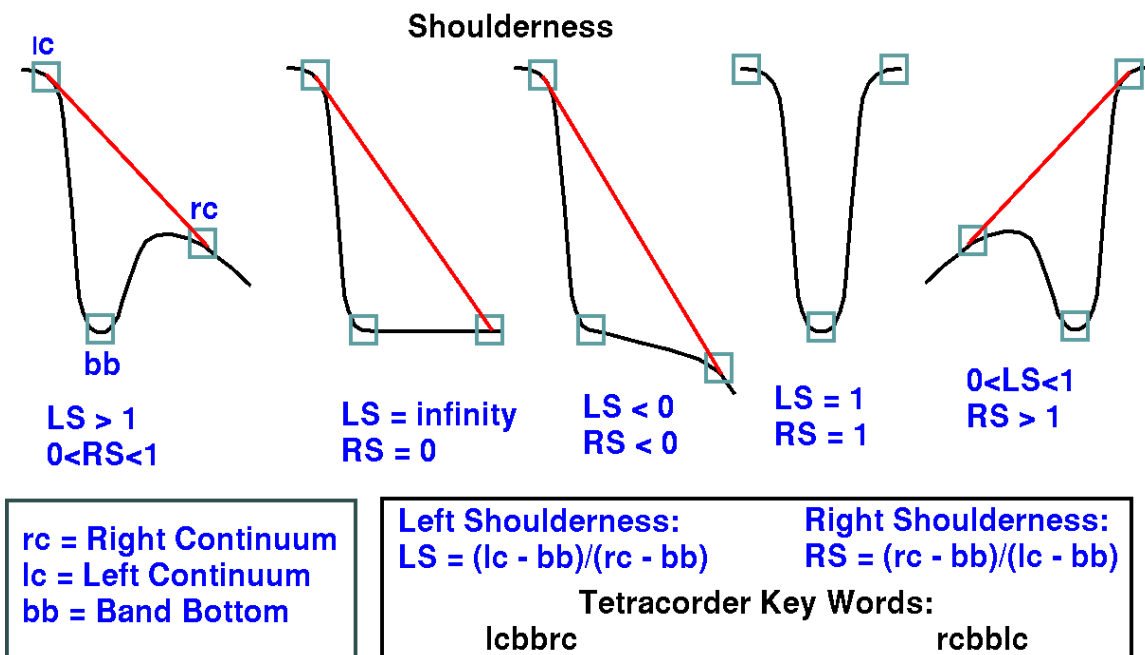


2062 Figure 7. Fuzzy logic. The correlation coefficient (the fit) value is multiplied by the fuzzy logic value.  
 2063 When a parameter value is less than  $n_1$  or greater than  $m_2$ , the fuzzy logic value is set to zero and the  
 2064 fit will be zero. If the parameter value is between  $n_2$  and  $m_1$ , the fuzzy logic value is set to 1.0 and the  
 2065 fit is unchanged. If between  $n_1$  and  $n_2$  or  $m_1$  and  $m_2$ , the fuzzy logic value is interpolated between 0  
 2066 and 1, decreasing the fit value.

2067

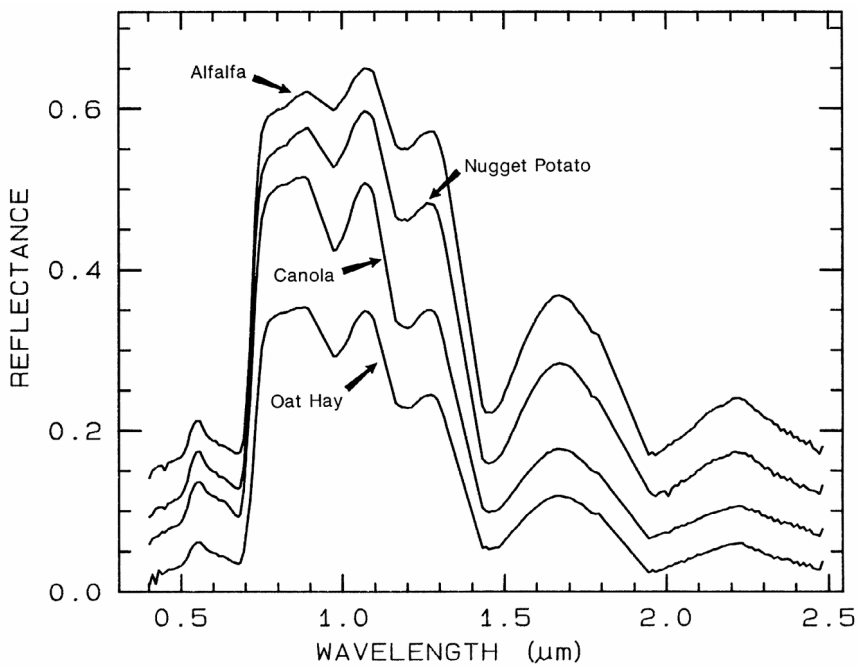
2068

2069



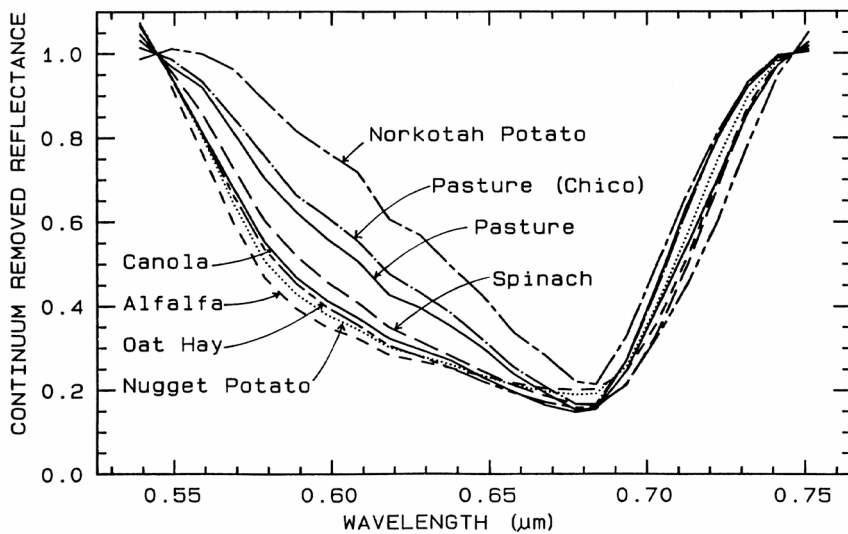
2071 Figure 8. Shoulderness definitions. The red line represents the straight-line continuum between  
 2072 lc and rc.  
 2073

2074



2076 Figure 9a. Vegetation spectra. From Clark, 1999.

2077



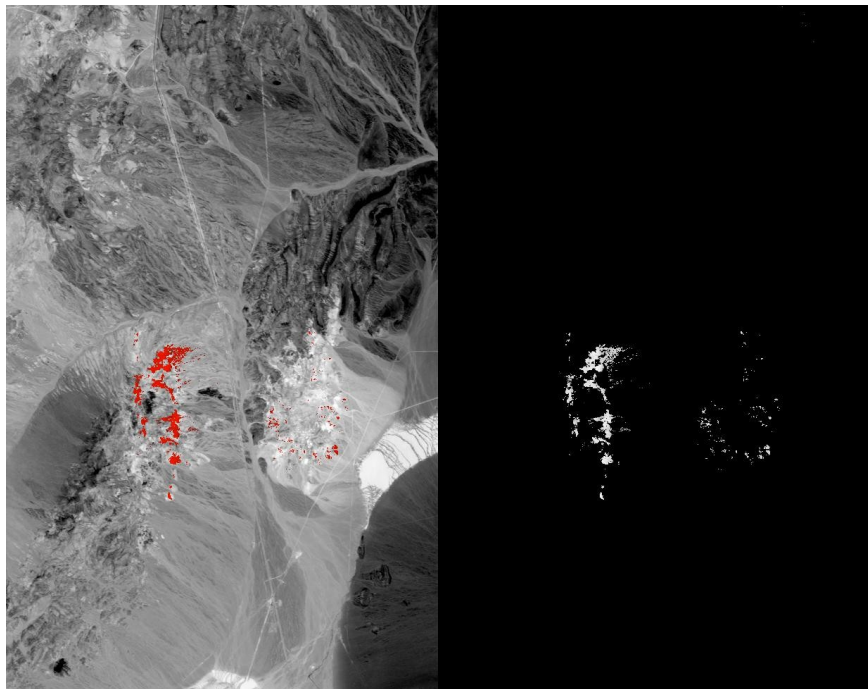
2079

2080 Figure 9b. Vegetation spectra showing shape changes with vegetation type, and the red edge position  
2081 shifts (the edge from  $\sim 0.68$  to  $\sim 0.75 \mu\text{m}$ ). The  $\sim 0.55$  to  $0.65\text{-}\mu\text{m}$  shape changes could also be used.  
2082 From Clark, 1999.

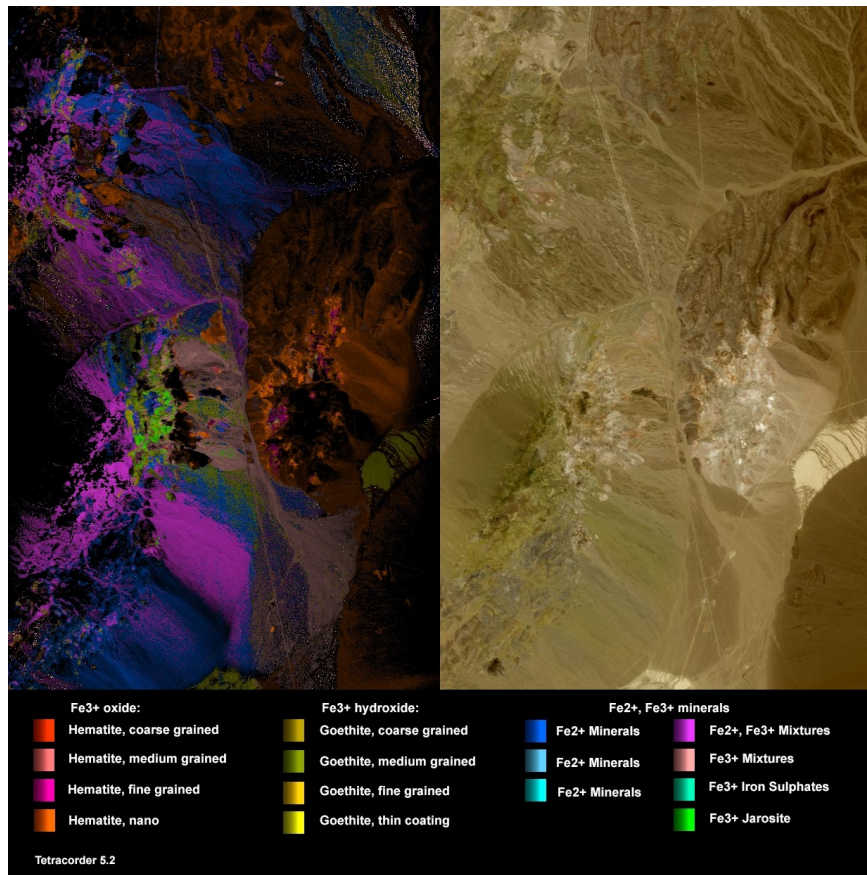
2083

2084

2085  
2086

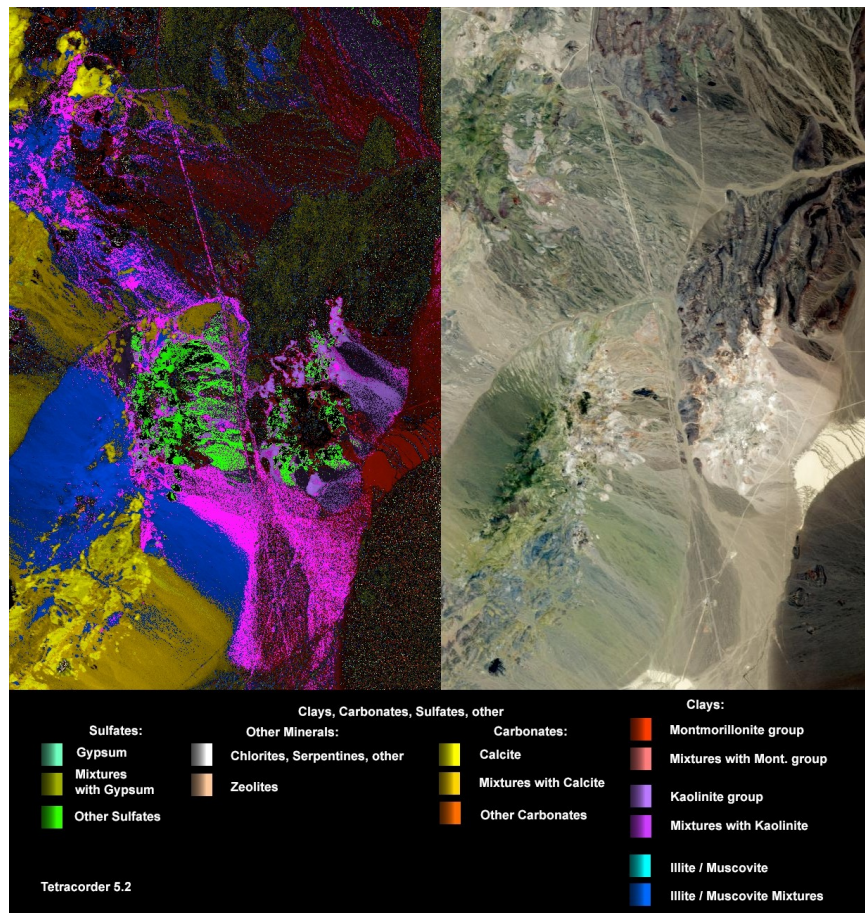


2088 Figure 10. Tetracorder browse product for K-alunite. This browse image includes multiple K-bearing  
2089 alunites into one image. On the left, the pixels containing K-alunite are shown in red on a gray scale  
2090 background, and on the right, white on a black background. This is an auto-generated Tetracorder  
2091 product. These images are found in the results.dual.group.\* directories.  
2092  
2093



2095      Figure 11a. Group 1 minerals mapped. This is a Tetracorder 5.27 standard product, expert system  
 2096      5.27d1. The image on the right is an approximate true color image using red, green and blue channels  
 2097      from the spectrometer data. It is approximate because only a single channel for each color is used  
 2098      instead of a spectral profile of human eye response. The user can define the channels used for each  
 2099      sensor. The channels used for this 1995 AVIRIS data are 30, 20 and 10 for red, green, and blue,  
 2100      respectively.

2101  
 2102  
 2103

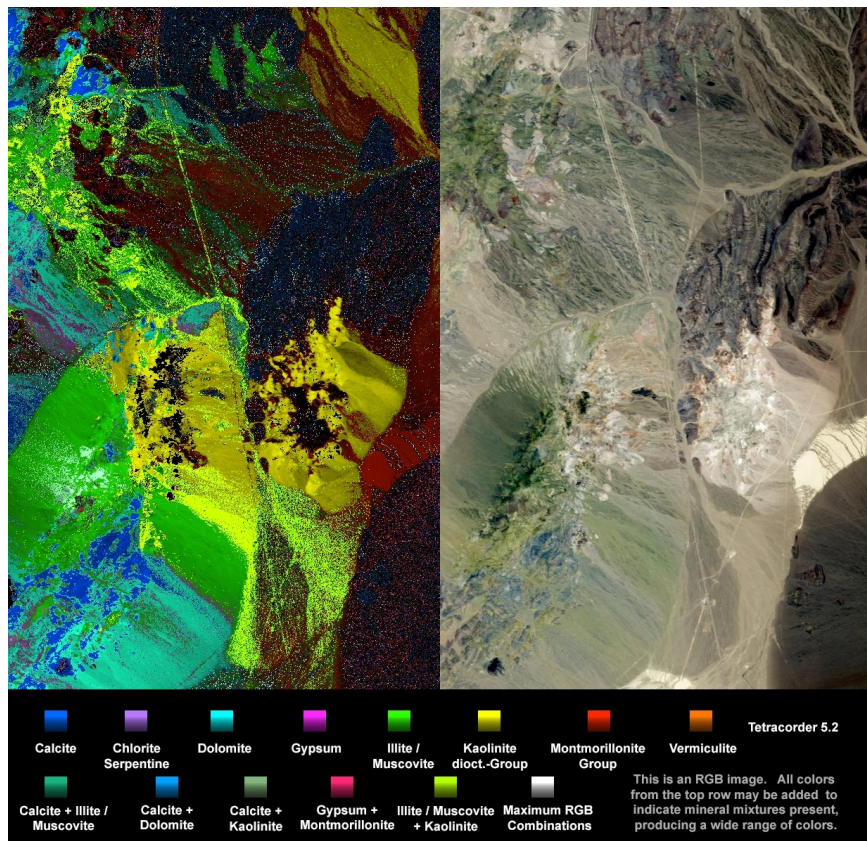


2106 Figure 11b. Group 2 minerals mapped. This is a Tetracorder standard product.

2107

2108

2109



2110 Figure 11c. EMIT 8, custom RGB color composite product. This is a Tetracorder standard product.

2111

2112

2113

2114



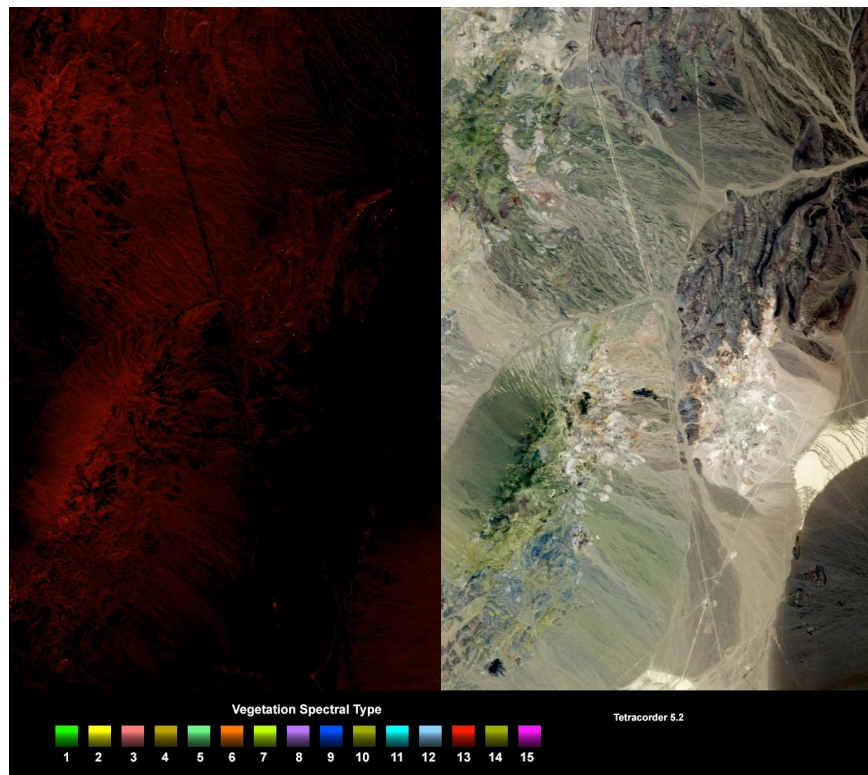
2116 Figure 11d. Muscovite aluminum content in the muscovite octahedral sites illustrates specialty product  
2117 useful for specific applications. Constructing additional products like this is copying and modifying a  
2118 simple script to put in the materials desired and their colors. This is a Tetracorder standard product.

2119

2120

2121

2122

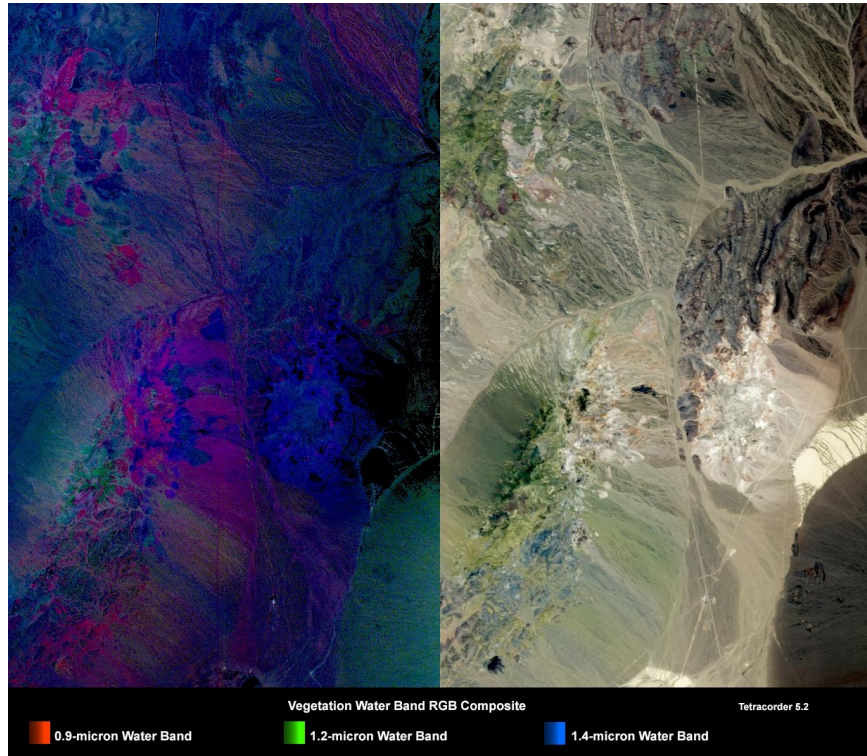


2124 Figure 11e. Detected vegetation spectral type. This is a Tetracorder standard product.

2125

2126

2127



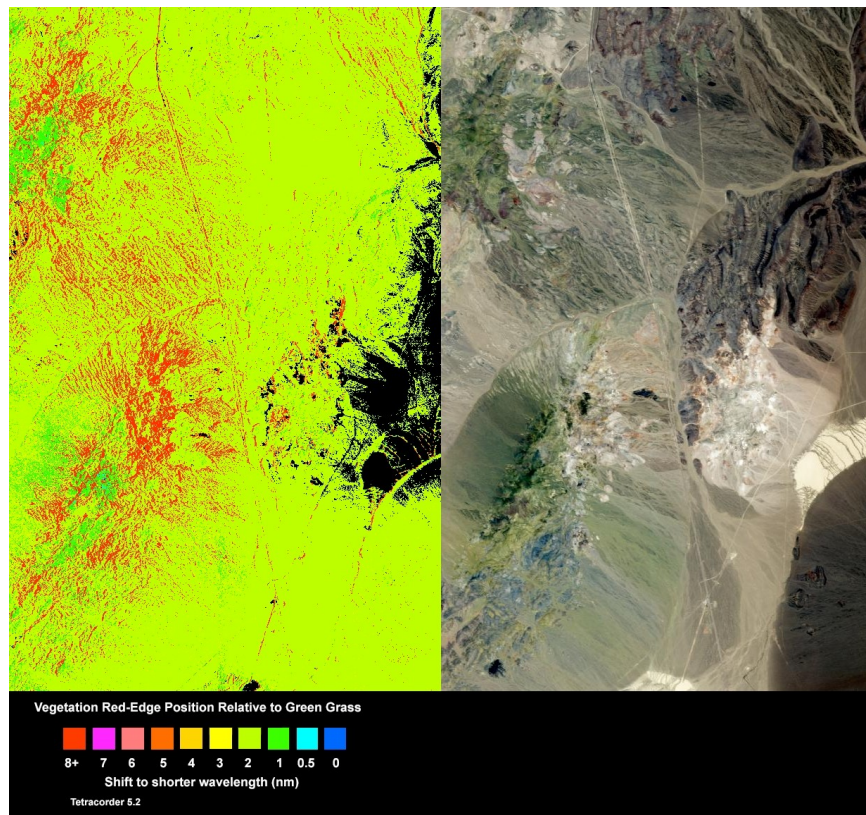
2129 Figure 11f. Vegetation water content. The water image on the left is an RGB color composite. This is  
2130 a Tetracorder standard product.

2131

2132

2133

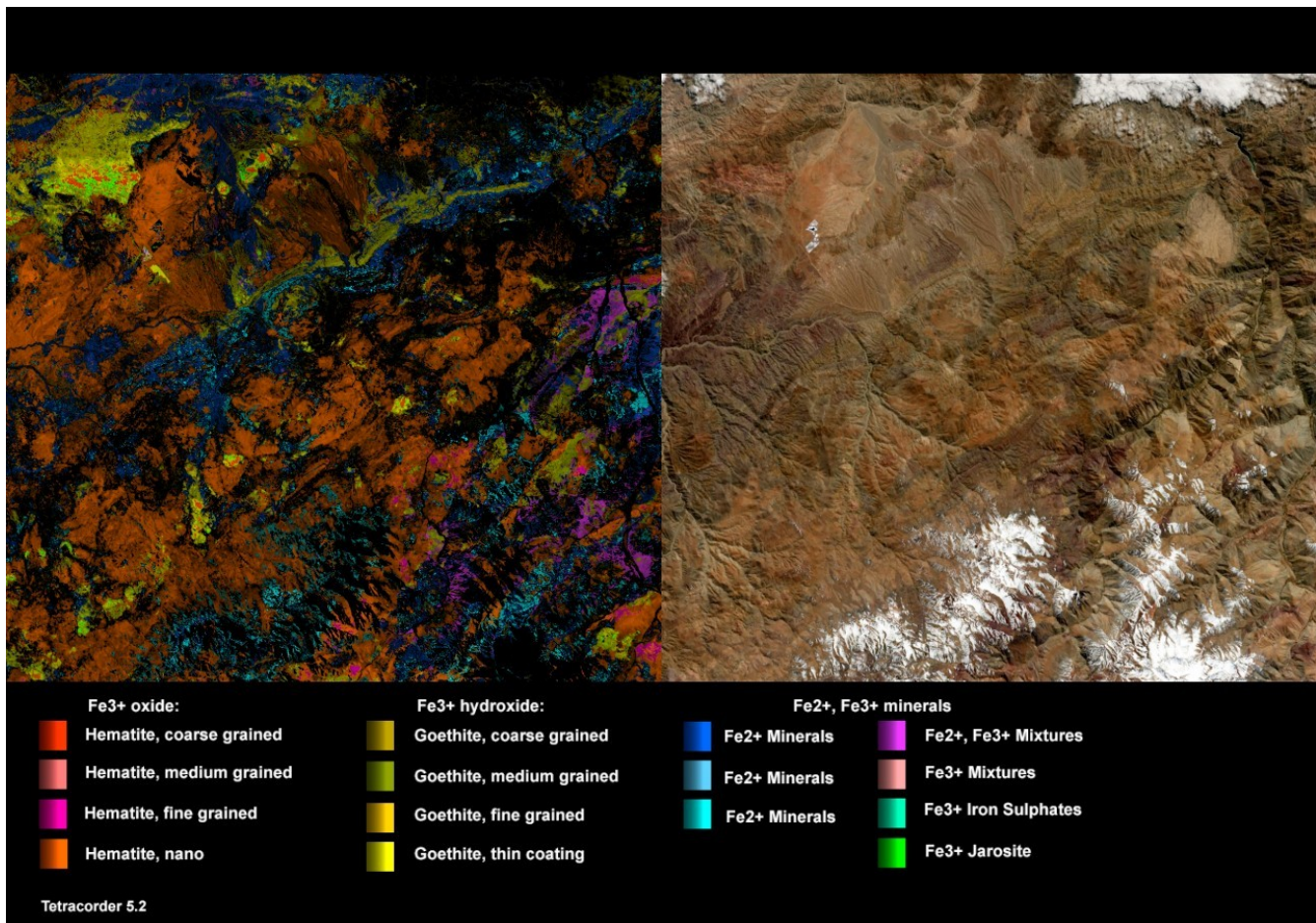
2134



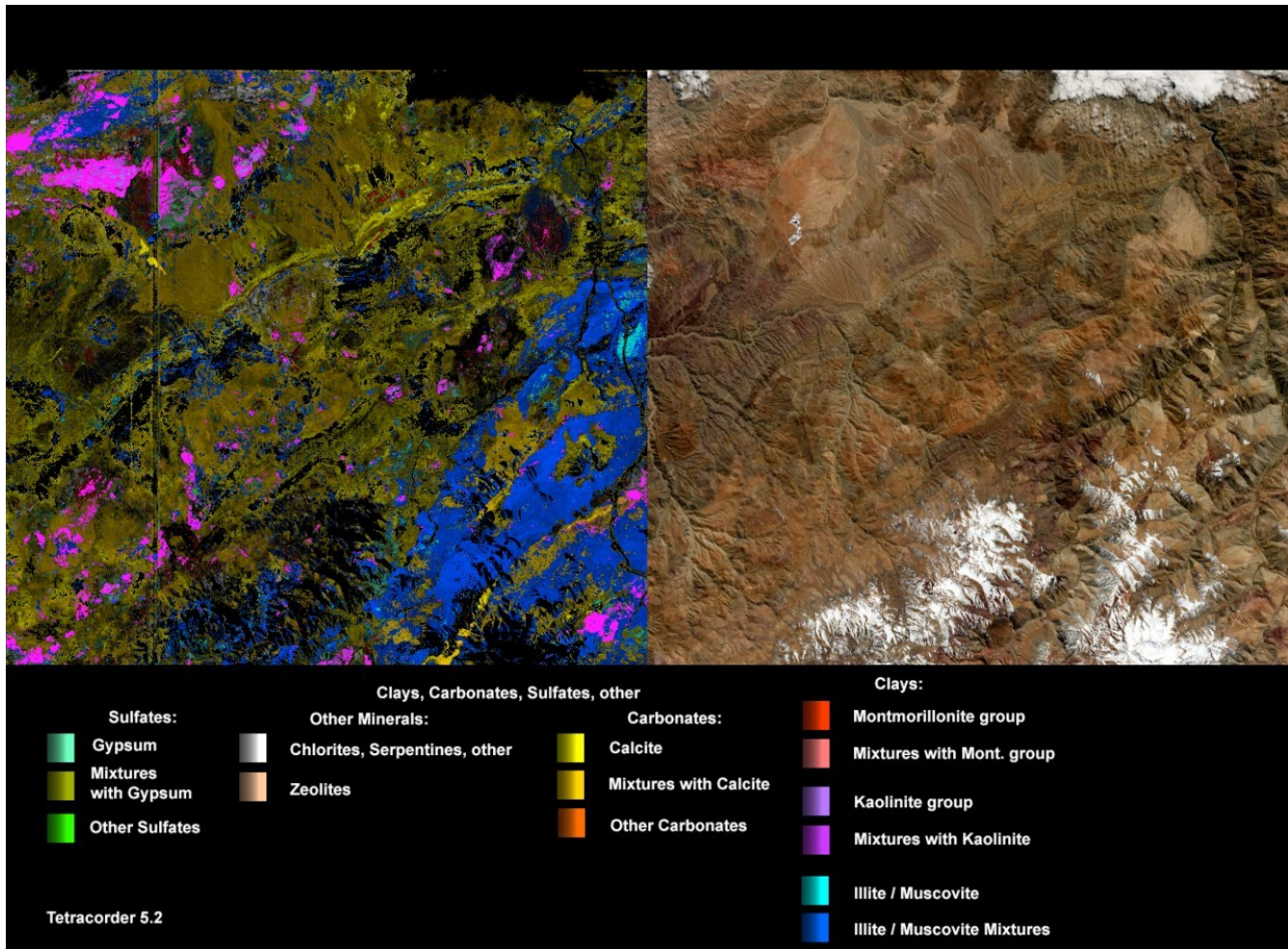
2136 Figure 11g. Vegetation red-edge position. This is a Tetracorder standard product.

2137

2138

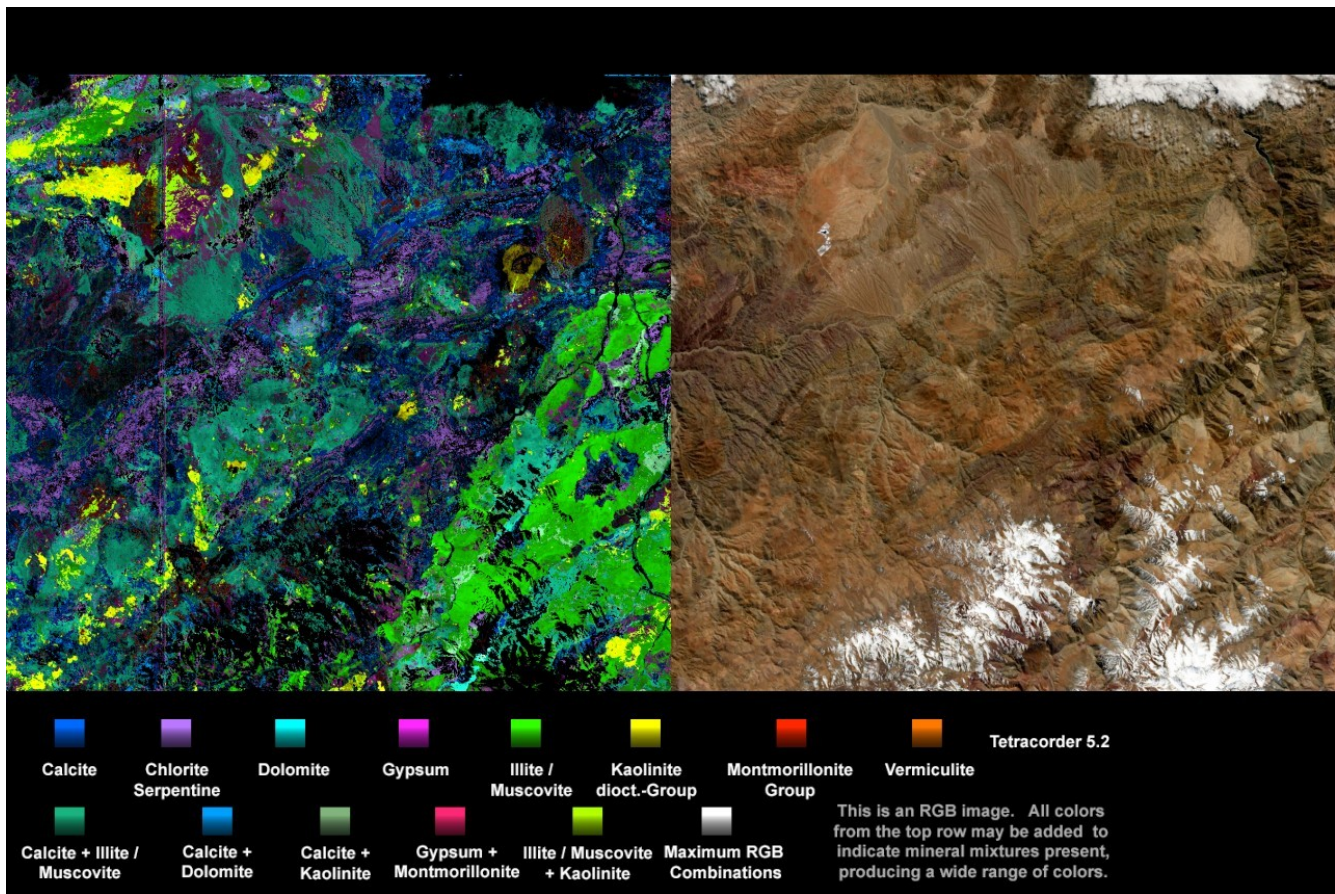


2141 Figure 12a. EMIT scene emit20220831t171631\_o24311\_s000\_l2a\_rfl\_b0106\_v01 Tetracorder  
 2142 standard product for  $\text{Fe}^{2+}$  and  $\text{Fe}^{3+}$  bearing mineral electronic absorptions in the visible to very-near  
 2143 infrared spectral range. The EMIT swath width is approximately 77 km, in this non-ortho-corrected  
 2144 scene over Chile. This is a Tetracorder standard product.  
 2145



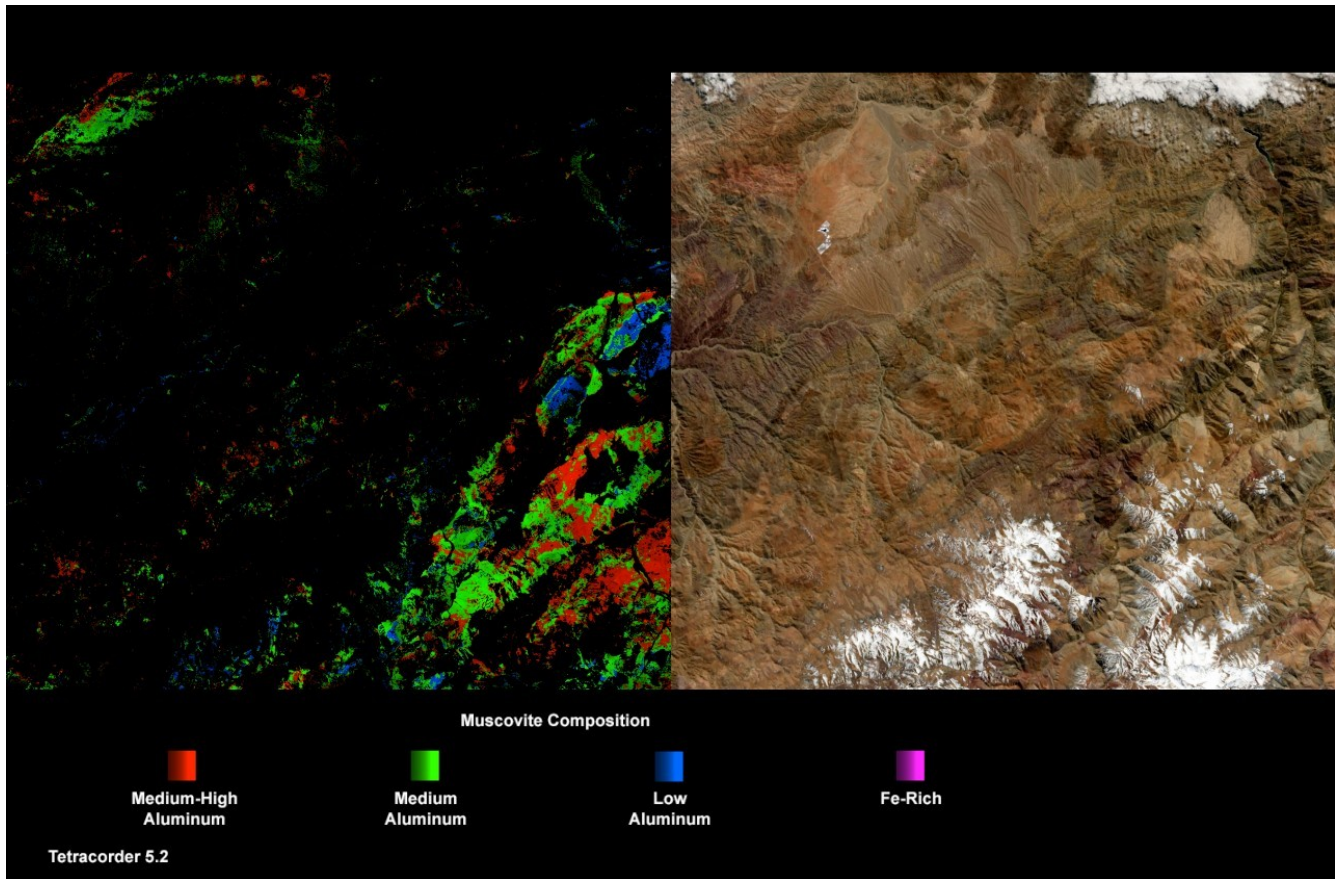
2148 Figure 12b. EMIT scene emit20220831t171631\_o24311\_s000\_l2a\_rfl\_b0106\_v01 Tetracorder  
 2149 standard product for vibrational absorptions in the near-infrared region. The EMIT swath width is  
 2150 approximately 77 km, in this non-ortho-corrected scene over Chile. This is a Tetracorder standard  
 2151 product.

2152



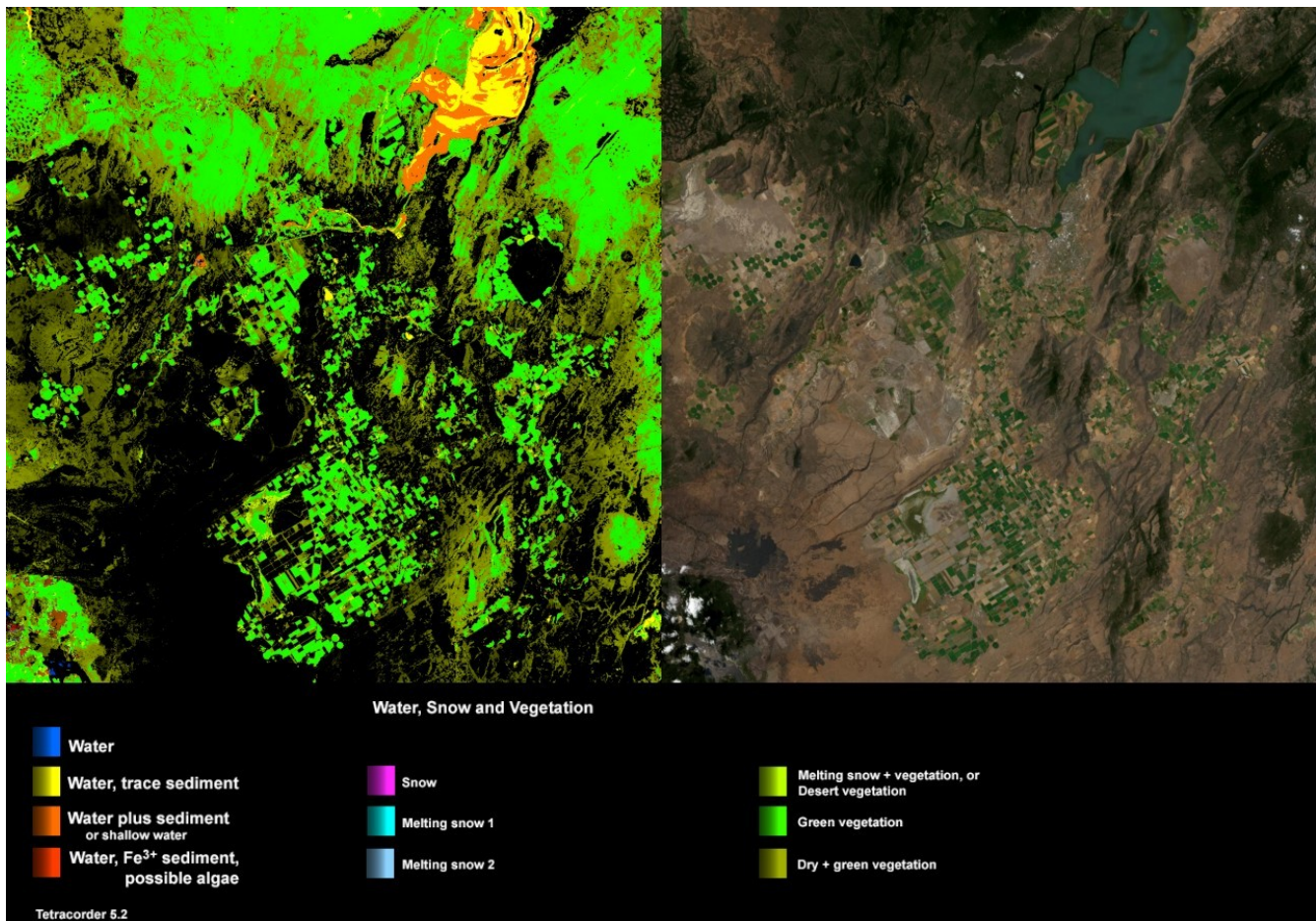
2155     Figure 12c. EMIT scene emit20220831t171631\_o24311\_s000\_l2a\_rfl\_b0106\_v01 Tetracorder  
 2156     standard product for the EMIT 8 minerals (excluding hematite and goethite): calcite,  
 2157     chlorite/serpentine, dolomite, gypsum, illite/muscovite, kaolinite-dioctahedral group, montmorillonite  
 2158     group, and vermiculite. The EMIT swath width is approximately 77 km, in this non-ortho-corrected  
 2159     scene over Chile. This is a Tetracorder standard product.  
 2160

2161



2163 Figure 12d. EMIT scene emit20220831t171631\_o24311\_s000\_l2a\_rfl\_b0106\_v01 Tetracorder  
2164 standard product for aluminum content in the octahedral layer in muscovite/illite. The EMIT swath  
2165 with is approximately 77 km, in this non-ortho-corrected scene over Chile. This is a Tetracorder  
2166 standard product.  
2167

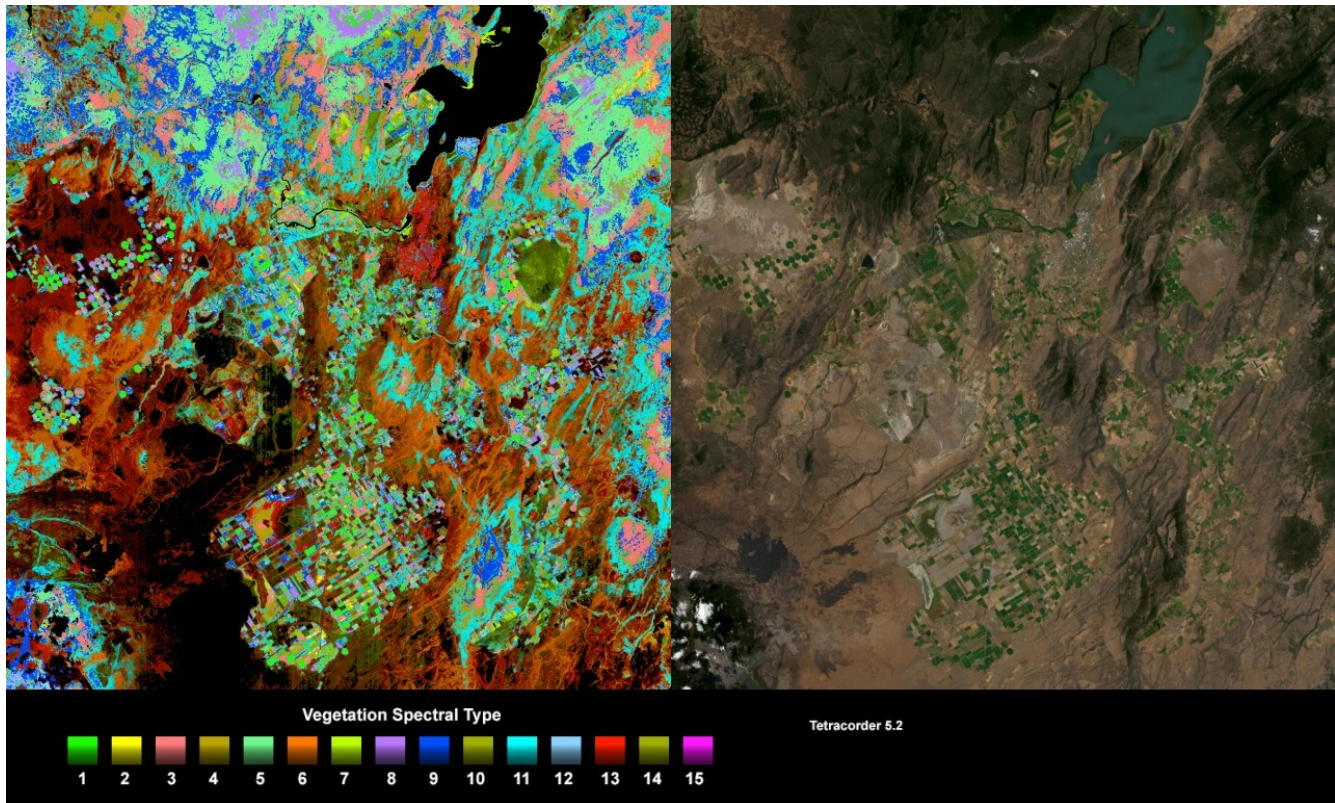
2168  
2169



2171 Figure 13a. EMIT scene emit20220814t223444\_o22615\_s000\_l2a\_rfl\_b0106\_v01 Tetracorder  
2172 standard product showing vegetation, snow and and melting snow, and water sediments and another  
2173 contaminants. Each of these are combinations of images showing finer detail. The EMIT swath with is  
2174 approximately 77 km, in this non-ortho-corrected scene on the U. S. California-Nevada border. North  
2175 is to the upper right. This is a Tetracorder standard product.

2176  
2177  
2178

2179



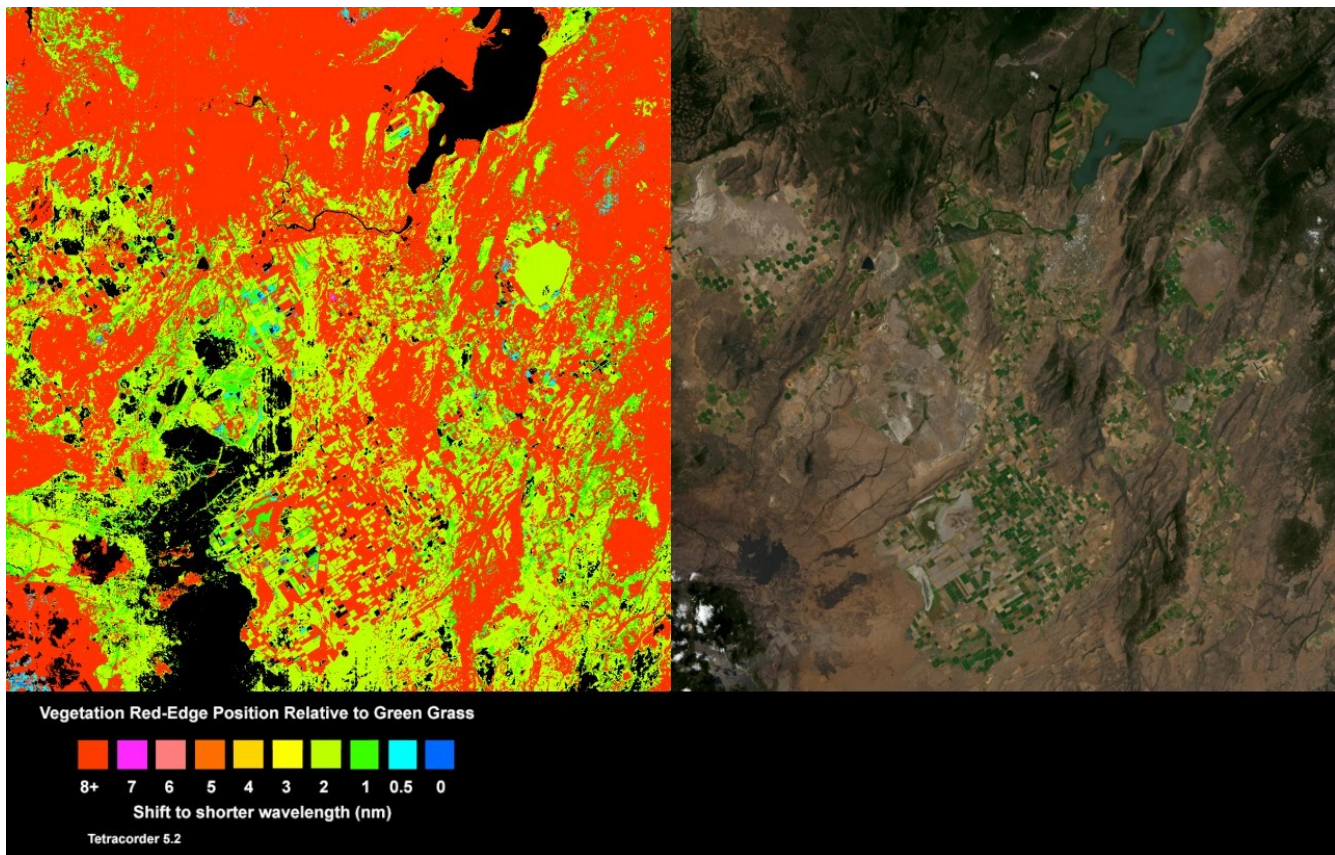
2181 Figure 13b. EMIT scene emit20220814t223444\_o22615\_s000\_l2a\_rfl\_b0106\_v01 Tetracorder  
2182 standard product showing vegetation spectral type. The spectral type was determined using the shape  
2183 of the chlorophyll absorption like that shown in Figure 9b. The EMIT swath width is approximately 77  
2184 km, in this non-ortho-corrected scene on the U. S. California-Nevada border. North is to the upper  
2185 right. This is a Tetracorder standard product.

2186

2187

2188

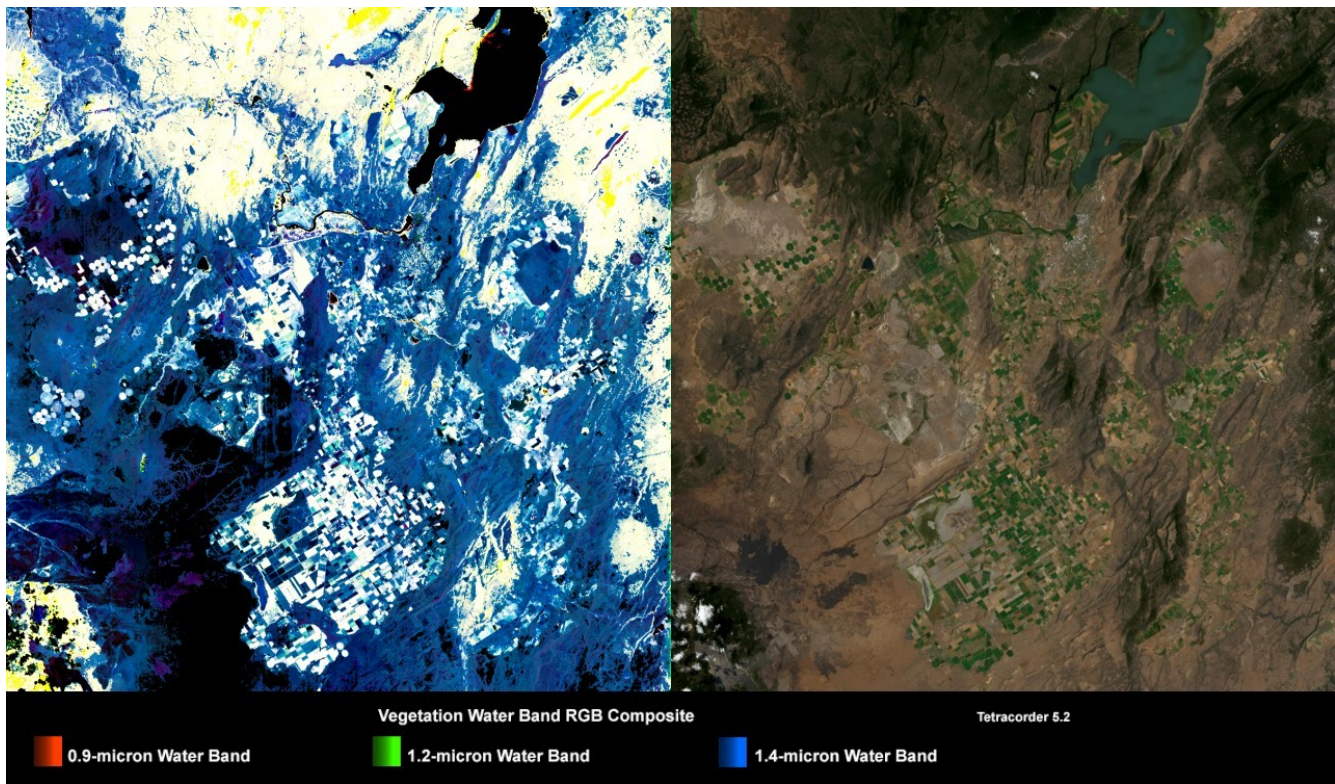
2189



2191 Figure 13c. EMIT scene emit20220814t223444\_o22615\_s000\_l2a\_rfl\_b0106\_v01 Tetracorder  
2192 standard product showing the chlorophyll absorption edge position near  $0.7 \mu\text{m}$  relative to the position  
2193 of a green lawn grass. The EMIT swath width is approximately 77 km, in this non-ortho-corrected scene  
2194 on the U. S. California-Nevada border. North is to the upper right. This is a Tetracorder standard  
2195 product.

2196

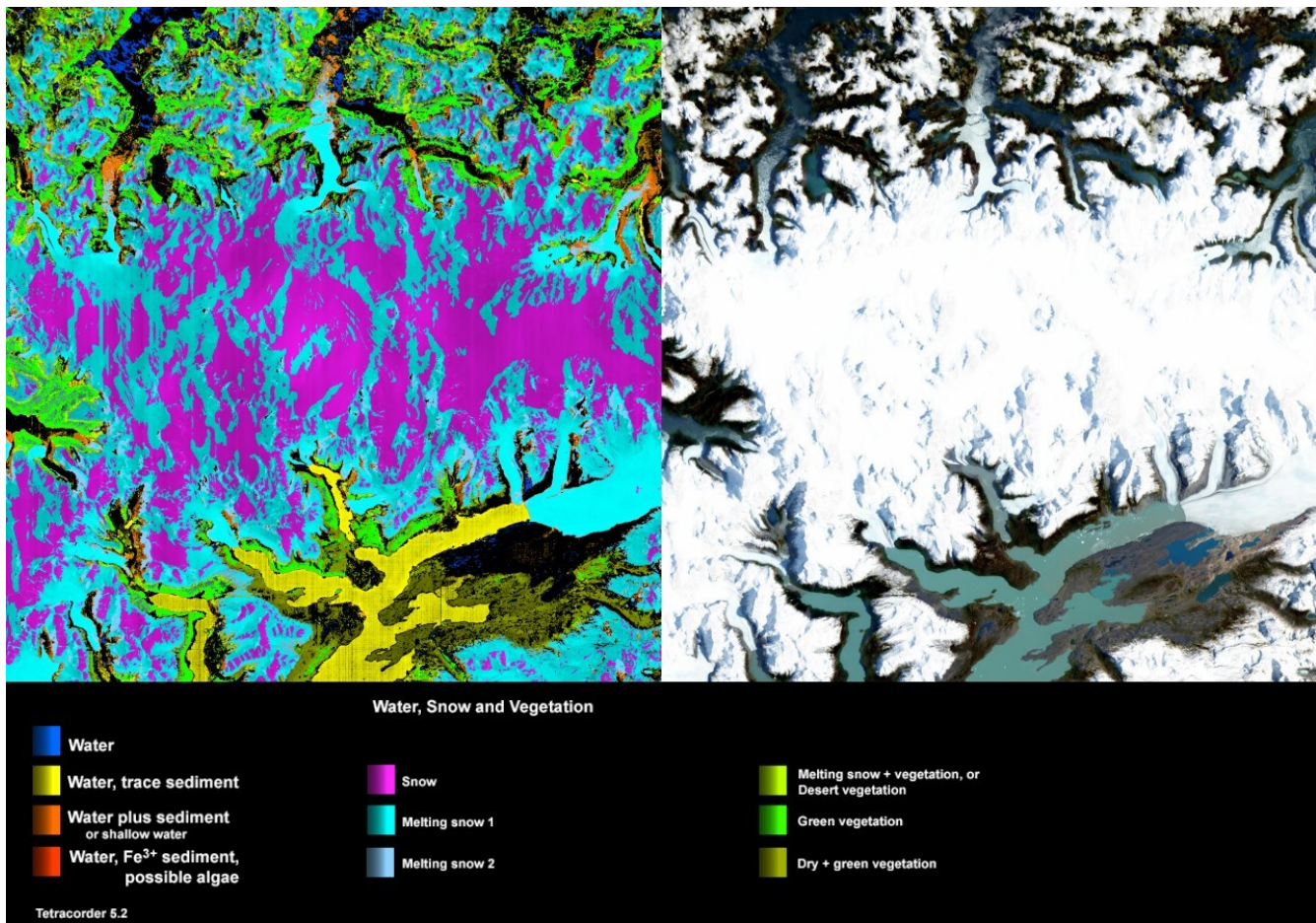
2197



2200 Figure 13d. EMIT scene emit20220814t223444\_o22615\_s000\_l2a\_rfl\_b0106\_v01 Tetracorder  
 2201 standard product showing relative strengths of the water absorptions in vegetation in the RGB  
 2202 composite image. Blue areas have relatively weak 0.9 and 1.2- $\mu$ m water absorptions thus less water.  
 2203 White areas have three absorptions strong, thus higher water content. The EMIT swath width is  
 2204 approximately 77 km, in this non-ortho-corrected scene on the U. S. California-Nevada border. North  
 2205 is to the upper right. This is a Tetracorder standard product.

2206  
 2207  
 2208  
 2209

2210



2212 Figure 14. EMIT scene emit20220912t154138\_o25510\_s001\_l2a\_rfl\_b0106\_v01 Tetracorder  
2213 standard product showing a mountain snow scene in the Chile-Argentina border. The snow shows no  
2214 detectable melting at higher elevations (magenta), but melting at lower elevations (cyan, light blue).  
2215 Also shown are sediments in water from the snow melt. The EMIT swath width is approximately 77  
2216 km. This is a Tetracorder standard product.

2217

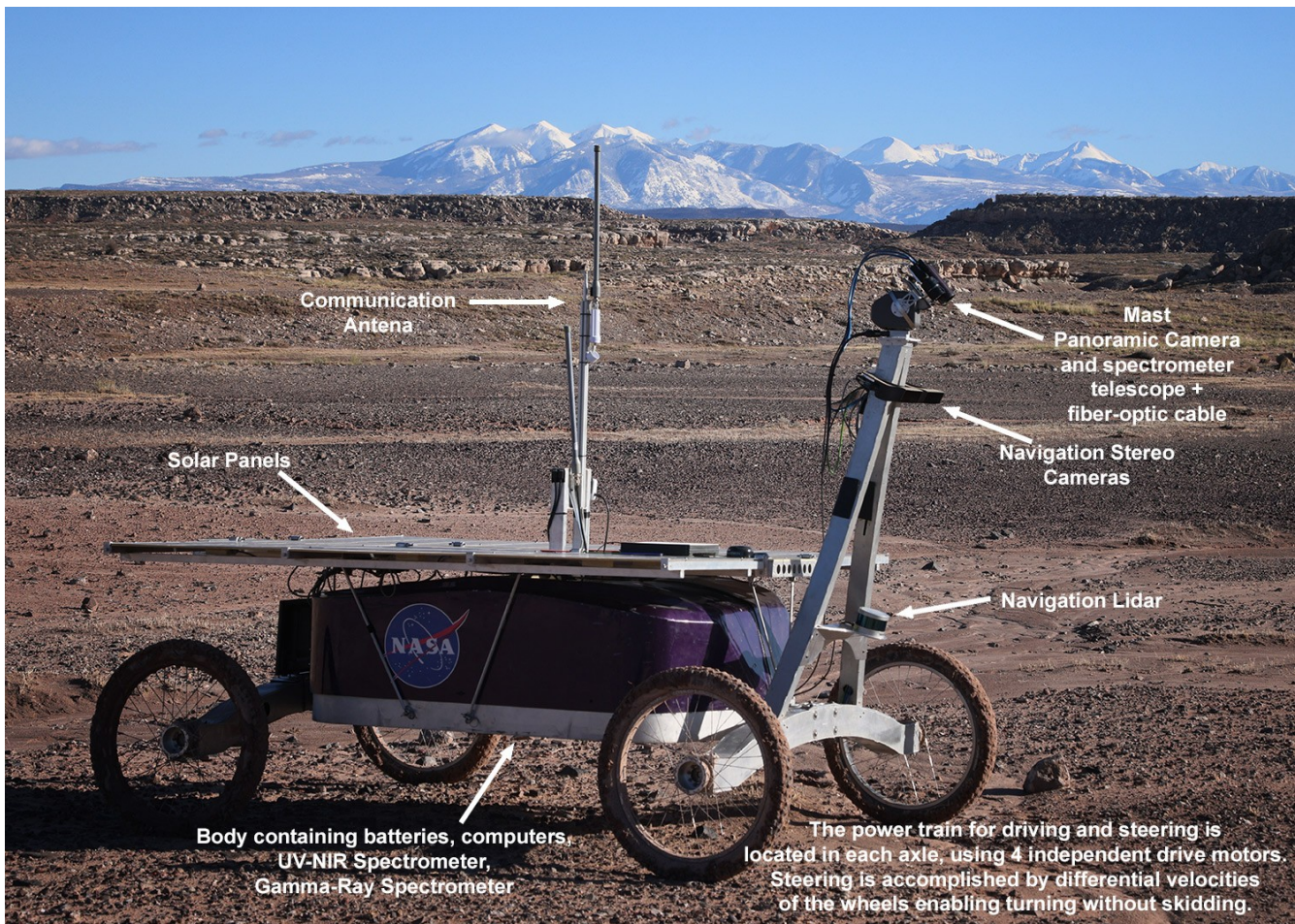
2218

2219

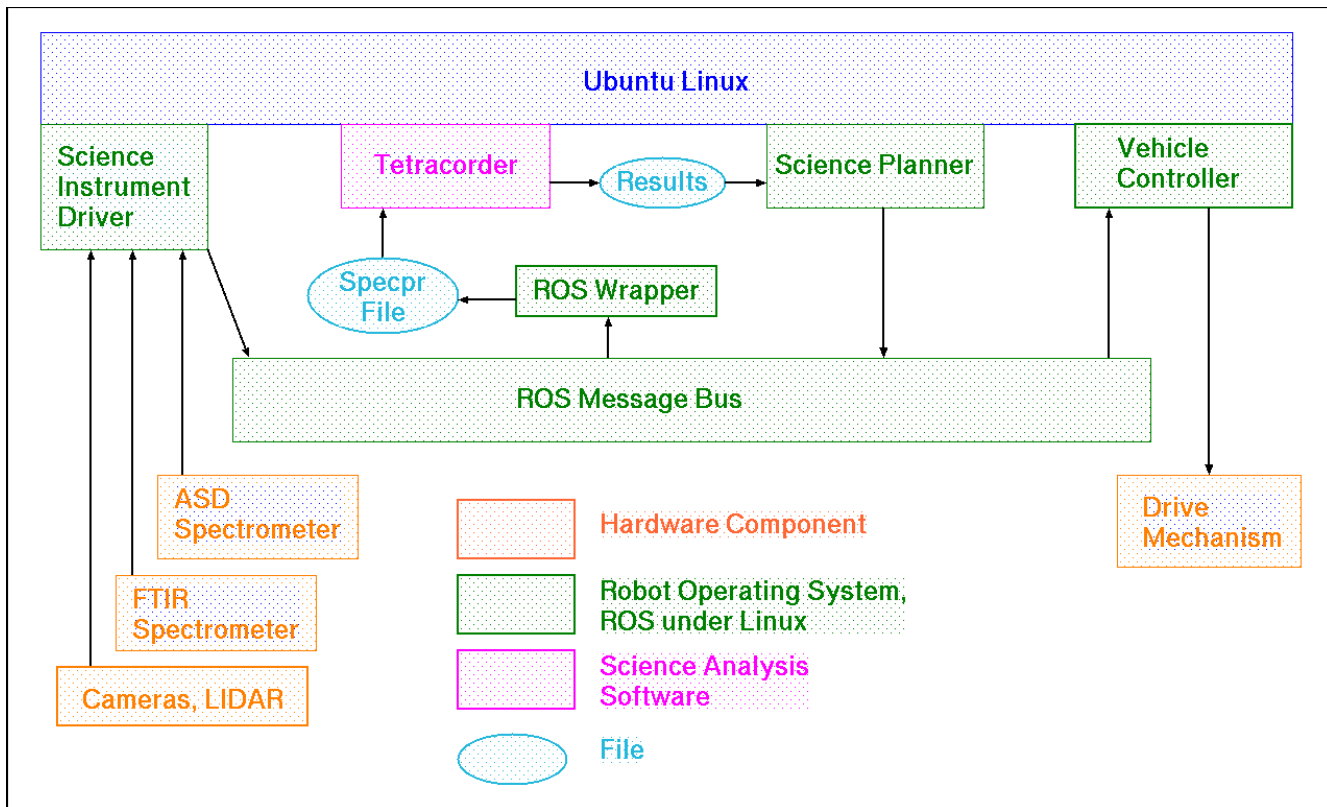
2220

2221

2222  
2223

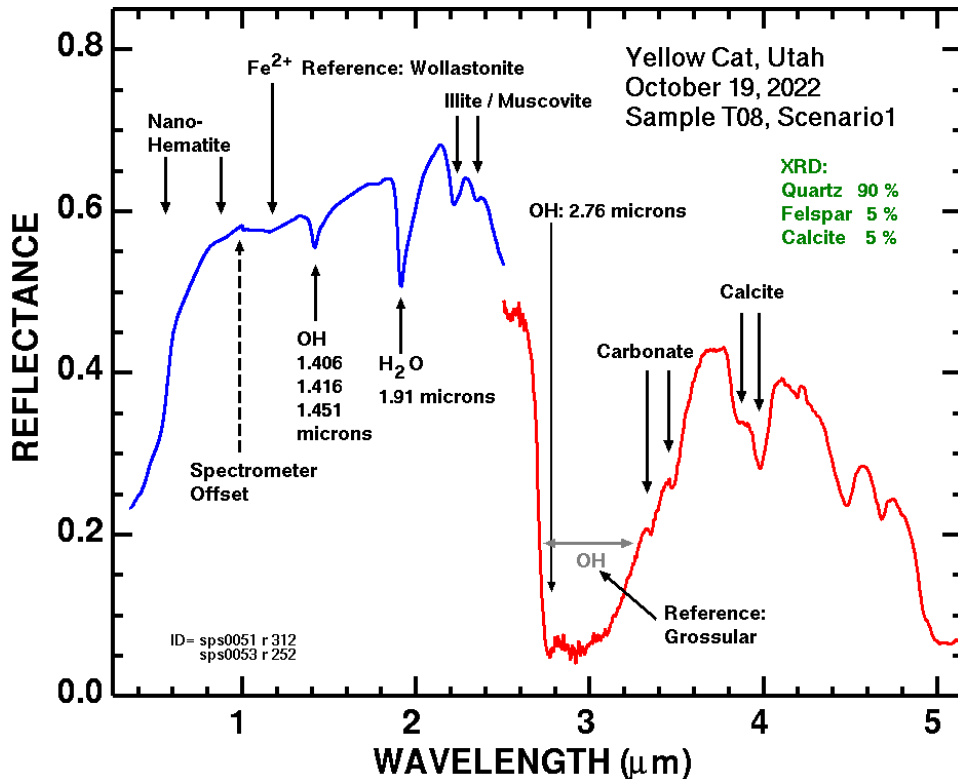


2225 Figure 15. Zoë rover in the field. For scale, the height of the Mast is about 3 meters. Tetracorder runs  
2226 on a Ubuntu Linux computer in the body of the rover, analyzing data real time from an Analytical  
2227 Spectral Devices, ASD, spectrometer covering 0.35 to 2.5  $\mu\text{m}$ . The spectrometer is located in the body  
2228 under the solar panels and receives light via a fiber optic feed from a telescope mounted at the top of  
2229 the mast. Here the telescope and mast camera are point down in front of the rover to analyze data as  
2230 the rover autonomously drives forward. The view is to the southeast toward the La Sal Mountains near  
2231 Moab Utah.  
2232



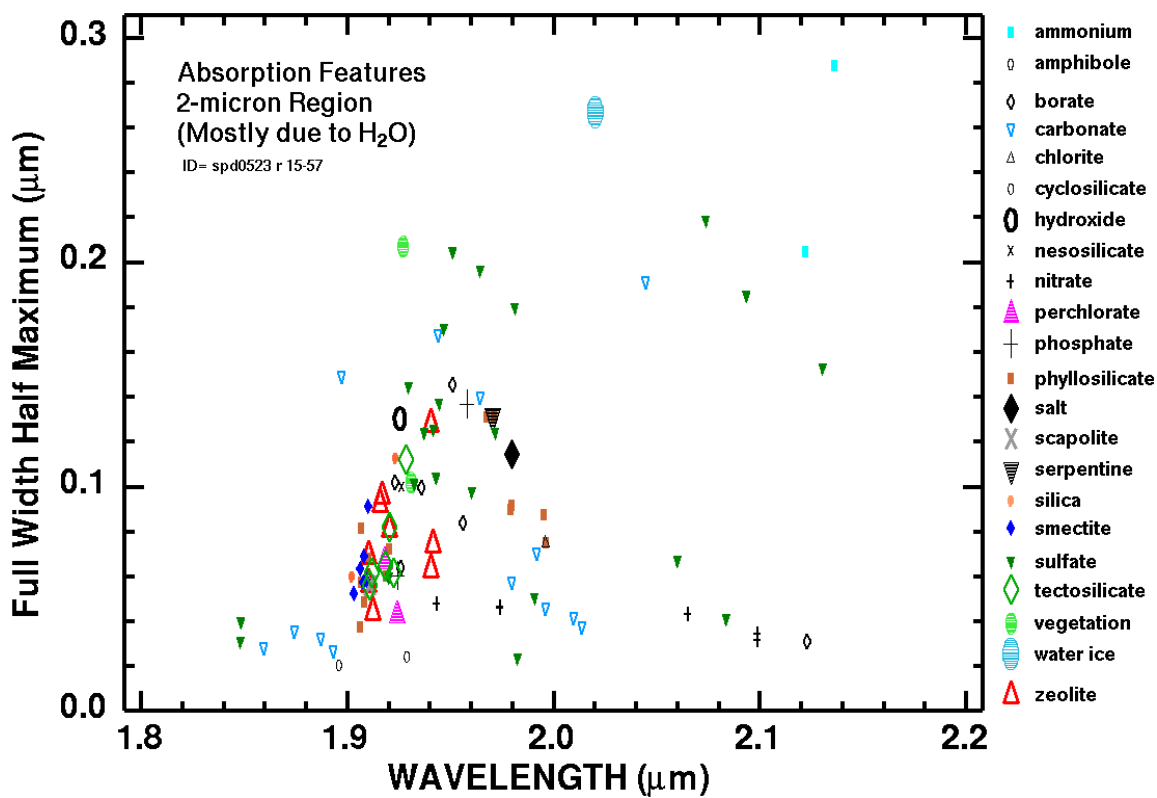
2235 Figure 16. A simplified version of the data flow and how Tetracorder is integrated into the system.  
 2236 Data from the ASD spectrometer is collected and pushed to the ROS message bus. Tetracorder is  
 2237 started using a ROS wrapper program and spectra are fed by updating a specpr file. Tetracorder is run  
 2238 using the 'single spectrum' mode for this operation, following the growing specpr file. After processing  
 2239 the spectra, Tetracorder writes the results to a results file which is then read by the Science Planner  
 2240 which analyzes the detections and generates guidance plans. The Vehicle Controller picks up the  
 2241 plans generated by the Science Planner and gives instructions to the drive mechanism to visit the next  
 2242 location.  
 2243  
 2244  
 2245

2246  
2247  
2248  
2249



2251 Figure 17. Spectra and XRD results obtained by the Zoë rover contact instruments during the Yellow  
2252 Cat, Utah October 2022 field campaign. The labeled spectral features are the Tetracorder  
2253 identifications. XRD results were not obtained real time for the rover to use. The blue spectrum is  
2254 from an ASD spectrometer, and the red spectrum is from an FTIR spectrometer, both contact  
2255 instruments. Flagged features (arrows) are Tetracorder identifications. The Fe<sup>2+</sup> Wollastonite is an  
2256 identification of and Fe<sup>2+</sup> absorption and not necessarily diagnostic of Wollastonite, only that  
2257 Wollastonite was the reference spectrum. Features with no arrows were not evaluated by Tetracorder.  
2258 Note that the carbonate features near 3.4  $\mu\text{m}$ , could be misidentified as organics if there are no  
2259 carbonate reference spectra for this wavelength region in the Tetracorder expert system.

2260  
2261  
2262

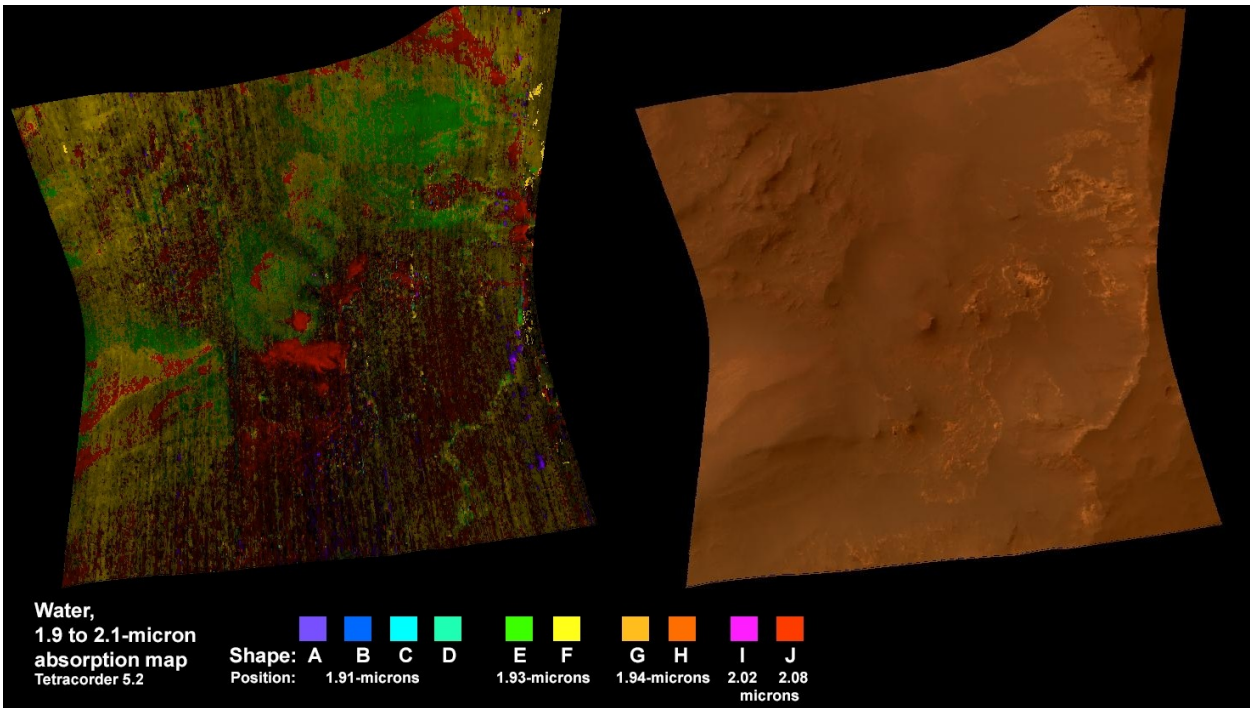


2265 Figure 18. Water absorption positions and widths derived from the USGS spectral library 06 (Clark et  
2266 al., 2007) for materials measured in a dry environment.

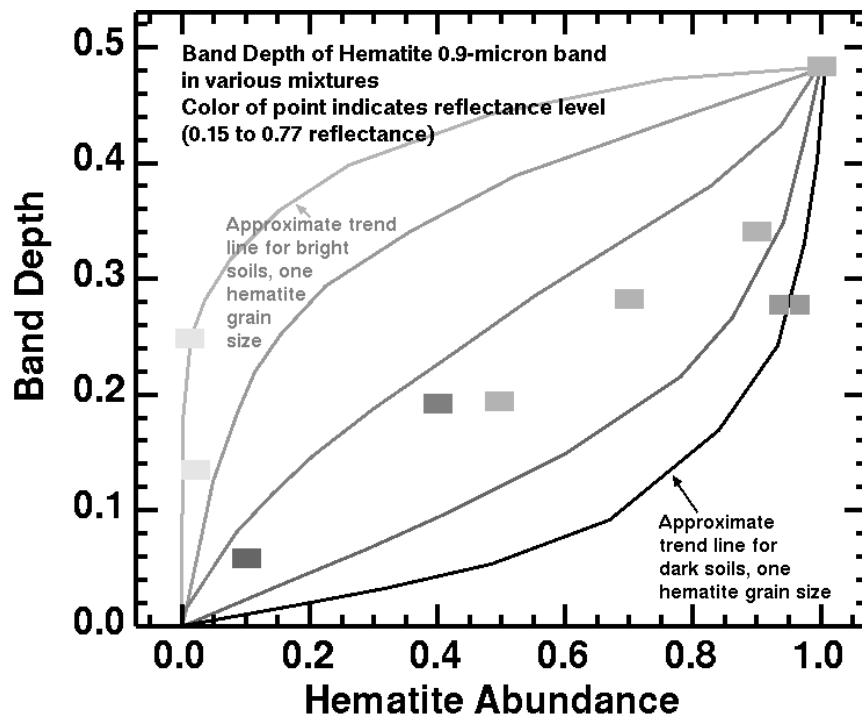
2267

2268

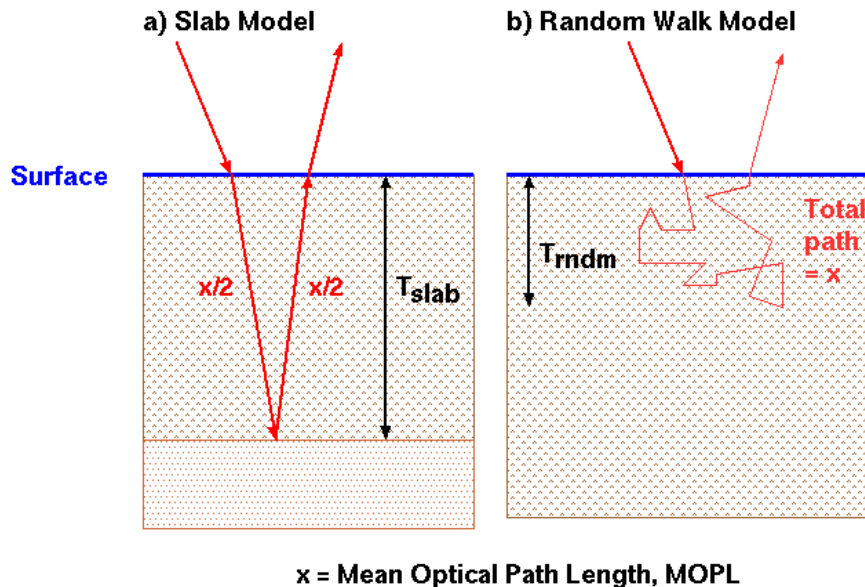
2269



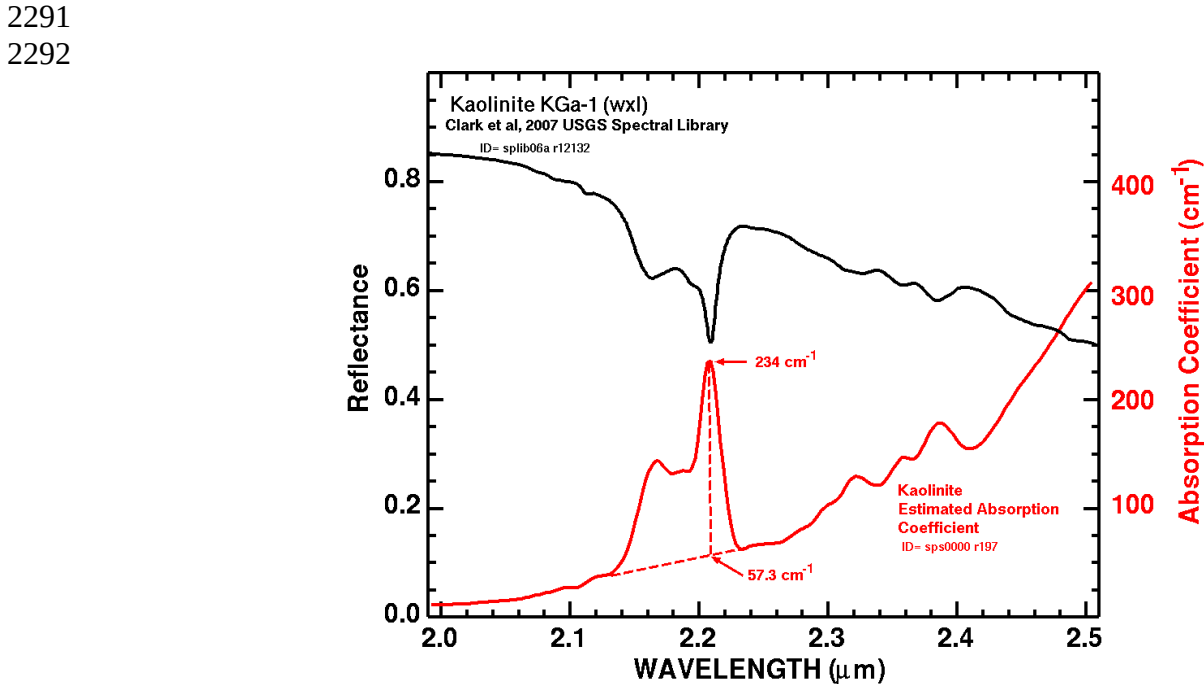
2272 Figure 19. Tetracorder standard product showing the 1.9- $\mu\text{m}$  water band position for Mars  
 2273 Reconnaissance Orbiter, Compact Reconnaissance Imaging Spectrometer for Mars (CRISM) image  
 2274 cube FRT0000B385\_07\_IF164J\_MTR3. Red indicates a very long 1.9- $\mu\text{m}$  band position typical of  
 2275 sulfates. Absorptions indicate the sulfate kieserite is present. Green and yellow, indicating absorptions  
 2276 in the 1.93- $\mu\text{m}$  region are less diagnostic, consistent with phyllosilicates or other sulfates. Some  
 2277 montmorillonite mapped in the green area near the upper right corner based on detection of a 2.2- $\mu\text{m}$   
 2278 feature.



2280 Figure 20. Band depth of the Hematite 0.9- $\mu\text{m}$  band as a function of abundance and continuum  
2281 reflectance (lightness of the gray rectangles). The relationship can be considered piece wise linear as  
2282 long as one stays within the bounds where linearity is valid. The trend lines are derived from models.  
2283  
2284  
2285  
2286



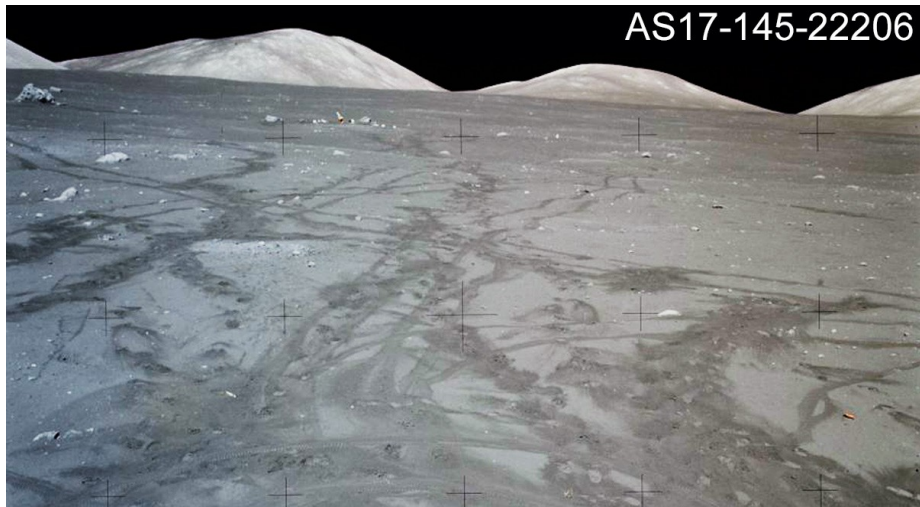
2288 Figure 21. a) The non-scattering slab model used the derived MOPL from optical constants and is used  
2289 in Model 2. b) The random walk model uses the derived MOPL from optical constants and is used in  
2290 Models 3 and 4.



2293 Figure 22. Reflectance and estimated absorption coefficients for kaolinite in the USGS spectral library  
2294 6 (Clark et al., 2007). The delta absorption coefficient,  $\Delta k = k_b - k_c = 234 - 57.3 = 176.7 \text{ cm}^{-1}$ . From the  
2295 observed band depth in the reflectance spectrum, the MOPL = 24  $\mu\text{m}$ .

2296  
2297  
2298

2299



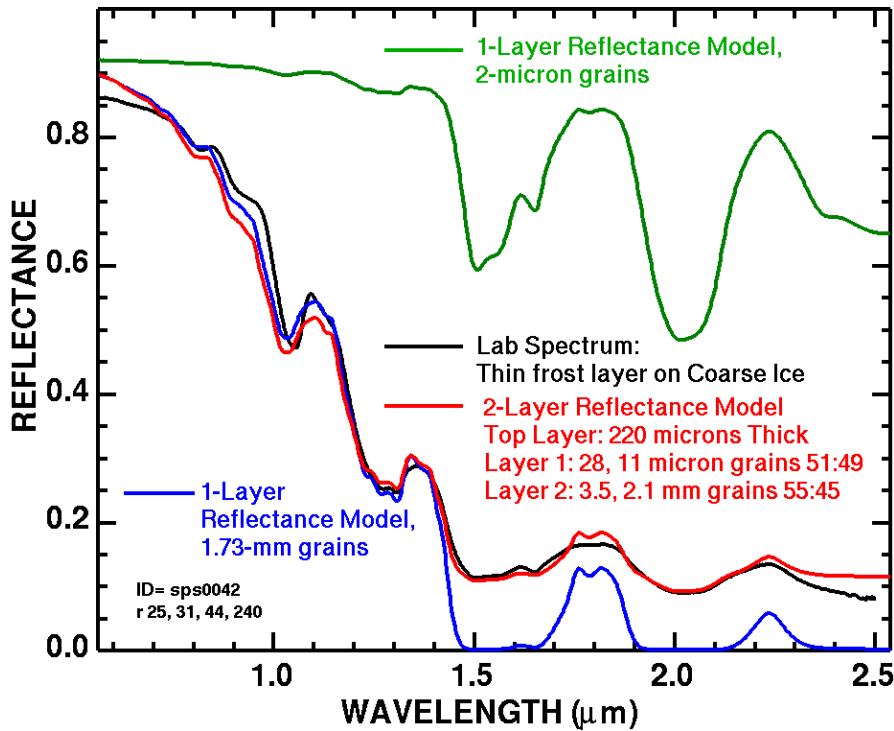
2301 Figure 23. Image of the lunar surface with rover tracks showing the disturbed soil is darker and  
2302 different in color than the surface, indicating changes in grain size and/or composition  
2303 with depth. Contrast has been increased from the original to show the tracks better. AS17-145-22206  
2304 Apollo 17, 1972 Hasselblad image taken post Extravehicular Activity EVA 3. The original film  
2305 magazine was labeled D.

2306

2307

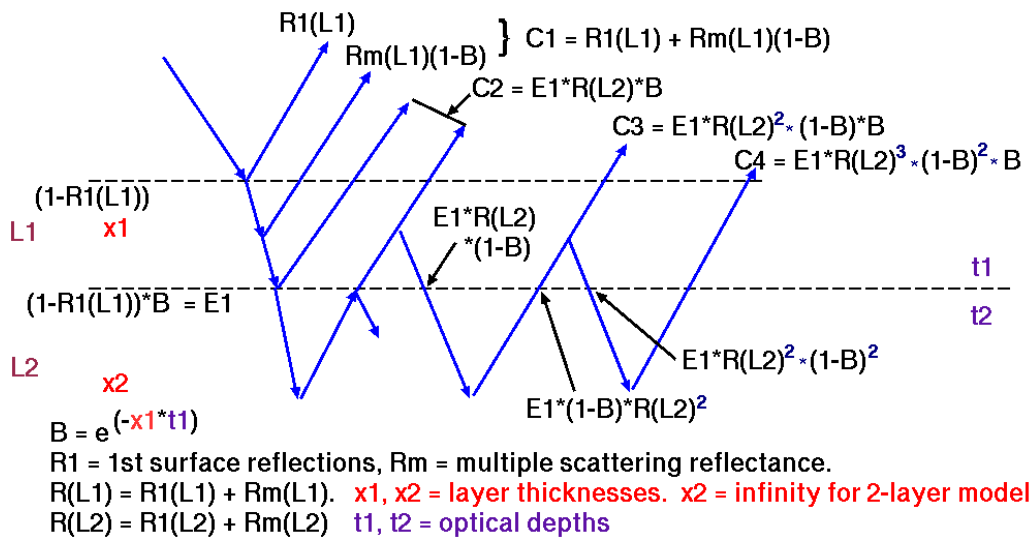
2308

2309



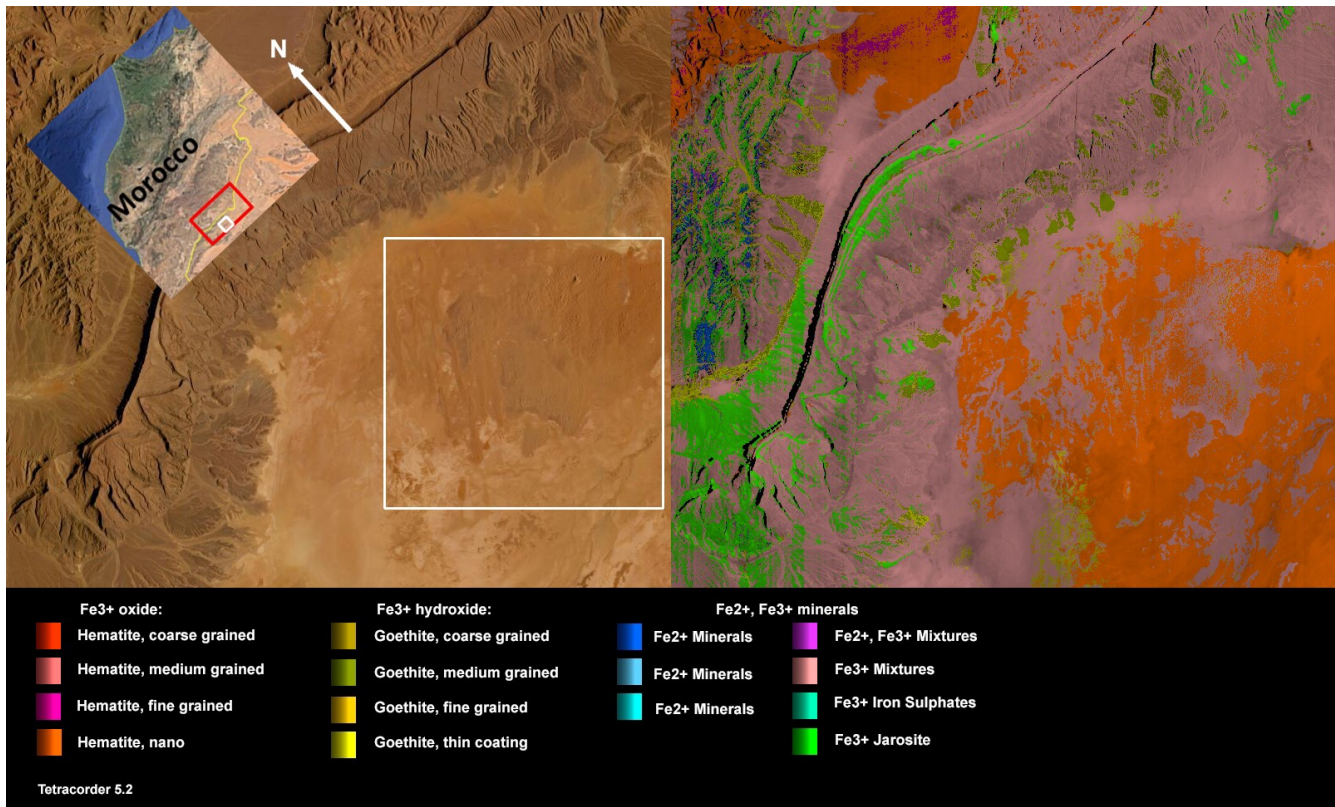
2312 Figure 24. Model spectra of a layered surface with larger grain sizes deeper down (red line) results in  
 2313 increasing band depths in spectral regions with lower absorption coefficients and matches the  
 2314 lab data (black line). Such layered media enhances weak bands, like the 1.04- $\mu\text{m}$  absorption, exactly as  
 2315 observed in the Saturn system. Non-layered models (green and blue curves) cannot match  
 2316 the observed lab spectrum (black curve), but the layered model (red curve) shows a close  
 2317 match. Non layered models can only match band depths for some absorptions whereas the  
 2318 layered model closely matches all. This new model is derived from the Clark et al. (2012)  
 2319 radiative transfer algorithms plus Clark and Roush (1984) equations 18 to 24. See Table 6  
 2320 for derived band depths.  
 2321  
 2322  
 2323

2325

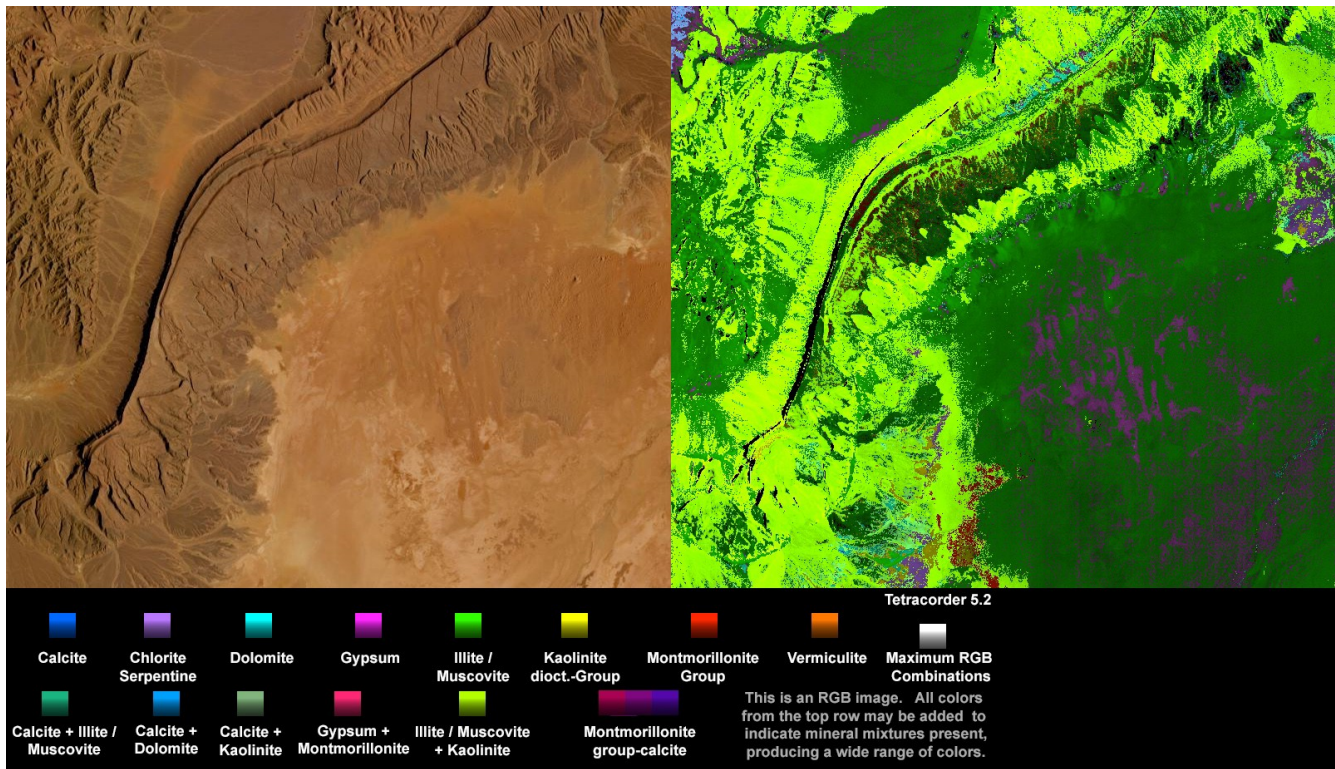


$$Rs = C_1 + C_2 + C_3 + C_4 + \dots$$

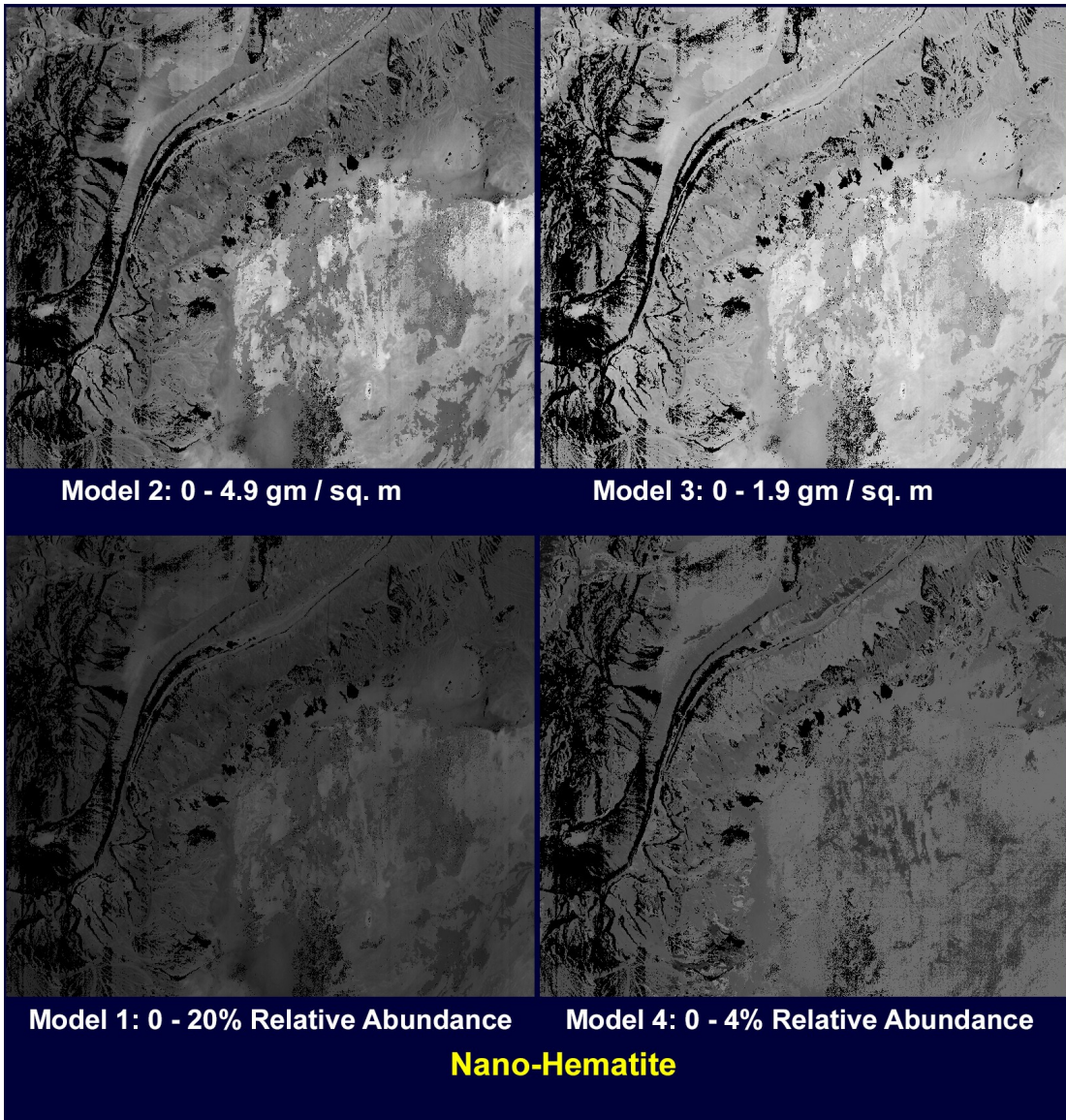
2327 Figure 25. Example of multi-stream equations for reflectance,  $Rs$ , from a multi-layer surface. The  
 2328 multi-stream model is coded and operational for up to 3-layer models.  
 2329  
 2330  
 2331  
 2332



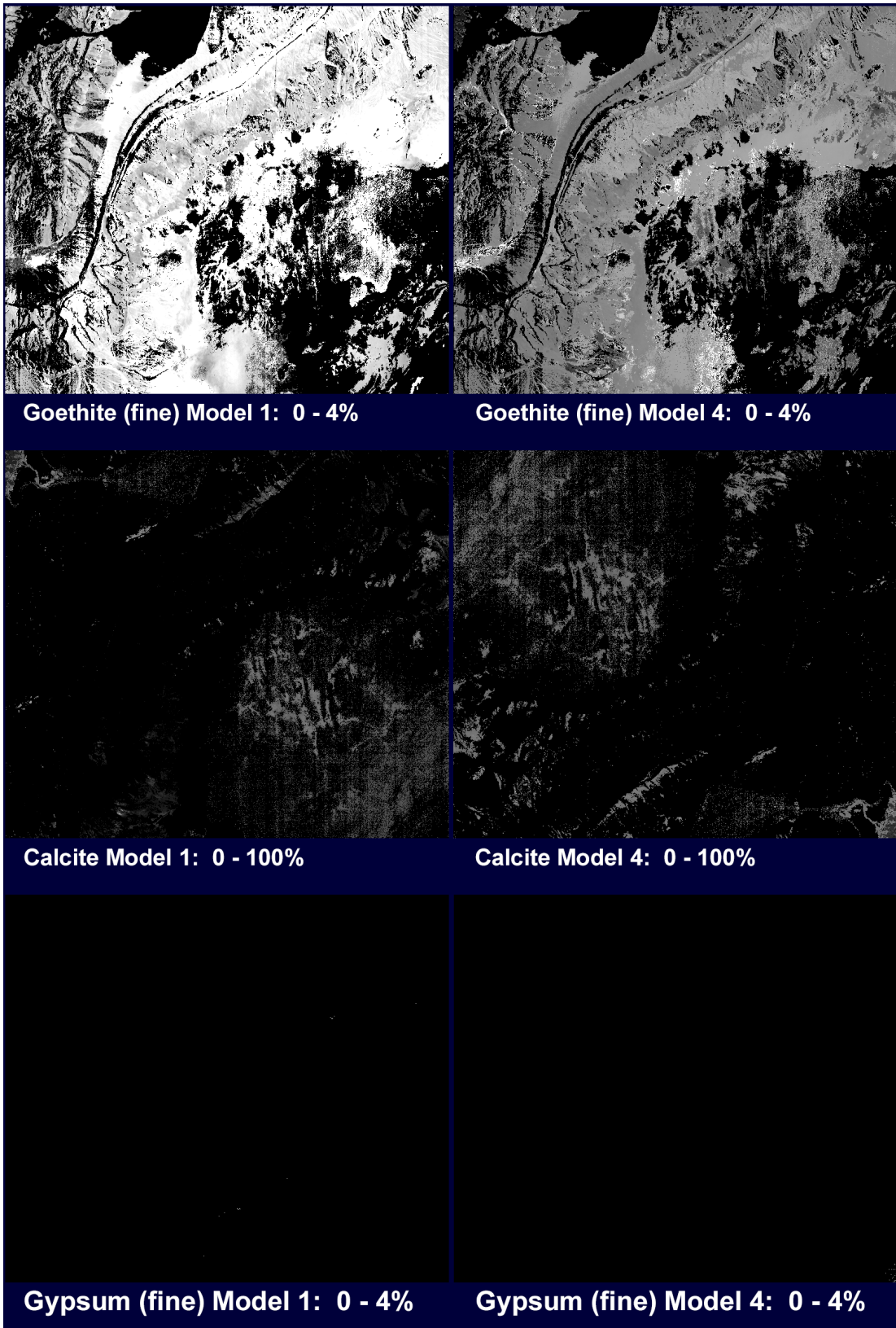
2333      Figure 26. Tetracorder 5.27d1 results for a portion of the FRAGMENT study area in Morocco. The  
 2334      scene is a crop from EMIT cube emit20230206t101334\_003707\_s000\_l2a\_rfl\_b0106\_v01. The  
 2335      salmon color is mainly areas containing hematite-goethite mixtures. The green areas, jarosite, is a  
 2336      misidentification caused by a deficiency in the spectral libraries used: the green areas appear to be  
 2337      hematite-goethite mixtures with grain sizes not represented in the libraries. The white box is the area  
 2338      where abundances were derived and reported in Table 8.  
 2339



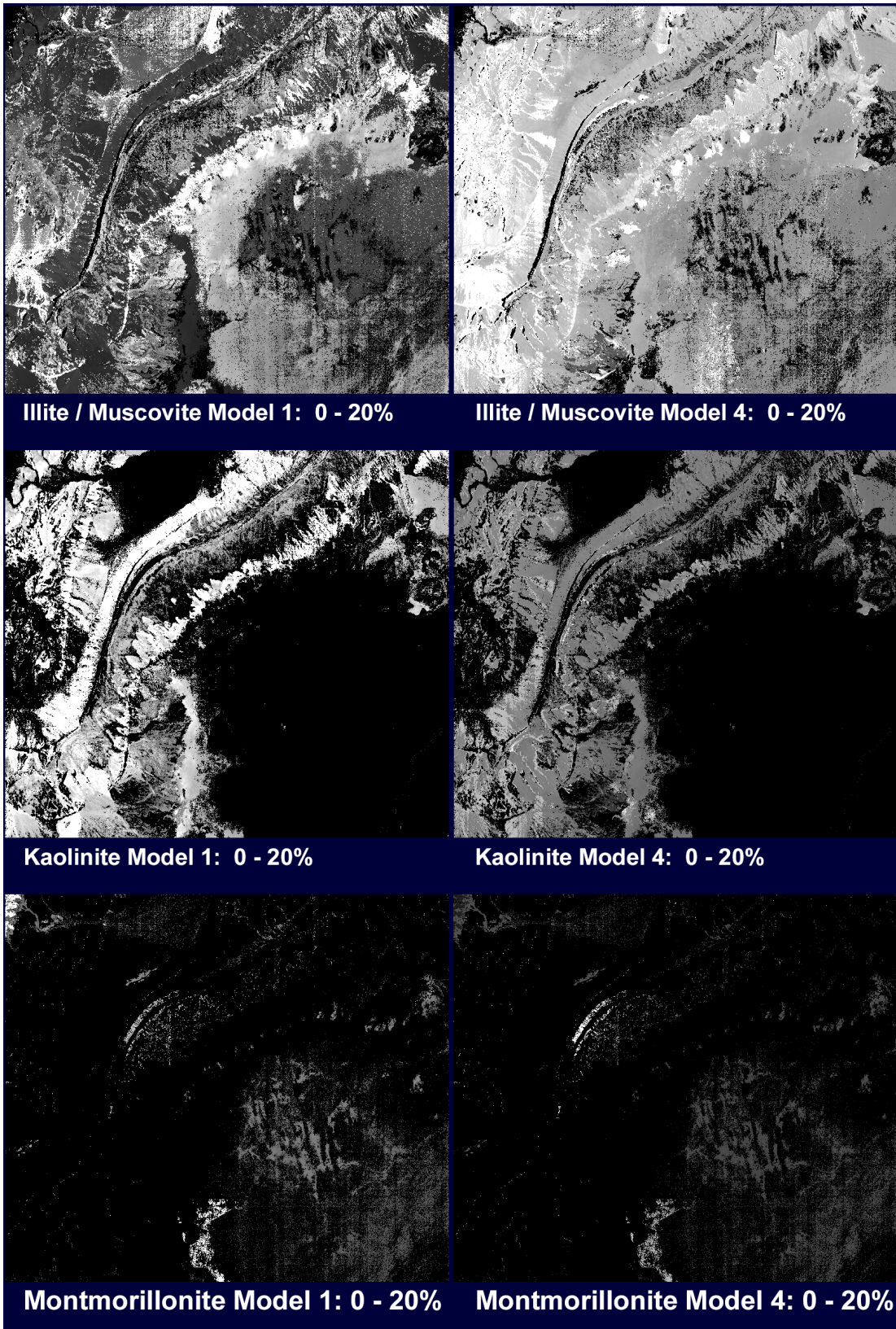
2340 Figure 27. Tetracorder 5.2d1 results of the EMIT 8 minerals for a portion of the FRAGMENT study  
 2341 area in Morocco. The purple areas in the lower right are calcite-montmorillonite group mixtures.  
 2342 The scene is a crop from EMIT cube emit20230206t101334\_o03707\_s000\_l2a\_rfl\_b0106\_v01.



2344 Figure 28. Tetracorder 5.27d1 results for nano-hematite and 4 abundance models for the image area  
2345 shown in Figures 26 and 27.  
2346  
2347



2348 Figure 29a. Tetracorder 5.27d1 results for 2 abundance models for goethite, calcite and gypsum for the  
2349 image area shown in Figures 26 and 27.



2351 Figure 29b. Tetracorder 5.27d1 results for 2 abundance models for illite/muscovite, kaolinite and  
2352 montmorillonite for the image area shown in Figures 26 and 27.

2353

2354

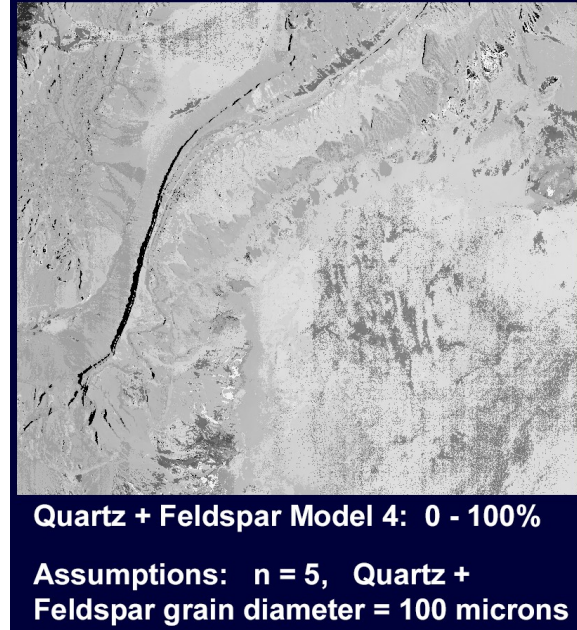
2355

2356

2357

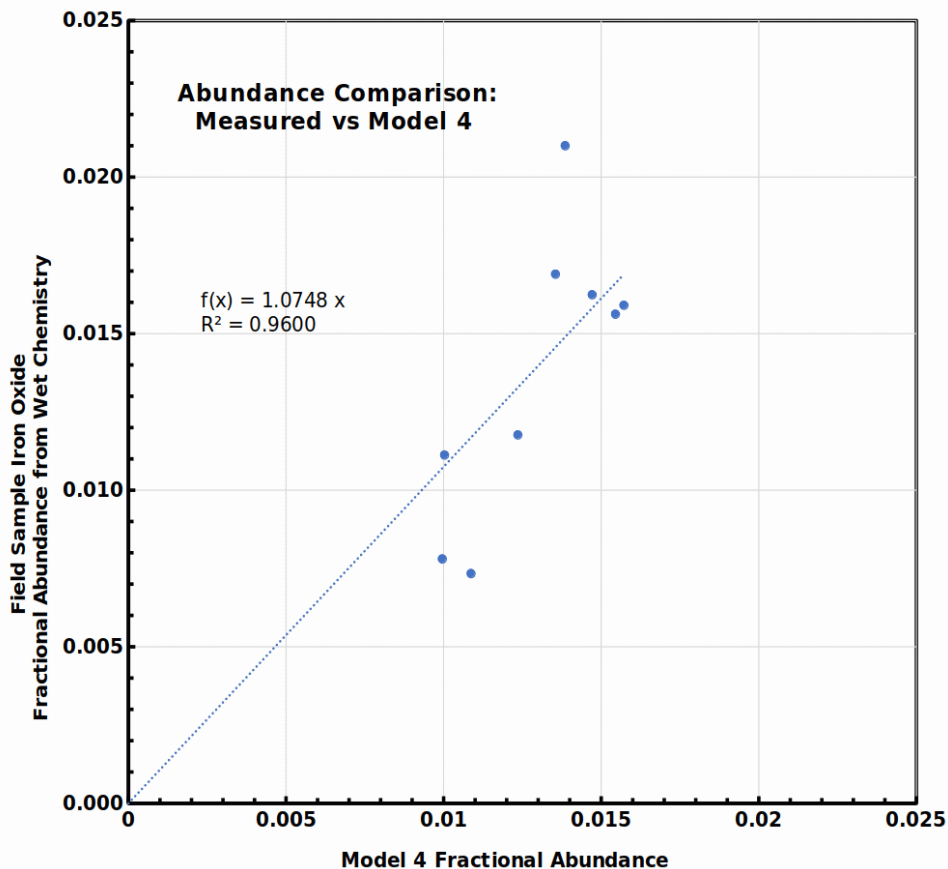
2358

2359



2361 Figure 30. Tetracorder 5.27d1 Model 4 abundance results for quartz +feldspar for the image area  
2362 shown in Figures 26 and 27.

2363



2366     Figure 31. Comparison of wet chemistry data from González-Romero et al., 2023 converted to iron  
 2367     oxide abundance is compared to Model 4 abundance.

2368

2369

2370

2371

2372

2373

2374